Winter 12-15-2017

Multiscale imaging of the mouse cortex using two-photon microscopy and wide-field illumination

Jonathan Richard Bumstead
Washington University in St. Louis

WASHINGTON UNIVERSITY IN ST. LOUIS

School of Engineering & Applied Science

Department of Biomedical Engineering

Dissertation Examination Committee:
Joseph Culver, Chair
Daniel Côté
Viktor Gruev
Timothy Holy
Matthew Lew
Daniel Moran

Multiscale Imaging of the Mouse Cortex Using Two-Photon Microscopy and Wide-Field Illumination

Jonathan R. Bumstead

A dissertation presented to
The Graduate School
of Washington University in
partial fulfillment of the
requirements for the degree
of Doctor of Philosophy

December 2017
St. Louis, Missouri

Table of Contents

List of Figures

List of Tables

Acknowledgments

I would like to begin by acknowledging the academic and financial support provided by the Imaging Sciences Fellowship and McDonnell Center for Systems Neuroscience.

My growth as a scientist and engineer during my dissertation is largely thanks to my advisor, Dr. Joe Culver. I feel fortunate to have landed in such a position with an advisor who trusted me to build a complicated system from the ground up. In addition to all Joe taught me about optical system development, he has provided me countless resources to construct the system and was always the first to suggest I apply to a conference, summer school, or fellowship.

I would also like to thank the rest of my committee for advising me throughout my dissertation, especially Dr. Daniel Côté, who invited me to work in his lab during August 2014 only shortly after meeting him at Neurophotonics School in Quebec. My experience in his lab was arranged at a crucial time during the development of our system, and I learned fundamental optical alignment procedures and design considerations essential for constructing the system.

Thanks are also due to the rest of the members of the Culver lab. From failed design plans to paper publications, I enjoyed discussing with them both the rewarding and frustrating experiences that come with pursuing such an endeavor. Special thanks to Dr. Adam Bauer for helping me in my first experiments in the Culver lab, as well as Jasmine Park and Ike Rosen who both performed epic craniotomy surgeries.

Most importantly, I need to thank my family. First and foremost, my loving parents, Rick and Vicki, who have supported me in all my projects inside and outside the lab. They have always provided, and continue to provide, a safe and energizing place to call home. Grandma Mary-Lou (the puzzle grandma) and Grandpa Dick who introduced me to scientific inquiry and engineering.

My two sisters, Breann and Claire, and my brother, James, who are not only caring siblings, but true friends who have been supportive throughout my dissertation.

And finally, I am incredibly grateful to have spent the final years of my PhD with my partner and best friend, Ena. She has been a constant source of encouragement, and, regardless of my successes and failures at work, I find myself always looking forward to sharing our days together.

Jonathan Bumstead

Washington University in St. Louis

December 2017

ABSTRACT OF THE DISSERTATION

Multiscale Imaging of the Mouse Cortex Using Two-Photon Microscopy and Wide-Field Illumination

by

Jonathan Richard Bumstead

Doctor of Philosophy in Biomedical Engineering

Washington University in St. Louis, 2017

Professor Joseph P. Culver, Chair

The mouse brain can be studied over vast spatial scales ranging from microscopic imaging of single neurons to macroscopic measurements of hemodynamics acquired over the majority of the mouse cortex. However, most neuroimaging modalities are limited by a fundamental trade-off between the spatial resolution and the field-of-view (FOV) over which the brain can be imaged, making it difficult to fully understand the functional and structural architecture of the healthy mouse brain and its disruption in disease. My dissertation has focused on developing multiscale optical systems capable of imaging the mouse brain at both microscopic and mesoscopic spatial scales, specifically addressing the difference in spatial scales imaged with two-photon microscopy (TPM) and optical intrinsic signal imaging (OISI). Central to this work has been the formulation of a principled design strategy for extending the FOV of the two-photon microscope. Using this design approach, we constructed a TPM system with subcellular resolution and a FOV area 100 times greater than a conventional two-photon microscope. To image the ellipsoidal shape of the mouse cortex, we also developed the microscope to image arbitrary surfaces within a single frame

using an electrically tunable lens. Finally, to address the speed limitations of the TPM systems developed during my dissertation, I also conducted research in large-scale neural phenomena occurring in the mouse brain imaged with high-speed OISI. The work conducted during my dissertation addresses some of the fundamental principles in designing and applying optical systems for multiscale imaging of the mouse brain.

Chapter 1: Introduction

1.1 Overview

Advancements in optical imaging technology have enabled the study of the mouse brain from nanoscale to macroscale, spanning several orders of magnitude in field-of-view (FOV) and resolution (Fig. 1.1) [1-3]. The work presented in this thesis focuses specifically on mesoscopic imaging, a term used to describe spatial scales existing between microscopic and macroscopic imaging. Mesoscopic imaging studies have focused on recording neural activity over large regions of the brain with the ultimate goal of simultaneously recording the activity of every neuron in the nervous system of small organisms [4, 5]. The major challenge faced in developing imaging tools for accomplishing this goal is the fundamental trade-offs between resolution, FOV, signal-to noise ratio (SNR), and imaging speed [4, 6]. Much of this work in whole-brain imaging and network mapping has been motivated by the effort to map the human connectome using hemodynamic measurements obtained with functional magnetic resonance imaging (fMRI) [7]. The hemodynamic response measured with fMRI results from a complex interaction between neurons, astrocytes, and blood vessels called the neurovascular response that is a relatively indirect report of brain function [8]. More direct measurements of brain activity can be achieved by measuring electrochemical and ionic concentration changes in the brain, which can be recorded in small organisms with electrodes [9], voltage sensitive dyes [10], and calcium reporters [11].

Until recently, optical sectioning fluorescence microscopy techniques, such as two-photon microscopy (TPM) [12-14], light sheet microscopy [15, 16], and confocal microscopy [17], have been used with these fluorescence reporters of voltage and calcium for *in vivo* imaging of only a small percentage of the brain. Improvements in these modalities and genetically encoded calcium

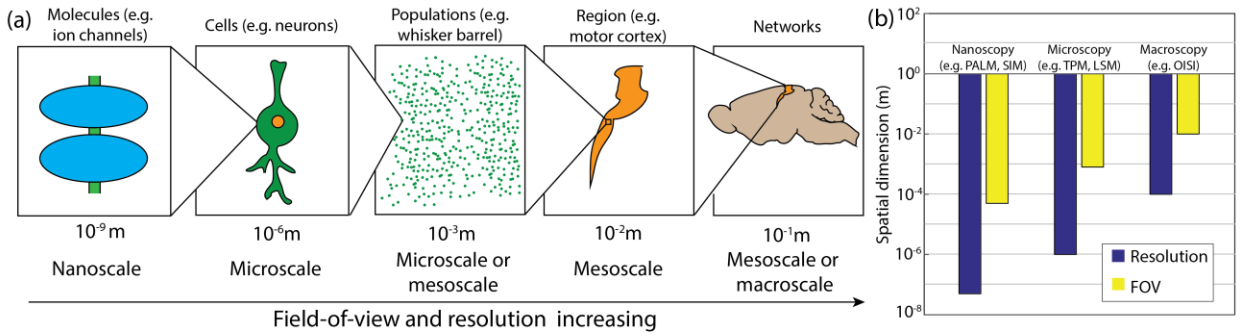

Fig. 1.1. Range of spatial scales for imaging the mouse brain. (a) Hierarchy of structures that are imaged in the mouse brain and their corresponding spatial scales. (b) Approximate field-of-view (FOV) and lateral resolution of optical imaging modalities used to study the brain over different spatial scales including photoactivated localization microscopy (PALM), structured illumination microscopy (SIM), two-photon microscopy (TPM), lightsheet microscopy (LSM), and optical intrinsic signal imaging (OISI).

indicators coupled with the growing interest in mesoscopic imaging over the last few decades have spawned several whole-brain imaging studies on calcium dynamics in zebrafish [18, 19] and C. Elegans [20, 21]. Researchers have begun to use these microscopy methods to examine correlated spontaneous activity of hundreds of neurons with computational analyses that are conceptually similar to those used in functional connectivity studies with fMRI [3, 18, 19, 21-23]. However, whole-brain imaging of mice that are analogous to studies done with fMRI in humans are not possible using conventional optical sectioning microscopes because the FOV is limited to around 500 x 500μm^2 (i.e. a FOV diameter of 707μm) [13, 24].

Due to this FOV limitation, researchers have primarily utilized mesoscopic optical imaging with wide-field illumination (MOI-WFI) techniques to study brain function over large regions of the mouse cortex (up to 10 x 10mm^2 FOV) [10, 25, 26]. MOI-WFI has successfully measured the functional neuronal response to a variety of stimuli [1, 27, 28], as well as spontaneous brain activity that can be used to identify resting-state functional connectivity networks [26, 29]. In addition to studies of functional connectivity and network mapping in the mouse brain, MOI-WFI has also

been invaluable in the study of other neural phenomena that occur over large regions of the mouse cortex such as cortical spreading depression [30], retinal waves [31], Mayer waves [32], and slow wave sleep [29]. However, MOI-WFI techniques have relatively poor resolution (100-300μm lateral resolution) in comparison to optical sectioning microscopy (0.5-1.5μm lateral resolution) [25, 33]. Therefore, the cellular dynamics of brain networks and large-scale neural phenomena in mice are still poorly understood.

To bridge the gap in studying the function of the mouse brain at these two different spatial scales, we designed and constructed a large FOV two-photon microscopy (LF-TPM) system using off-the-shelf components (Chapter 2) and an adaptive LF-TPM (ALF-TPM) system (Chapter 3). As a demonstration of the utility of whole brain functional imaging, MOI-WFI is applied to studying Mayer waves [32] and peri-infarct depolarization in mice (Chapter 4). The rest of the introduction will review basic principles and applications of TPM and MOI-WFI.

1.2 Two-Photon Microscopy

1.2.1 General Principle

Fluorescence microscopy is a powerful tool for studying the brains of small organisms. The basic principle is to use an engineered fluorescent protein (FP) that can be introduced to an organism through chemical or biological methods, excite the FP with light delivered to the sample or organism, and detect the emitted light due to fluorescence [34-36]. Fluorescence microscopy techniques and the advances in FP engineering have enabled imaging of the function and structure of specific cell types (e.g. neurons, microglia, and astrocytes) in the brain [37]. Furthermore, the spectral and conformational properties of FP can be tailored to specific applications, and the overall brightness and photostability of probes continue to improve [34, 38]. An example of such a fluorescent probe is the calcium indicator GCaMP, which is a fusion of green fluorescent protein

(GFP), calmodulin, and M13 [39-41]. The conformation of GCaMP changes when bound to calcium such that the rate of fluorescence within neurons greatly increases during an action potential due to the influx of calcium into the cell. In the next section, we review some of the applications of fluorescence imaging, specifically TPM, for small animal imaging. For now, we focus on the basic principles of one-photon and two-photon fluorescence.

In comparison to one-photon absorption, two-photon absorption has a much lower probability of occurring and therefore generally requires high light intensities [42, 43]. Many of the properties of two-photon absorption can be explained by the fact that the rate of the phenomenon is proportional to the square of the excitation intensity (Appendix A). As a result, photons emitted due to two-photon excitation are essentially localized to the focal point of an objective lens, whereas emission photons in one-photon excitation are spread throughout the excitation volume (Fig. 1.2(a-b)) [36]. To restrict imaging to a single axial plane in the sample with one-photon excitation, confocal microscopy requires a pinhole at the detector. Conversely, the localization of two-photon excitation requires no pinhole for sectional imaging because even scattered emission photons in the sample originate from the focal point of the objective [12, 44]. A more concrete definition of the localization of the emission due to two-photon excitation requires analysis of the intensity distribution as a function of space, which depends on imaging conditions (e.g. the numerical aperture (NA) of the lens, sample properties, etc.) and the excitation source [12, 42, 45].

The time averaged fluorescence flux $\langle F(t) \rangle$ depends on several other important parameters included the concentration of the fluorophore $C(\vec{r})$, the fluorophore cross-section σ_n, the collection efficiency ϕ, and quantum efficiency of the dye η. Assuming uniform fluorophore concentration in the sample, the fluorescence flux due to an *n*th-order excitation process is:

$$\langle F(t)\rangle = \frac{1}{n} g^{(n)} \phi \eta C \sigma_n \langle I_0(t)\rangle^n \int_V S^n(\vec{r}) d\vec{r} \tag{1.1}$$

where $\langle I_0(t)\rangle$ is the time average of the temporal distribution of the excitation light, $S(\vec{r})$ is the spatial distribution of the excitation light, and $g^{(n)}$ is the nth-order temporal coherence factor. For a continuous wave (CW) laser, $g^{(n)}$ = 1. For a pulsed laser, the temporal coherence is:

$$g^{(n)} = \frac{{g_p}^{(n)}}{(f\tau)^{n-1}} \tag{1.2}$$

where f is the repetition rate of the laser, and τ is the pulse width. For a pulse with Gaussian temporal profile, ${g_p}^{(2)} = 0.66$ [42, 43].

The intensity distribution of light depends on the excitation source and NA of the objective lens, and must be considered for solving Eq. (1.1). In a thick sample for which the concentration of fluorophore is equally distributed throughout the excitation volume, the expression for the fluorescence signal measured when the sample is excited by focused a Gaussian beam with wavelength λ is:

$$\langle F(t)\rangle = 0.33\pi \frac{\phi \eta C \sigma_2 n_0 \langle P(t)\rangle^2}{\lambda (f\tau)^{n-1}} \tag{1.3}$$

where n_0 is the refractive index of the sample medium, and $\langle P(t)\rangle$ is the average power of the excitation light at the sample. It is important to note that the fluorescence signal is predicted to be independent of the excitation NA. However, the collection efficiency ϕ depends on the collection NA squared. Because two photon microscopes generally use epi-collection systems, the NA of the objective does affect the SNR [42, 43].

Another result of two-photon absorption's dependence on the illumination excitation squared is that the use of a pulsed laser greatly increases (i.e. about a factor of 10^5) the rate of the phenomenon (Eq. 1.3) [43, 46]. A way to conceptualize this result starts with the assumption that

the probability of two-photon absorption should depend on the probability of finding two photons within the FP volume at the same time [42]. Naturally, this probability is much lower than the probability of finding a single photon within the FP volume. Therefore, two-photon absorption requires high light intensities, which are achieved by spatial and temporal confinement of the excitation source (Fig. 1.2(c-d)) [47]. The full design of a two-photon microscope is discussed in Chapter 2.

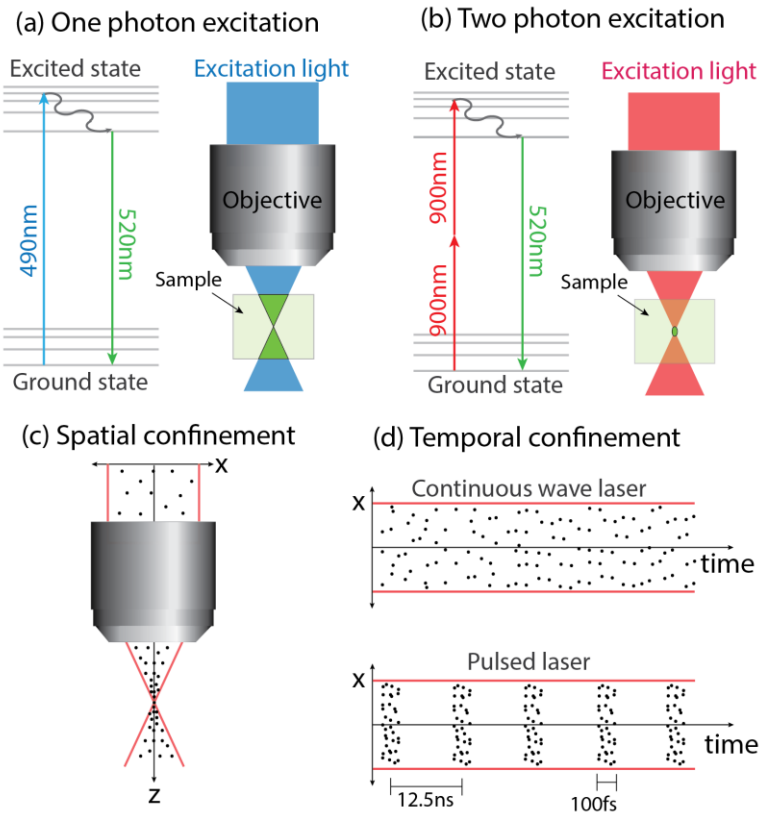

Fig. 1.2. One-photon and two-photon absorption properties. (a) Two state model of fluorophore excited by one photon. Light is emitted throughout entire focal volume. (b) Same as (a), but for two-photon absorption (c) Spatial confinement of light for two-photon excitation. (d) Temporal confinement of light with pulsed laser. Figure was adapted from Stutzmann et al. and So et al. [36, 47].

1.2.2 Applications in Neuroscience

TPM has been applied to study populations of neurons, neuroglia, and blood vessels in various regions of the mouse brain including the visual cortex [24, 48, 49], vibrissal motor cortex [14, 50],

and hippocampus [51-53]. In all cases, the skull above the region of interest is either thinned or removed to eliminate light scattering by the skull (Fig. 1.3(a)) [54]. The full procedure for a craniotomy is presented in Chapter 2. The head of the mouse is then fixed and the region is imaged using a two-photon microscope.

To image the cerebral vasculature, fluorescein-dextran or Texas Red-dextran is injected into the tail vein (5% v/v solution). The conjugation of dextran to the FP prevents it from leaving the vasculature [55]. After acquiring images of the vasculature, specific vessels over the FOV can be scanned to determine changes in the vessel diameter and velocity of blood flow in the vessels at Nyquist frequency typically around 20 Hz using a traditional mirror galvanometer (Fig. 1.3(b)) [56]. Using TPM, Drew et al. imaged changes in flow and volume of vessels in the primary vibrissa cortex of mice. The results include an analysis of the frequency content of the vessel diameter changes over time, which enable the comparison of arteriole and venous blood flow without stimulation, during a brief stimulation, and during a long stimulation to the vibrissa [14].

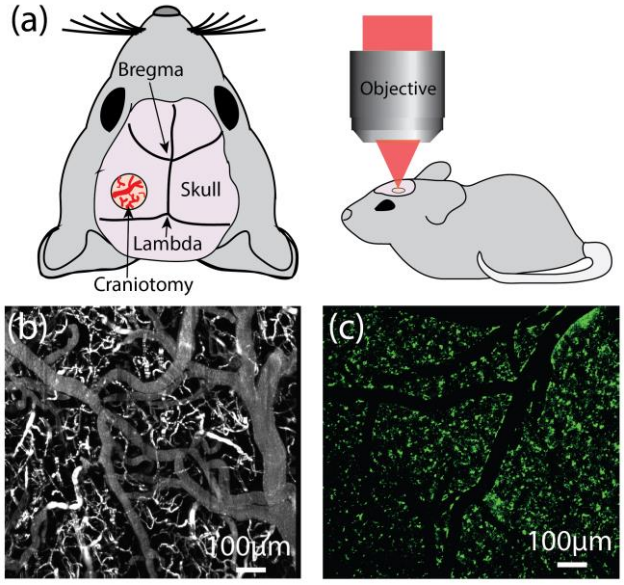

Fig. 1.3. *In vivo* TPM. (a) Dorsal view of mouse prepared for imaging with TPM. A portion of the skull is removed over region of interest (b) Maximum projection image of cerebral vasculature collected with TPM (c) Maximum projection image of microglia in $Cx3Cr1^{GFP+/-}$.

Calcium imaging of neurons is typically achieved by using fluorescent calcium indicators in transgenic mice. It has been shown that calcium transients are well correlated to action potentials, and are therefore a powerful tool for studying the activity of individual neurons in the mouse brain [57, 58]. Functional maps of neural populations are created by presenting a stimulus to a small animal and correlating it to calcium dynamics measured in individual cells with TPM. For example, visual stimuli with different orientations were presented to rats and cats to show differences in the functional organization of neurons in the visual cortex [24]. In a study on more complex neuronal processing, calcium activity in the primary visual cortex was imaged as mice navigated through mazes generated by a virtual reality projection. The results of this study revealed neural encoding of the spatial location and stimulus-predictive responses in layer 2/3 neurons of the mouse primary visual cortex [48]. These representative studies demonstrate how researchers study neural representations of stimuli and behavior of small organisms using TPM.

In addition to neurons, researchers have also used TPM to study microglia and astrocytes. The microglia response to focal brain injury induced by laser ablation or glass electrode was imaged in the motor and barrel cortex of mice (Fig. 1.3(c)). This study was conducted with transgenic mice in which the Cx3cr1 gene was replaced with enhanced GFP so that all microglia were fluorescently labeled. By locally injecting ATP into the brain, the same microglia response was observed [59]. In another study, rhod-2 AM was pressure injected into the primary visual cortex of mice to visualize calcium dynamics of astrocytes. The role of astrocytes in neuronal circuits during spontaneous brain activity, as well as optogenetic activation, were then investigated using TPM [60].

These TPM studies in rodents provide a brief overview of the experimental approaches used to study the micro-architecture of the brain. One of the major limitations in these studies is the

restricted FOV of conventional TPM systems. In the next section, we briefly discuss the reasons why TPM is limited to imaging <1mm diameter FOV.

1.2.3 FOV Limitations

While there have been advancements in TPM, many of the developments have focused on imaging faster [61] and deeper into tissue [46] by use of adaptive optics [62] and manipulation of the point spread function (PSF) with temporal focusing [20], microlens arrays [63], and diffractive optical elements [64]. Only recently have researchers turned attention to extending the FOV [49, 65, 66].

The FOV in TPM systems is limited primarily by high-magnification objective lenses, poorly designed scan optics, and small field collection systems [65-68]. The use of high-magnification objectives stems from resolution and signal requirements that demand objective lenses with numerical aperture (NA) greater than 0.7. As a result, this biases microscope designs towards objectives with focal lengths less than 9mm (i.e. magnification greater than 20X), which make imaging field diameters greater than 1mm difficult to achieve [12, 45, 69, 70].

The less explored and more technically challenging problem in extending the FOV is the scan optics (Fig. 1.4). Interestingly, there has been greater emphasis on improving the performance of objective lenses, typically high-NA high-magnification objectives, than scan optics used in laser scanning microscopy systems. Therefore, the current FOV limit in many commercially available and custom-built two-photon and confocal microscopes is actually due to the use of achromatic doublet lenses as scan optics, not the objective lens [66, 67]. As the beam is scanned off axis, vignetting and optical aberrations, such as field curvature and astigmatism, degrade the performance of the microscope (Fig. 1.4(a)) [49]. A way to visualize these aberrations is through a spot diagram, which shows the intersection of rays at a cross section in the optical system. If the beam is well focused at the image plane (e.g. on axis imaging with an achromatic doublet), then

the spots are well localized (Fig. 1.4(b)). If the spot size RMS radius is less than the theoretical resolution limit predicted by diffraction, then the image condition is said to be diffraction limited. If instead the spots are spread more than the diffraction limit, then the system is limited by geometric aberrations (Fig. 1.4(c-d)).

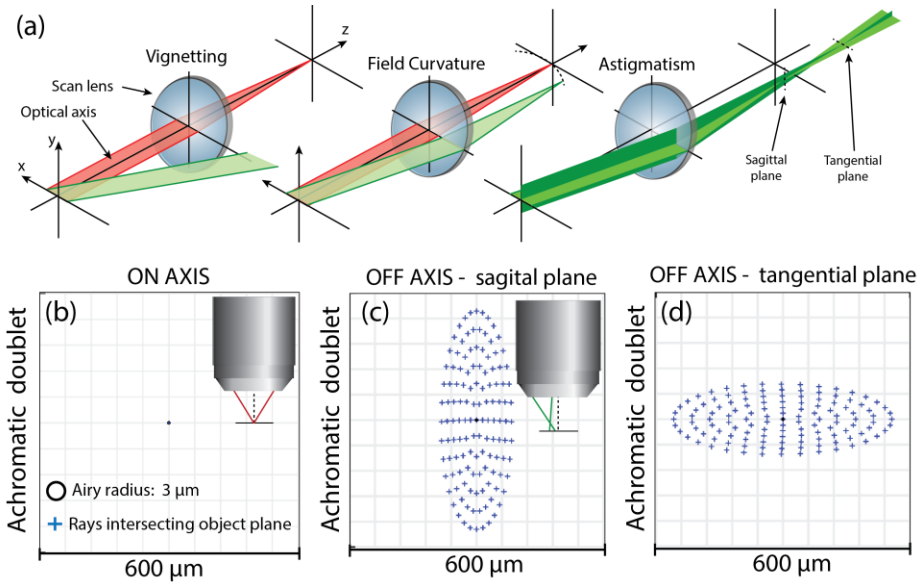

Fig. 1.4. Optical aberrations introduced by scan optics. (a) Vignetting and optical aberrations of scan optics (b) Spot diagram of rays intersecting image plane on axis in a microscope with achromatic doublet lenses. (c) Same as (b), but off axis and at the sagittal plane. (d) Same as (c), but for tangential plane.

1.3 Mesoscopic Optical Imaging with Wide-Field Illumination

1.3.1 General Principle

The primary absorber of visible and near infrared (IR) radiation in tissue is hemoglobin [1]. Therefore, measurement of light absorption by tissue provides information about the concentration of oxygenated (HbO_2) and deoxygenated hemoglobin (Hb_R), which serve as indirect measurements of neural activity through the neurovascular response [71].

A basic OISI system is shown in Fig. 1.5. Light sources of different wavelength (typically light emitting diodes (LEDs)) sequentially provide wide-field illumination over the exposed cortex of a

small animal. The light is either absorbed by the tissue or diffusely scattered back to a camera positioned above the animal. Orthogonal polarizers are positioned in front of the LEDs and the camera so that only diffusely reflected light is detected [1, 26]. Changes in light intensity measurements can be converted to concentrations of HbO_2 and Hb_R by using the modified Beer-Lambert law and molar extinction coefficient

$$I(\lambda, t) = I_0(\lambda)\exp(-\mu_a(\lambda, t) * L(\lambda)) \tag{1.4}$$

where I is the intensity of light detected by the camera, I_o is the initial light intensity at the surface, μ_a is the absorption coefficient of the tissue, and L is the mean pathlength light travels in the tissue [72]. I_o is difficult to measure, so differential measurements are often made with respect to the average intensity measured by the camera [25]. The absorption of light at a particular wavelength depends on the concentration of all absorbers in the tissue.

$$\mu_a(\lambda, t) = \sum_n \varepsilon_n(\lambda) c_n\,(t) \tag{1.5}$$

where ε_n is the molar extinction coefficient of the nth absorption species in the tissue and c_n is the concentration of the nth absorption species. Assuming that hemoglobin is the primary absorber in the tissue, Eq. 1.5 can be written as:

$$\mu_a(\lambda, t) = \varepsilon_{HbO}(\lambda) c_{HbO}(t) + \varepsilon_{HbR}(\lambda) c_{HbR}(t) \tag{1.6}$$

where $\varepsilon_{HbO}(\lambda)$ and $\varepsilon_{HbR}(\lambda)$ are the extinction coefficients of HbO_2 and Hb_R. The extinction coefficients of HbO_2 and Hb_R are wavelength dependent (Fig. 1.5(a)). Therefore measuring changes in their concentration can be achieved by imaging with two or more wavelengths of light. In the case that two wavelengths are used, Eq. 1.5 and Eq. 1.6 can be combined to express changes

in light intensity measured by the camera as a function of differential changes in HbO_2 and Hb_R concentration.

$$\ln\left[\frac{I(\lambda=\lambda_1,t)}{I_m(\lambda=\lambda_1)}\right]=\ln\left[\Delta I_{\lambda_1}(t)\right]=-\left(\varepsilon_{HbO,\lambda_1}\Delta c_{HbO}(t)+\varepsilon_{HbR,\lambda_1}\Delta c_{HbR}(t)\right)L(\lambda_1) \quad (1.7)$$

$$\ln\left[\frac{I(\lambda=\lambda_2,t)}{I_m(\lambda=\lambda_2)}\right]=\ln\left[\Delta I_{\lambda_2}(t)\right]=-\left(\varepsilon_{HbO,\lambda_2}\Delta c_{HbO}(t)+\varepsilon_{HbR,\lambda_2}\Delta c_{HbR}(t)\right)L(\lambda_2) \quad (1.8)$$

where λ_1 and λ_2 are the wavelengths of illumination, ΔI_{λ_1} and ΔI_{λ_2} are the normalized light intensity measurements made by the camera, and Δc_{HbO} and Δc_{HbR} are differential measurements of HbO_2 and Hb_R. Each pixel in the image represents a summation of hemoglobin concentrations over some depth in the tissue, which depends on how deeply the photons can penetrate into the tissue before the light is scattered. The depth penetration of OISI is limited to the superficial layers of the mouse brain (<650μm) [1, 25-27, 71].

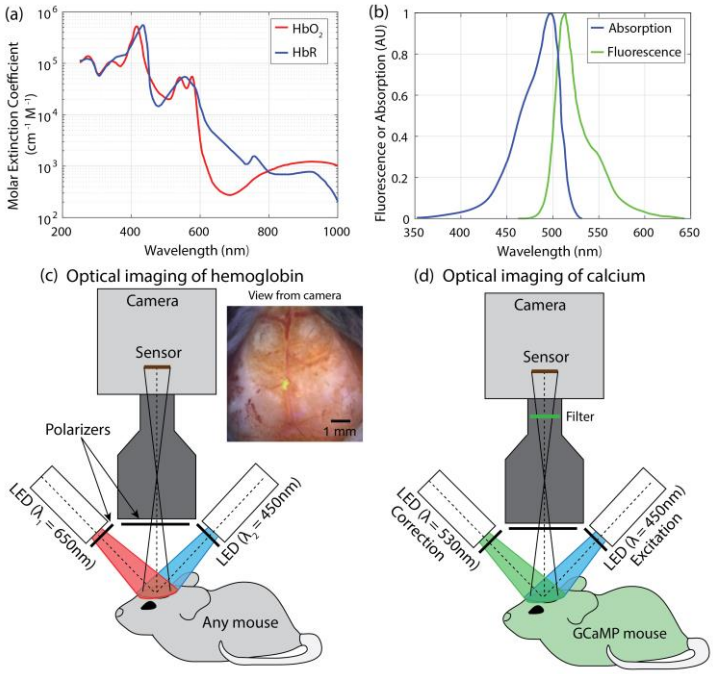

Fig. 1.5. Mesoscopic optical imaging with wide-field illumination. (a) Extinction coefficient of oxy- and deoxy-hemoglobin as a function of wavelength. (b) Excitation and emission spectrum of GCaMP6f (data from Harris et al. [73]). (c) Setup of optical intrinsic signal imaging of the mouse brain. (d) Setup of mesoscopic calcium imaging.

MOI-WFI can also be used to measure calcium dynamics over the brain of small animals. The optical system requires similar components to OISI: a camera, LEDs, and polarizers. Excitation light ($\lambda \approx 450$nm) illuminates the exposed cortex of a mouse with a FP sensitive to calcium concentration (Fig. 1.5(b) and (d)). The emission is then collected by the camera, while filtering out the excitation with an optical filter before the sensor. Due to the hemoglobin in the tissue, some of the emission light is absorbed. Therefore, another LED with wavelength similar to the peak emission wavelength of the FP ($\lambda \approx 530$nm) illuminates the mouse head after the excitation. The hemoglobin measurement acquired by the camera can then be used to correct the fluorescence signal to account for absorption of the emission by hemoglobin in the tissue [25].

1.3.2 Applications in Neuroscience

MOI-WFI has been used to identify functional regions associated with auditory, visual, vibrissa, and forepaw stimulations. For example, the spatial extent of HbO_2, HbR, and total hemoglobin (HbT) during whisker and forepaw stimulation were measured in rats using OISI [1]. Similar to TPM, OISI has also mapped the visual cortex by presenting visual stimuli with different orientations to mice [28]. Such studies demonstrate the utility of MOI-WFI for understanding the functional architecture of small animals from a mesoscopic perspective.

In addition to stimulus-based studies, spontaneous brain activity of mice has also been studied with OISI. White et al. demonstrated that spontaneous brain activity in spatially separated brain regions is correlated with respect to time, which recapitulates results of human fMRI studies. The phenomenon, known as resting-state functional connectivity (RSFC), has made a significant impact on how functional connections in the brain are interpreted [26]. Spontaneous correlations of calcium activity in the brain have also been reported using calcium planar imaging [29, 74]. OISI can be applied to study neuropathology in mice, such as stroke. Bauer et al. used an OISI

system to analyze changes in functional connectivity in mice with varying infarct size after a transient middle cerebral artery occlusion (tMCAO). Functional connectivity metrics were also correlated with behavior [75].

In addition to studying disruptions in distributed brain networks, OISI has also been applied to studying peri-infact depolarization (PID) in rodents. PID is a wave of neuronal depolarization that occurs after stroke and during migraine, which results in approximately 5% changes in the optical intrinsic signal [30]. Therefore, the propagation, frequency, and velocity of PIDs can be characterized in mouse models of stroke and migraine. In Chapter 4, I present my work on measuring the spatiotemporal and spectral properties of Mayer waves, RSFC, and PIDs using OISI.

Chapter 2: Large Field-of-View Two-Photon Microscopy

Conventional TPM is capable of imaging neural dynamics with subcellular resolution, but is limited to a field of view (FOV) diameter <1mm. While there has been recent progress in extending the FOV in TPM, a principled design approach for developing LF-TPM with off-the-shelf components has yet to be established. Therefore, we present a design strategy that depends on analyzing the optical invariant of commercially available objectives, scan optics, mirror scanners, and emission collection systems in isolation. Components are then selected to maximize the space-bandwidth product of the integrated microscope. In comparison to other LF-TPM systems, our strategy simplifies the sequence of design decisions and is applicable to extending the FOV in any microscope with an optical relay. The microscope we constructed with this design approach can image <1.7μm and <28μm lateral and axial resolution over a 7mm diameter FOV, which is a 100-fold increase in FOV compared to conventional TPM. Furthermore, the design is cost-effective (<$40,000 beyond the initial expense of the laser) and only requires one scanning relay, which reduces the complexity of other more expensive LF-TPM systems. As a demonstration of the potential that LF-TPM has on understanding the microarchitecture of the mouse brain across interhemispheric regions, we performed *in vivo* imaging of both the cerebral vasculature and microglia cell bodies over the mouse cortex.

2.1 Optical Design Strategy

In its simplest form, a two-photon microscope consists of a scanning system in the x and y direction that is conjugated to the back aperture (which is usually also the back focal plane) of an objective lens. Conjugation of these two planes is achieved with an afocal relay consisting of two lenses, often called the scan and tube lens [76]. Analysis of a ray diagram of this system is the first step

in redesigning the microscope for large FOV imaging. However, as several components are integrated into the system, it can become difficult to make design decisions and isolate components using raytracing techniques. In contrast, analyzing the conservation of radiant power by calculating the optical invariant in the optical system can provide an intuitive understanding of component requirements and enable several design decisions to be made before detailed system optimization or custom component design [77, 78]. The conversation of the optical invariant of a system is valid in aberration-free, lossless systems modeled with ray optics. Therefore, diffraction should be considered when applying the optical invariant to analyze a system. For example, we analyzed systems that were diffraction limited so our quantification of the system performance was more accurate. The approach should also be supplemented with analysis using optical engineering software, which is capable of complex raytracing and diffraction analysis.

The optical invariant is a constant that is conserved throughout an optical system, and can be used to determine the angle and displacement of rays without intermediate raytracing calculations. Often this concept of an optical system's light acceptance is described by the invariant's 3D analog, the throughput or étendue, which is proportional to the square of the invariant [77]. Throughput and the optical invariant are conceptually interchangeable. Throughout this report, we calculate the optical invariant, which can be determined by the height and angle of the chief and marginal rays, for optical components in isolation, as well as for integrated optical systems consisting of several components. In general, the optical invariant of an integrated system will be limited by the component with the lowest optical invariant in isolation. For example, if a galvanometer has a lower invariant in isolation in comparison to an objective, then the optical invariant of a system consisting of both components will be equal to the invariant of the galvanometer. In this case, the objective would not be imaging to its full capabilities as specified by manufacturers. Our approach

for designing a LF-TPM system was to first select a high throughput objective lens, and then identify optical components capable of supporting an invariant equal to or greater than the invariant of the objective in isolation.

In some cases, determining the optical invariant of a component is simple, requiring only the input beam diameter and scan angle listed by manufacturers. However, the invariant of many scanning lenses are specified for a single operating condition or not at all, and full characterization of the component requires measuring the invariant as a function of input beam diameter using optical engineering software. After selecting candidate elements for LF-TPM and evaluating their invariant in isolation, we tested the integrated optical system, first with optical engineering software (OpticStudio, Zemax, Kirkland, USA) and then experimentally with fluorescent beads.

2.1.1 Optical Invariant Analysis of a Laser Scanning Two-Photon Microscope

We analyzed the conservation of radiant power of a basic laser scanning two-photon microscope by first considering the optical invariant at the back aperture and front focal plane of an isolated objective lens:

$$I = r \sin\theta = nF \sin\alpha \tag{2.1}$$

where I is the optical invariant, r and θ are the beam radius and incident angle of collimated light at the aperture plane, F and α are the field radius and angle of the cone of light at the image plane, and n is the index of refraction of the immersion fluid of the objective (Fig. 2.1(a)) [77-79]. These parameters are usually defined by manufacturers in terms of the objective's NA, magnification, and field number, which we relate to F, θ, and α in the next section. Eq. 2.1 assumes that the optical system is aplanatic and is a more accurate definition of the optical invariant for microscopes in comparison to the paraxial definition (Appendix B).

We begin by assuming an ideal laser scanning microscope with invariant equal to the invariant of the objective in isolation. In order to scan the FOV of the objective, a laser beam with radius r_1 incident upon a mirror scanner (e.g. galvanometer) is relayed onto the back aperture of an objective lens (Fig. 2.1(b)). The full resolution of the objective lens is achieved by expanding the beam to fill the back aperture. Emission from the sample is then separated with a dichroic mirror and collected onto a photodetector, typically a photomultiplier tube (PMT).

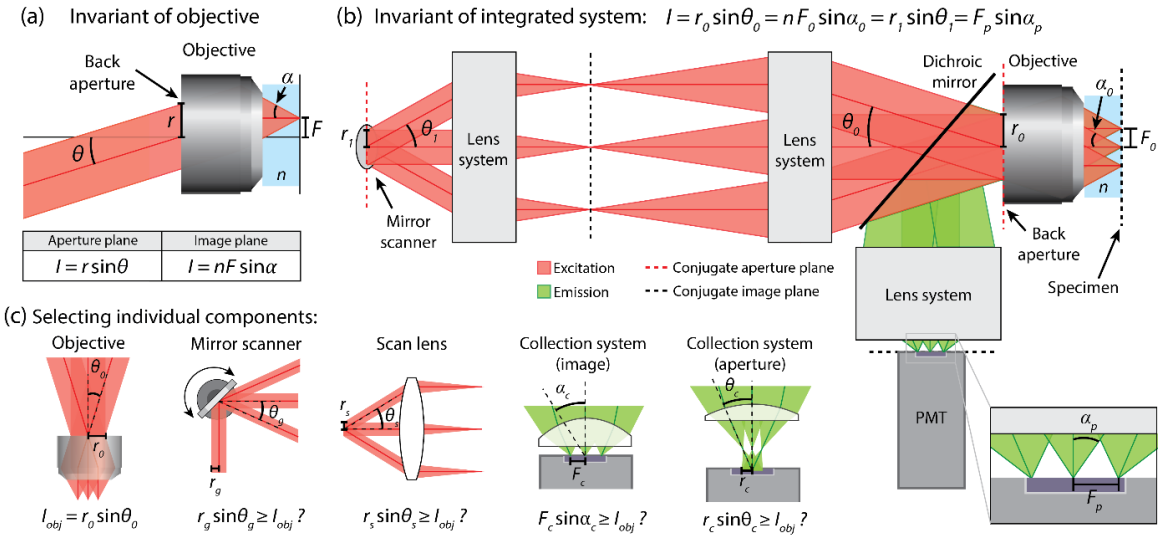

Fig. 2.1. Optical invariant in laser scanning two-photon microscopy. (a) Objective lens with focal length f_0 modeled as a paraxial lens. A collimated beam is directed to the back aperture of an objective that focuses the beam a distance F from the optical axis depending on the angle θ_0 (Eq. 2.4). (b) Basic laser scanning two-photon microscope. The invariant at the back aperture is equal to the invariant at the mirror scanner and the photocathode in aberration free, lossless system. (c) Individual components in microscope can be isolated by comparing the invariant of the objective to the invariant of the component. For the system to be limited by objective performance, invariant of component in isolation must be greater than or equal to invariant of objective.

At this point, it is useful to analyze the optical invariant at conjugate aperture planes, which are the back aperture plane of the objective and the optical scanner plane

$$r_0 \sin\theta_0 = r_1 \sin\theta_1 \tag{2.2}$$

where r_0 and θ_0 are the beam radius and angle of collimated light at the back aperture, and r_1 and θ_1 are the beam radius and scan angle at the mirror scanner. This simple relationship provides a quick and intuitive guide for comparing the demands of the objective lens to other components (e.g. galvanometers and scan lenses) in the microscope.

The challenge of designing an emission collection system for LF-TPM can also be approached by comparing the optical invariant at the specimen and the PMT photocathode:

$$n_0 F_0 \sin\alpha_0 = n_p F_p \sin\alpha_p \tag{2.3}$$

where F_0 and α_0 are the field radius and angle of the cone of emission light entering the objective, and F_p and α_p are the sensor radius and angle of the cone of light exiting the collection optics (Fig. 2.1(b)). Note that the NA of an optical subsystem is equal to $n \sin\alpha$, so Eq. 2.3 can also be written as $F_0 NA_0 = F_p NA_p$. Alternatively, the collection system can be designed by considering the photocathode of the PMT at an aperture plane conjugate to the back aperture of the objective [44]. For the system to be limited by the objective, the component's invariant in isolation must be greater than or equal to the invariant of the objective lens (Fig. 2.1(c)).

2.1.2 LF-TPM Requires Objective Lenses with High Throughput

Before selecting scanning optics and a scanner for the microscope, we needed to identify commercially available objectives suitable for large FOV imaging. The FOV of commercially available objective lenses is usually defined in terms of their field number *FN* and magnification $M = f_t / f_o$ where f_t is the focal length of the tube lens for which the objective is designed and f_0 is the focal length of the objective. The diameter of the FOV ($2F_0$) that an objective lens is designed

to image is then proportional to the focal length of the objective lens and the sine of the angle of collimated light at the back aperture θ_0 for an aplanatic system.

$$2F_0 = \frac{FN}{M} = 2f_0 \sin\theta_0 \tag{2.4}$$

To find candidate objectives for LF-TPM, we compared the specifications of 45 commercially available Olympus objectives (Olympus, Tokyo, Japan) (Appendix C, Fig. 2.2). For this analysis, the lateral resolution of a two-photon microscope was defined as the full width half maximum (FWHM) of the excitation PSF squared:

$$r_{xy} \approx 0.38\frac{\lambda_{ex}}{NA} \tag{2.5}$$

where *NA* is the numerical aperture of the objective and λ_{ex} is the excitation wavelength, which was set to 800nm [12]. The expected axial resolution of the objective was defined as the full width half maximum (FWHM) of the axial profile of the excitation PSF squared:

$$r_z \approx 0.63\frac{\lambda_{ex}}{n - \sqrt{n^2 - NA^2}} \tag{2.6}$$

where n is the index of refraction, *NA* is the numerical aperture, and λ_{ex} is the excitation wavelength, which was set to 800nm. The back aperture diameter was calculated with:

$$BA = 2r = \frac{2f_t NA}{M} \tag{2.7}$$

where M is the magnification of the objective lens [45]. The field number angle θ_{FN} is the angle of the incident collimated light at the back aperture required for imaging the field-of-view (FOV):

$$\theta_{FN} = \sin^{-1}\left(\frac{FN}{2f_t}\right) \tag{2.8}$$

where *FN* is the field number of the objective lens and f_t is the focal length of the tube lens. To calculate the invariant of the objective, Eq. 2.1 can be written in terms of the objective specifications:

$$I = \frac{NA \cdot FN}{2M} \tag{2.9}$$

As expected, the NA generally follows an inverse relationship with the focal length of the objective with deviations due to differences in the throughput of the objectives (Fig. 2.2(a)). By plotting the resolution versus FOV using Eq. 2.4 and 2.5, we were able to find objectives that deviated from the approximately linear trade-off between FOV and resolution (Fig. 2.2(b)). The Olympus XLFluor4X (NA 0.28, f = 45mm) and MVPLAPO 2XC (NA 0.5, f = 45mm) macro-objectives provide large FOV (>5mm) while maintaining sub-cellular resolution in comparison to all objectives analyzed, and were therefore selected for developing LF-TPM. For reference, an objective lens commonly used for *in vivo* TPM, the Olympus XLUMPLFLN 20X (NA 1.0, f = 9mm), is also labeled.

To assess the amount of information that could be transmitted by these objective lenses, the two-dimensional space-bandwidth product (SBP) was also calculated:

$$SBP = \frac{A_{FOV}}{A_{pix}} = \frac{\left(\sqrt{2}F_0\right)^2}{s_{pix}^2} = \frac{2F_0^2}{\left(\frac{r_{xy}}{2}\right)^2} = 8\left(\frac{F_0}{r_{xy}}\right)^2 \tag{2.10}$$

where A_{FOV} is the area of the FOV, A_{pix} is the area of the pixel, and s_{pix} is the size of the pixel. The SBP is the area of the FOV divided by the area of the pixel required for sufficiently sampling the FOV without aliasing, and can be conceptualized as the maximum number of pixels (i.e. information) that can be transmitted by an objective lens or imaging system (Fig. 2.2(c)). In Eq. 2.10, the SBP is calculated using the rectangular FOV so that it is more easily comparable to

existing microscopy systems. By plugging Eq. 2.4 and 2.5 into Eq. 2.10, the SBP can also be expressed in terms of objective parameters:

$$SBP = 55.4\left(\frac{NA \cdot FN}{2M \cdot \lambda_{ex}}\right)^2 = \frac{55.4}{\lambda_{ex}^2} I^2 \tag{2.11}$$

It is apparent from Eq. 2.11 that the SBP is proportional to the optical invariant squared (i.e. the throughput), demonstrating that optimization of the optical invariant in an integrated system also results in the optimization of the information transmitted. The macro-objectives considered for LF-TPM can potentially transmit 3 to 6 times more information than other commercially available objectives we analyzed (Fig. 2.2(d)). In general, commercially available low-magnification objectives transmit more information than high-magnification objectives because they have higher throughput.

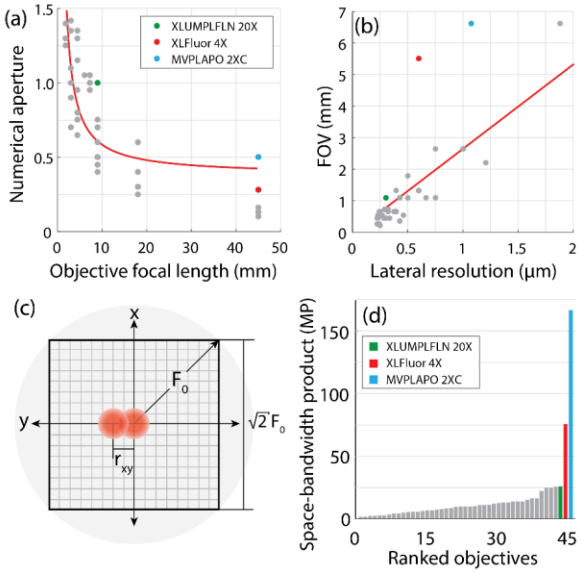

Fig. 2.2. Selecting objective lenses for LF-TPM. (a) Numerical aperture plotted against objective focal length for 45 commercially available Olympus objectives. Red curve is the best fit for the NA's inverse relation to the focal length of the objective. (b) The FOV plotted as a function of the resolution of the objective lens. Two objectives are candidates for LF-TPM (XLFluor 4x and MVPLAPO 2XC). Red curve is the best fit for the FOV's linear relation to the lateral resolution. (c) Diagram of circular FOV (gray) and intensity PSF squared (pink). The rectangular FOV and pixels required for sufficient sampling are also shown. (d) The space-bandwidth product of the 45 objective lenses.

2.1.3 Applying the Optical Invariant for Determining Galvanometers Suitable for LF-TPM

With candidate objective lenses selected, potential scanners and relay optics can be evaluated to see if they will support an invariant equal to or greater than the maximum invariant of the candidate macro-objective lenses. The invariant of the Olympus XLFluor4X, with back aperture of 25.2mm and max field angle of 4.2°, is 0.92mm, and the invariant for the MVPLAPO 2XC, with back aperture of 45mm and max field angle of 3.5°, is 1.37mm.

We computed the maximum optical invariant of mirror galvanometers and polygons (Table 2.1) and compared them to the invariant at the back aperture of the objective lenses. While resonant and polygonal mirror scanners are faster than traditional mirror galvanometers, they generally have lower throughput that do not match the demands of the objective. For this large FOV microscope, we therefore chose to use traditional mirror galvanometers, not resonant or polygon scanners. Although fast scanners typically have lower throughput than the objective lens, there are two solutions to using them in a LF-TPM system. First, a microscope can consist of multiple scanning arms per scanning direction, which adds to the complexity of the optical design or requires unique scanning solutions such as a virtually conjugated scanning galvanometer pair [65]. Alternatively, a smaller FOV or lower NA objective can be used that matches the throughput of the scanner. A resonant scanner (CRS4k, Cambridge Technologies) only has a maximum invariant 0.86 times smaller than the macro-objective used in our system, and could therefore be used with that objective if the objective is underfilled or scanning a smaller FOV.

Table 2.1 Optical invariant of commercially available scanners and objectives

Scanners

Component	Part number	Vendor	Input beam dia. (mm)	Max scan angle (half angle, °)	Max invariant (mm)
Resonant scanner 4kHz	CRS4K	Cambridge Technologies	9.0	10.0	0.78
Resonant scanner 8kHz	CRS8K	Cambridge Technologies	5.0	7.5	0.33
Resonant scanner 12kHz	CRS12K	Cambridge Technologies	5.0	5.0	0.22
Galvanometer scanner (1D)	6240HM40A	Cambridge Technologies	20.0	20.0	3.42
Resonant scanner 8kHz	SC-30	Electro-optical Products Corp.	5.0	6.0	0.26
Polygonal mirror scanner	DT-36-250-025	Lincoln Laser	2.7	5.0	0.12
Polygonal mirror scanner	DT-18-250-025	Lincoln Laser	6.4	10.0	0.56
Galvanometer scanner (2D)	GVS012	Thorlabs	2.0	31.0	0.52
			4.0	27.0	0.91
			6.0	23.0	1.17
			8.0	20.0	1.37
			10.0	10.0	0.87

Objectives

Component	Part number	Vendor	Input beam dia. (mm)	Max scan angle (half angle, °)	Max invariant (mm)
Macro-objective (NA 0.28, f = 45mm)	XLFLUOR4X/340:4X	Olympus	25.2	4.2	0.93
Macro-objective (NA 0.5, f = 45mm)	MVPLAPO 2XC	Olympus	45.0	3.5	1.37

2.1.4 Calculating the Optical Invariant of Scanning Optics

Similar to our selection of beam scanners for LF-TPM, we needed to identify scan optics that could potentially support the invariant at the back aperture of the objective lens. However, the throughput of a scan optic does not remain constant over all input beam diameters (i.e. the performance of the

lens varies with respect to input beam diameter). The max scan angle is typically limited by vignetting at small input beam diameters (Fig. 2.3(a)-(b)) and optical aberrations at large input beam diameters (Fig. 2.3(c)-(d)). We therefore defined the diffraction-limited max scan angle for a given input beam diameter as the scan angle that could be scanned before the beam was either clipped or was no longer diffraction-limited at the image plane (Fig. 2.3(e)-(f)).

To calculate the max invariant as a function of input beam diameter for scan optics, we first modeled scan optics in telecentric configuration using OpticStudio. The spot size over the image plane was calculated for input beam diameters ranging from 1-30mm, and scan angles ranging from 0° to 25°. We adjusted the image plane field curvature to minimize spot size, which enabled us to distinguish increases in spot size due to defocus from spot size increases due to astigmatism, coma, and spherical aberrations. Using OpticStudio, we were able to compare the spot RMS radius to the Airy radius over the FOV. The resolution was consider to be limited by optical aberrations, not diffraction, when the spot RMS radius was greater than the Airy radius. Vignetting data were also recorded to determine the angle at which the beam was less than 100% transmitted by the system, ignoring absorption and reflection of light through the system. To determine the maximum scan angle for a given input beam diameter, the max angle before the beam was clipped was compared to the scan angle at which the spot RMS radius was greater than the Airy radius. Depending on the imaging conditions and lens, the maximum scan angle would be limited by either vignetting or optical aberrations. A full pipeline of our analysis for determining the optical invariant as a function of input beam diameter for isolated scan lenses is included in Table 2.2.

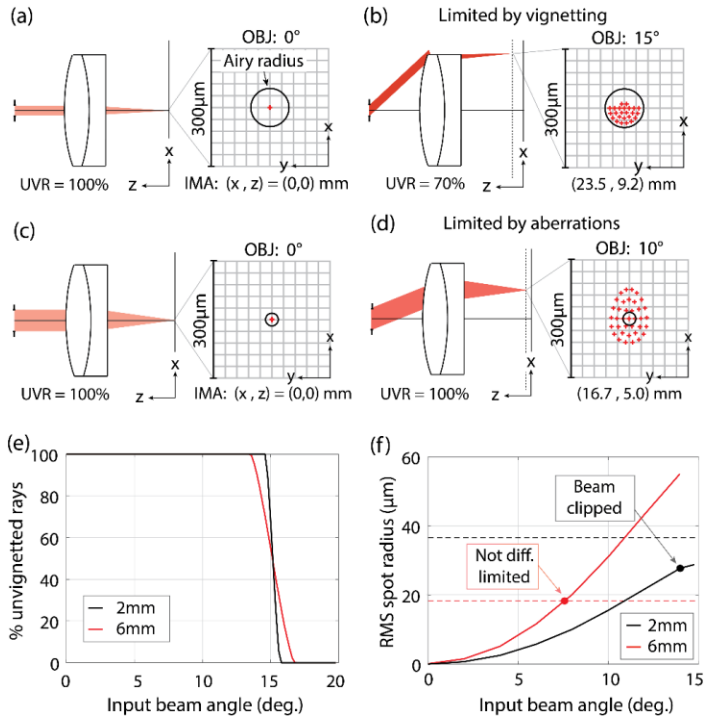

Fig. 2.3. Optical aberrations and vignetting limit the optical throughput of scan optics. (a) Layout and spot diagram of achromatic doublet focusing beam on axis with 2mm beam diameter. The spot size is diffraction-limited and there are 100% unvignetted rays (UVR) at the image plane. Layout is not to scale. (b) Same as (a), scan angle of 15°. 30% of the rays are clipped and do not reach the image plane. (c) Layout and spot diagram for achromatic doublet with input beam diameter of 6mm. (d) Same as (c), but for scan angle of 10°. The beam is not diffraction-limited at the image plane. (e) Percent of unvignettted rays as a function of input beam angle. (f) RMS spot size radius at the image plane as a function of input beam angle. Dashed black and red lines are diffraction limit for 2mm and 6mm beam diameter, respectively.

2.2 Simulations

2.2.1 Optical Invariant Function of Commercially Available Scan Lenses

We calculated the invariant as a function of input beam diameter for 27 different scan optics with focal lengths ranging from 18mm to 500mm (Fig. 2.4 and Fig. 2.5). The analysis included a variety of designs including plano-convex lenses, NIR achromatic doublets, compound achromatic doublets, and telecentric f-theta scan lenses (Appendix C). As an example, we highlight three scan

lenses: an achromatic doublet, an f-theta scan lens, and a compound achromatic doublet, also known as a Plössl design (Fig. 2.4(a)). Through our processing stream (Table 2.2), the diffraction-limited max scan angle can be plotted as a function of input beam diameter (Fig. 2.4(b) and Fig. 2.5(a)). To better compare the performance of scan optics to the objective and make design decisions, we also determined the component's invariant in isolation as a function of input beam diameter (Fig. 2.4(c) and Fig. 2.5(b)).

Table 2.2 Step-by-step procedure for calculating the invariant function for scanning optics.

Zemax	
Step	**Description**
1	Pick a test optic
2	Model in telecentric configuration
3	Set input beam diameter to 1mm
4	Set fields ranging from 0° to field that beam is clipped by 10%
5	Constrain image surface to paraxial focus
6	Save field curvature and distortion as .txt file
7	Set curvature of image surface to minimize spot size
8	Create merit function to minimize spot size error at image plane
9	Set last surface distance to variable
10	Optimize
11	Record Airy radius for this input beam diameter
12	Record RMS spot size over field
13	Record percent of unvignetted rays over field
14	Increase beam radius by 0.5mm
15	Repeat Step #10-14 until vignetting at every field or spot is limited by optical aberrations at every field
Matlab	
Step	**Description**
1	Set input beam radius for analysis
2	Extract spot size, vignetting, Airy radius, and field curvature data from .txt files
3	Find angle that beam is clipped
4	Find max angle that beam is diffraction limited at image plane
5	Compare angles from Step 3 and 4 to find max scan angle for given input beam diameter
6	Calculate product of max beam angle and radius
7	Increase beam radius
8	Repeat Steps #1-7 until max beam radius is reached
9	Plot invariant versus input beam radius

2.2 Simulations

2.2.1 Optical Invariant Function of Commercially Available Scan Lenses

We calculated the invariant as a function of input beam diameter for 27 different scan optics with focal lengths ranging from 18mm to 500mm (Fig. 2.4 and Fig. 2.5). The analysis included a variety of designs including plano-convex lenses, NIR achromatic doublets, compound achromatic doublets, and telecentric f-theta scan lenses (Appendix C). As an example, we highlight three scan lenses: an achromatic doublet, an f-theta scan lens, and a compound achromatic doublet, also known as a Plössl design (Fig. 2.4(a)). Through our processing stream (Table 2.2), the diffraction-limited max scan angle can be plotted as a function of input beam diameter (Fig. 2.4(b) and Fig. 2.5(a)). To better compare the performance of scan optics to the objective and make design decisions, we also determined the component's invariant in isolation as a function of input beam diameter (Fig. 2.4(c) and Fig. 2.5(b)).

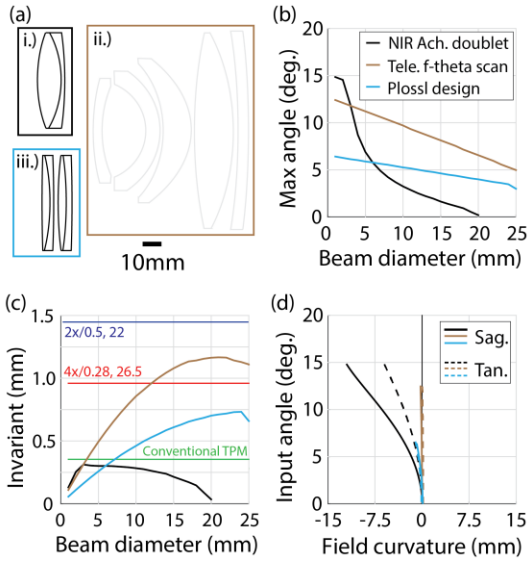

Fig. 2.4. Comparison of scan optics for TPM and LF-TPM. (a) Layout of i.) achromatic doublet (AC508-100-B, Thorlabs), ii.) telecentric f-theta lens (64-422, Edmund Optics), and iii.) compound achromatic doublet (AC508-400-B and AC508-500-B, Thorlabs). (b) Max scanning angle of each optic as function in input beam diameter (c) Optical invariant plotted versus input beam diameter. (c) Sagittal (sag.) and tangential (tan.) curvature at image plane.

The invariant of a common scan optic, an achromatic doublet (efl = 100mm; AC508-100-B, Thorlabs, Newton, USA), matches the invariant required for conventional TPM, but is unable to support the demands of the macro-objective lenses and therefore generally fails as a scan lens in LF-TPM (Fig. 2.4). Here we consider a conventional TPM system as one that is capable of imaging a FOV diameter of 707μm with the Olympus XLUMPLFLN 20X (i.e. $I = 9\sin(2.25°) = 0.35mm$).

Of the 27 lenses, we highlight two of the best performing: a compound achromatic doublet lens system (efl = 222mm; AC508-400-B and AC508-500-B, Thorlabs) and a telecentric f- theta scan lens (efl =115mm; 64-422, Edmund Optics, Barrington, USA)) (Fig. 2.5(a)-(b)). These lenses are labeled as L15 and L27 in Appendix C, respectively, and will be referred to as such in the main text for brevity. Both L15 and L27 are close to matching the invariant at the back aperture of the macro-objective lenses for beam diameters greater than 8mm and 16mm, respectively. These two lens systems also have minimal field curvature at the image plane in comparison to the single achromatic doublet (Fig. 2.4(d)).

In addition to identifying scan lenses with high throughput, we must also consider the ratio of the focal lengths of the two lenses in order to determine if two lenses will function well as a scan relay (Fig. 2.5(c)). Therefore, the performance of the first lens in the relay with input beam diameter d_{in} must be compared to the performance of the second lens in the relay with beam diameter Md_{in} at its aperture plane, where M is the ratio of the focal lengths of the lenses. The results from our analysis demonstrate that L15 and L27 have comparable invariants in isolation when considering the magnification of the beam in the relay (Fig. 2.5(b)), implying that a relay consisting of these lenses is a good candidate for LF-TPM.

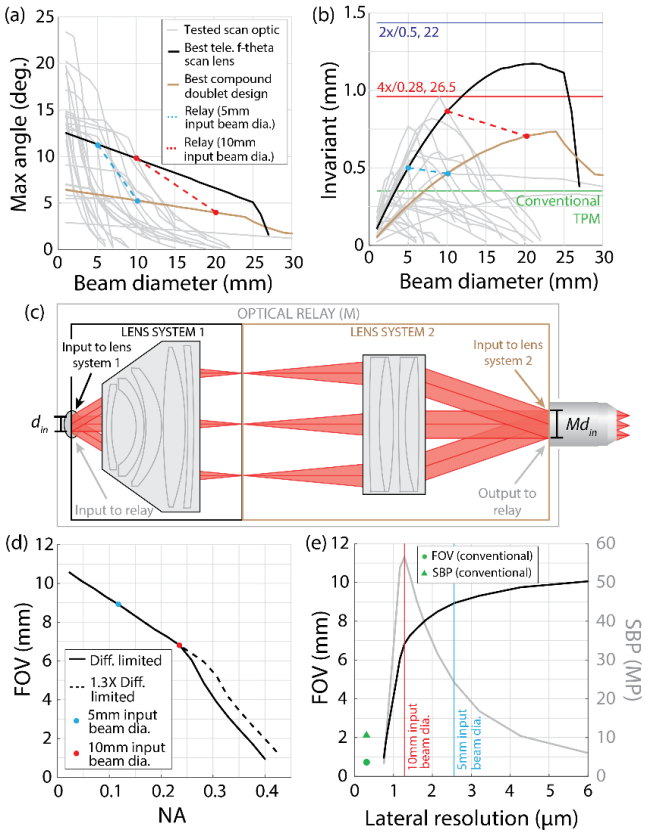

Fig. 2.5. Calculating the invariant for scan optics and selecting scan relays. (a) Max scan angle calculated as a function of input beam diameter for 27 scanning lenses. Highlighted are the best performing telecentric f-theta scan lens and compound doublet designs. Also shown by the dashed lines are two operating conditions for a relay consisting of these two lenses for input beam diameter of 5mm and 10mm (b) Invariant for 27 scanning lenses plotted as function of input beam diameter. The invariant at the back aperture for two macro-objectives and in a conventional TPM system are also shown. The dashed lines show the operating points of the relay highlighted in (a). (c) Schematic of analyzing invariant of scan optics in isolation and integrated in optical relay. d_{in} is the input beam diameter and M is the magnification of the relay. (d) Expected FOV plotted versus excitation NA for relay highlighted in (a)-(c). (e) Expected FOV (black curve) and SBP (gray curve) plotted against expected resolution.

The evaluation of the throughput of individual lenses is also useful in comparing the performance of different iterations in lens design. For example, we calculated the optical invariant as a function of input beam diameter for four compound achromatic doublet lenses designs consisting of the same two achromatic doublets but with different lens orientations to identify the

best performing design (Fig. 2.6). We analyzed six different combinations of achromatic doublets (L13-L18 in Appendix C.2) with the best performing configuration shown in Fig. 2.6. All designs had a spacing of 2mm between achromatic doublets.

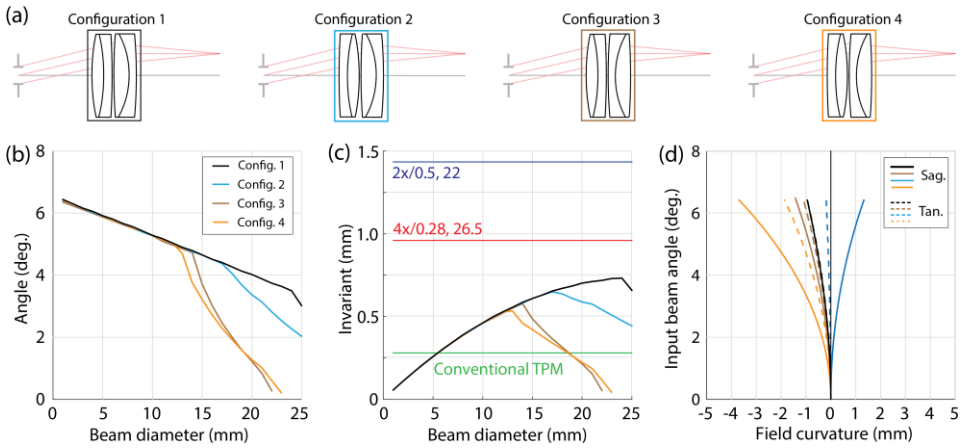

Fig. 2.6. Performance of compound achromatic doublets with different configurations. (a) Diagram of two achromatic doublets arranged in four possible configurations. (b) Maximum scan angle as a function of input beam diameter to the lens system. (c) Invariant of four lens configurations as a function of input beam diameter. The invariant at the back aperture of two macro-objectives and for conventional TPM are also shown. (d) Sagittal (sag.) and tangential (tan.) field curvature at the image plane for the four configurations.

2.2.2 Integrating Optical Subsystems

Once candidates have been analyzed in isolation, it is necessary to evaluate the performance of the lenses together in a relay. The relay was analyzed with its output at the back aperture of an objective lens modeled as a paraxial lens with focal length of 45mm. We evaluated the performance of the relay over input beam diameters between 1mm and 18mm. The excitation NA of the objective in this model depends on the diameter of the beam at the back aperture, which is equal to the magnification of the relay (M = 2.1) multiplied by the input beam diameter. From this analysis, we calculated the expected FOV that could be imaged by the system as a function of the effective excitation NA of the objective lens (Fig. 2.5(d)) and expected lateral resolution (Fig.

2.5(e)). The SBP is also plotted to determine the imaging conditions that optimize the microscope's information transmission, which is maximum at input beam diameter of around 10mm.

Due to the lower invariant of the compound achromatic doublet subsystem, our relay does not support the full invariant of the macro-objective lenses and thus the back aperture will be either underfilled, limiting resolution, and/or the FOV will be limited. We therefore selected two potential designs: (1) excitation NA 0.11 and 9mm FOV diameter and (2) excitation NA 0.22 and 7mm FOV diameter. These two designs can be achieved with the same relay by simply changing the beam magnification before the microscope such that the input beam diameter is either 5mm or 10mm (Section 2.3). Design 2 is the imaging condition with maximum SBP, and is expected to be around 5 times greater than the SBP in conventional TPM (Fig. 2.5(e)). Note that the collection NA is the same for both designs and is equal to the full NA of the objective lens, which is 0.28.

Until this stage of the design, we have focused on selecting potential scan optics for LF-TPM and evaluating their performance together in a single relay. To scan in two directions, the microscope must either have a 2D galvanometer or two scanners separated by another afocal relay. Both of these designs have their advantages and disadvantages. Any addition of scan optics to a system will increase the complexity of the microscope and will make it more difficult to minimize optical aberrations. On the other hand, a 2D galvanometer system may introduce beam clipping at large scan angles and thus decrease the scannable FOV of the microscope. We therefore compared the invariant of a microscope with the single relay and 2D galvanometer to the invariant of a microscope with two relays and two separated mirror galvanometers.

In both cases, we used the same relay consisting of L15 and L27. For the two relay system, we needed to add another afocal relay. We opted to model this second scanning arm with two different relays with unity magnification: (1) two telecentric f-theta scan lenses (relay 1A; Edmund Optics,

64-422) and (2) two other telecentric f-theta scan lenses (relay 1B; Thorlabs, LSM05-BB) (Fig. 2.7). A unity magnification relay was chosen because the best performing relay can be achieved using f-theta scan lenses. This type of relay could not be used in the first relay because telecentric f-theta scan lenses have short distance between the stop and first element in the system, which precludes the positioning of a dichroic mirror between the objective and scan system.

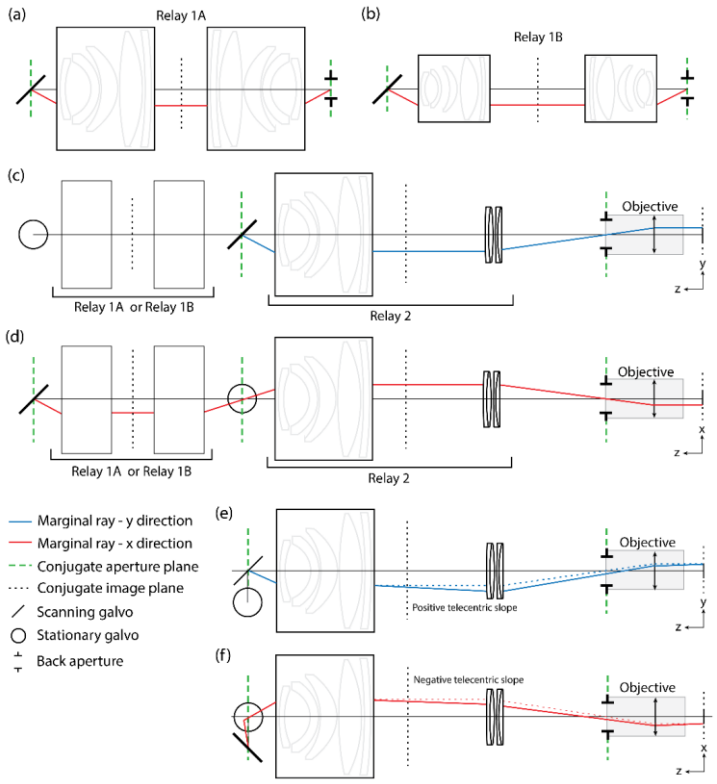

Fig. 2.7. Schematics of laser scanning microscopes with one or two relays. (a) Diagram of Relay 1A, consisting of two telecentric f-theta scan lenses (efl =115mm; Edmund Optics, 64-422). (b) Diagram of Relay 1B, consisting of two telecentric f-theta scan lenses (relay 1B; Thorlabs, LSM05-BB). (c) Schematic of two relay laser scanning microscope with relay 1A or relay 1B scanning in the x-direction, and the high throughput relay shown in Fig. 2.5 scanning in the y-direction. The objective is modeled as a paraxial lens. (d) Same as (c), but showing only the marginal ray in the x-direction. (e) Schematic of one relay microscope with 2D galvanometer. Blue line is marginal ray in the y direction. Note that positive telecentric slope is introduced in the y-direction due to the aperture stop being positioned between the galvanometers. (f) Same as (e), but for the x-direction. Because the scanning is beyond the focal plane of the scanning lens, there is negative telecentric slope in the x-direction.

For the one relay system, a 2D galavanometer was modeled by placing the back focal plane of the first scan lens between two mirrors with the aperture stop positioned at the first mirror. We also compared this model to the same system without the 2D galvanometer (i.e. the aperture stop was positioned at the back focal plane of the first scan lens). These scanning systems were analyzed with their output at the back aperture of an objective lens modeled as a paraxial lens with focal length of 45mm.

We evaluated the performance of the relay over input beam diameters between 1mm to 18mm. The excitation NA of the objective in this model depends on the diameter of the beam at the back aperture, which is equal to the total magnification of the relays (M = 2.1) multiplied by the input beam diameter. From this analysis, we calculated the expected FOV that could be imaged by the system as a function of the effective excitation NA of the objective lens (Fig. 2.8(a)). We also calculated the invariant of these systems as a function of the input beam diameter (Fig. 2.8(b)).

These results show that the beam is clipped by the 2D galvanometer for beam diameters greater than 10mm in the one relay system. However, the addition of a second relay introduces optical aberration that limit the performance of the microscope, especially for relay 1B. This analysis demonstrates that a single relay system simplifies the design, while maintaining similar performance to a system consisting of two afocal relays.

Due to the fact that it is more challenging and expensive to construct a microscope with two relays, we opted to implement a LF-TPM system with a single relay consisting of L15, L27, and a 2D galvanometer (GVS012, Thorlabs). This galvanometer matches the invariant at the back aperture for input beam diameter ranging from 4-10mm.

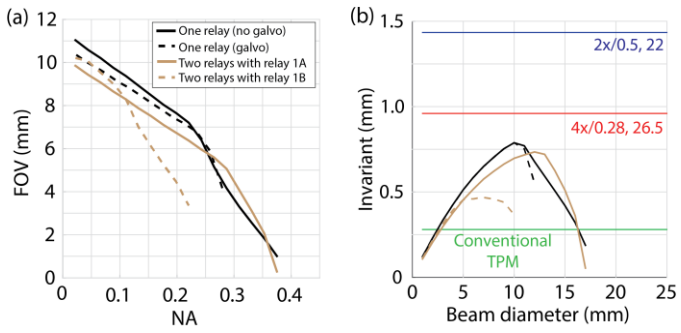

Fig. 2.8. Performance of one relay and two relay designs are similar. (a) Expected FOV versus excitation NA for the four systems shown in Fig. 2.7. Systems were tested with the objective lens modeled as a paraxial lens. The one relay system was tested with the stop conjugate to the back aperture of the objective with no account for beam clipping due to the 2D galvanometer. (b) Invariant of systems plotted as a function of input beam diameter. The invariant at the back aperture of two macro-objectives and for conventional TPM are also shown. The optimal performance of the one relay system is with input beam diameter of 10mm, and is similar with and without accounting for beam clipping at the mirror galvanometer.

Our final analysis in analyzing the optical invariant of integrated microscopy systems, we modeled a one relay microscope with achromatic doublet lenses used for the scan lens (AC508-75-B, Thorlabs) and tube lens (AC508-200-B, Thorlabs) (Fig. 2.9(a)). The total magnification of the system is 2.67. To compare the invariant of the optics in isolation to the integrated microscope, the magnification must be considered (i.e. the invariant of the tube lens in isolation must be plotted against the input beam diameter divided by the magnification so that it is in reference to the input of the entire microscope). The invariant of the integrated microscope closely matches the invariant of the scan lens in isolation (Fig. 2.9(a)-(b)). This results supports the concept that the optical component with the lowest invariant in isolation will set the invariant of the integrated system.

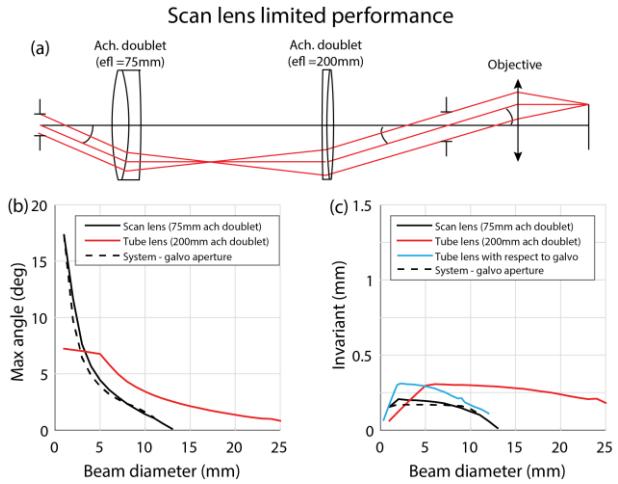

Fig. 2.9. Integrated microscope limited by scan lens. (a) Layout of microscope consisting of two achromatic doublets for relay lenses. The performance of system is limited by the scan lens, which is an achromatic doublet with focal length equal to 75mm. Layout is not to scale. (b) Zemax similuations showing the max scan angle as a function of input beam diameter for the two relay optics in isolation as well as the integrated system. (c) Invariant plotted as function of input diameter for data in (b). The performance of the integrated system matches the invariant of the scan lens in isolation, implying that the scan lens is limiting component in system.

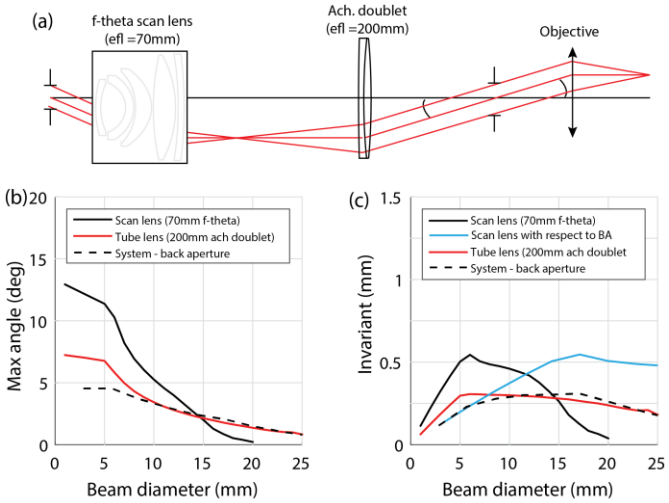

Fig. 2.10. Microscope with limiting component dependent on operating conditions. (a) Layout of microscope consisting of a f-theta telecentric scan lens and achromatic doublet. Layout is not to scale. (b) Zemax similuations showing the max scan angle as a function of input beam diameter for the two relay optics in isolation as well as the integrated system. The system invariant is plotted with respect to the beam diameter at the back aperture. (c) Invariant plotted as function of input diameter for data in (b). The limiting component in the system depends on the beam diameter. The scan lens is plotted with respect to both the galvanometer and the back aperture.

We modeled another system that replaced the scan lens with a telecentric f-theta lens (LSM05-BB, Thorlabs) (Fig. 2.10(a)). The total magnification of the system was 2.85. For beam diameters less than 7mm, the microscope is limited by the scan lens (i.e. the invariant of the integrated microscope is equal to the invariant of the scan lens). For beam diameters greater than 7mm, the microscope is limited by the tube lens (i.e. the invariant of the integrated microscope is equal to the invariant of the tube lens) (Fig. 2.10(b)-(c)).

2.2.3 Collection Systems

A collection system can be designed by considering the photocathode of the PMT at an aperture plane conjugate to the back aperture of the objective or conjugate to the front focal plane of the objective (Fig. 2.1c). The emission NA is the full NA of the objective lens, which may be different than the excitation NA. Although diffraction-limited image quality is not required at the photocathode, it is still difficult to design collection optics with high NA. Firstly, the conservation of the optical invariant is only valid in aberration-free systems, so if the collection system is not diffraction limited this method will serve only as a general guideline, and full energy transmission may require higher NA than predicted by analyzing the invariant. Minimizing aberrations and stray light becomes increasingly difficult with higher NA. Secondly, high NA systems generally have short working distance and shallow depth of field, making it difficult to mount and align the PMT after the collection system. Therefore, it is advantageous to use low NA collection systems. We therefore compared the NA of collection systems conjugate to the back aperture to the NA of collection systems conjugate to the specimen.

If the photocathode of the PMT is conjugate to the specimen plane, then Eq. 2.3 can be used to determine the approximate collection NA necessary by setting *Fs* equal to the radius of the photocathode [65]:

$$NA_i = \frac{I_{obj}}{r_1} = \frac{F_o NA}{r_1} \tag{2.12}$$

where NA_i is the NA of the collection system conjugate to the image plane, I_{obj} is the objective invariant, F_o is the FOV radius, NA is the numerical aperture of the objective, and r_1 is the radius of the photocathode (Fig. 2.11(a)).

If the photocathode is conjugate to the aperture stop of the objective, then the exit pupil of the system coincides with the photocathode (Fig. 2.11(b)). The magnification of the system M is equal to r_o/r_1, where r_o is the radius of the back aperture. A collection system with photocathode conju-

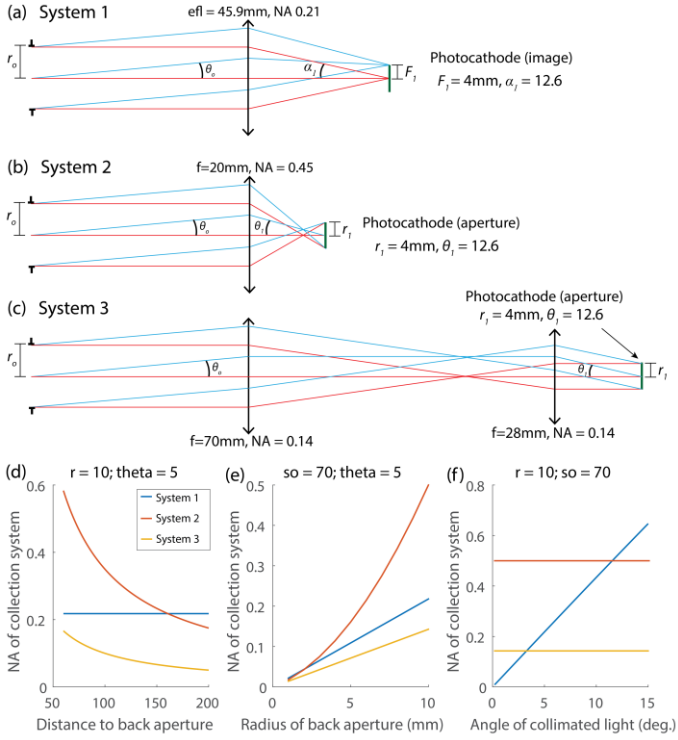

Fig. 2.11. Collection system designs. (a) Layout of collection system with light focused onto the PMT. The emission from the sample is modeled as light exitting the back aperture with radius r_0 and angle θ_0. Collection conditions require a single lens with NA 0.21. (b) Layout of collection system with PMT coinciding at exit pupil. For the same collection conditions, this system requires a single lens with NA 0.45. (c) Layout of collection system that relays back aperture onto PMT with two lenses. The NA of both lenses is equal to 0.14. (d) NA of the three collection systems plotted as a function of distance to back aperture. (e) NA of collection systems plotted as function of beam radius at back aperture. (f) NA of collection systems plotted as function of angle of collimated light at back aperture.

gated to back aperture can be achieved using a single lens system. Assume that the collection system is aplanatic, and let the distance between the back aperture and first principal point of the first lens be s_o. Often s_o is minimized in the microscope so that the first collection lens is as close as possible to the back aperture to improve collection efficiency. The effective focal length of such a collection system can be determined by plugging in s_o and $s_i=Ms_o$ into the thin lens equation. Thus, the NA of the single lens system used for collection is given by:

$$NA_a = r_o\left(\frac{1}{s_o}+\frac{1}{Ms_o}\right)=\frac{r_o}{s_o}+\frac{r_o^2}{s_o r_1} \tag{2.13}$$

where NA_a is the numerical aperture of a single lens system, r_o is the radius of the back aperture, s_o is the distance between the lens system and the back aperture, and r_1 is the radius of the photocathode.

Alternatively, if the emission from the back aperture is relayed onto the photocathode with a telecentric telescope (Fig. 2.11(c)), then we can determine the approximate NAs of the two lenses in the relay [44]. In a telecentric telescope, s_o is equal to the focal length of the first lens and the focal length of the second lens is determined by the magnification required of the relay. Therefore,

$$NA_{r1}=\frac{r_o}{f_1}=\frac{r_o}{s_o} \tag{2.14}$$

$$NA_{r2}=\frac{r_1}{f_2}=\frac{r_o}{s_o} \tag{2.15}$$

where NA_{r1} is the NA of first lens in the collection relay, f_1 is the focal length of the first lens in the collection relay, NA_{r2} is the NA of second lens in the collection relay, and f_2 is the focal length of the second lens in the collection relay. Eq. 2.14 and 2.15 show that the NA of the two lenses in a collection relay have the same NA.

With Eq. 2.12, 2.13, 2.14, and 2.15, we can now determine the collection NA necessary for collecting emission from the sample onto the photocathode using these three different designs: (1) photocathode conjugate to specimen, (2) photocathode conjugate to back aperture with single lens system, and (3) photocathode conjugate to back aperture with optical relay consisting of two lens systems (Fig. 2.11(d)-(e)). Remember that in all cases that the invariant at the photocathode is equal to the invariant at the back aperture if the system is diffraction limited. For example, we show the optics necessary for collecting light from a back aperture with radius 10mm and angle of collimated light of 5° using these three different designs. We also calculated the NA required as a function of distance to the back aperture, radius of the back aperture, and angle of collimated light at the back aperture. In most cases, an optical relay will lower the NA of the collection lenses necessary to relay light from the back aperture onto the photocathode.

For our imaging conditions, we decided to design the collection system by positioning the photocathode of the PMT at a plane conjugate to the specimen plane. We modeled potential collection systems with light exiting an aperture with a diameter of 25.2mm at an angle of 5.7° and a photocathode with 8mm diameter (R12829, Hamamatsu, Hamamatsu City, Japan). Using Eq. 2.3, we predicted a collection system NA_{coll} of 0.31 ($I = 12.6\sin(5.7°) = 1.25mm \rightarrow NA_{coll} = \frac{1.25}{4} = 0.31$). The collection system for our microscope consists of three plano-convex lenses and has an NA of 0.33. Because the collection system is not diffraction limited, the photocathode is positioned between the image plane and exit pupil of the collection system, not directly at the image plane. There is no expected vignetting of the emission for imaging conditions without scattering when using the Olympus XLFluor4X, and only 14% clipped rays when imaging off axis with the MVPLAPO 2XC objective.

2.3 Implementation

The final LF-TPM system includes a Ti:Sapphire (Ti:S) laser (Mai Tai HPDS, Spectra Physics, Santa Clara, USA) with an electro-optic modulator (350-80-LA-02, Conoptics, Danbury, USA) and prism compensation for controlling the laser intensity and dispersion at the sample (Fig. 2.12), respectively. Before the PMT, the emission from the sample is separated with a dichroic mirror (FF775-Di01-60x84, Semrock, Rochester, USA) and emission filters (FF01-680/SP-50.8-D, Semrock and ET525/36m, Chroma, Foothill Ranch, USA). The signal is then amplified with a transimpedance amplifier (TIA60, Thorlabs) and digitized (PCIe-6353, National Instruments, Austin, USA) before a computer. Control of the electronics and image construction are then performed using custom written software (MATLAB, MathWorks, Natick, USA). All component distances are shown in Table 2.3.

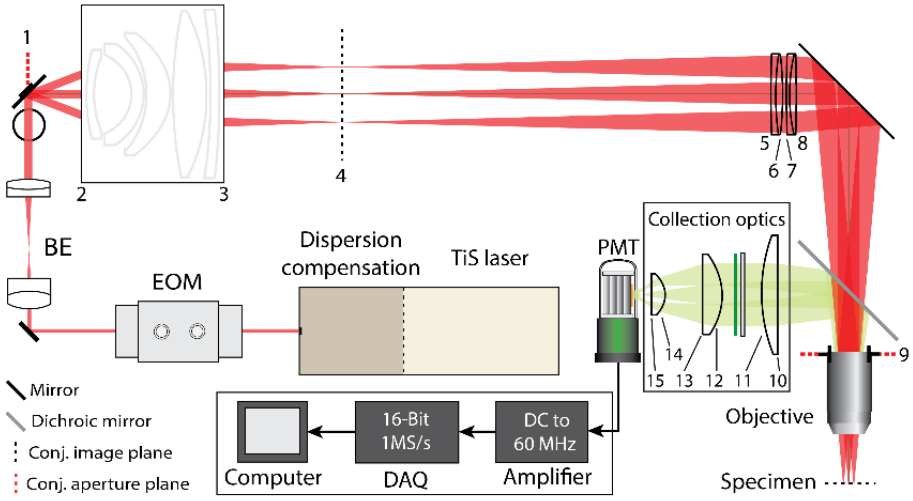

Fig. 2.12. LF-TPM system schematic. Pulsed light from TiSapphire (TiS) laser is directed to the galvanometer and the input of the microscope. Laser intensity and dispersion are controlled with an electro-optic modulator (EOM) and dispersion compension prisms. The beam is then expanded with a beam expander (BE) consisting of two achromatic doublets. Emission is separated with a dichroic mirror and pass both a shortpass and notch filter before being collected by a photomultiplier tube (PMT). The output of the PMT is amplified and digitized before images are displayed on a computer.

Table 2.3 System prescription starting from 2D mirror galvanometer to PMT. Labels are shown Fig. 2.12.

Surfaces	Distance or thickness (mm)	Description	Part	Vendor
1	-	XY galvanometer	GVS012	Thorlabs
1-2	24	-	-	-
2-3	92	Telecentric f-theta scan lens	64-422	Edmund optics
3-4	348	-	-	-
5-6	7.1	Achromatic doublet	AC508-500-B	Thorlabs
6-7	2	-	-	-
7-8	7.1	Achromatic doublet	AC508-400-B	Thorlabs
8-9	208	-	-	-
9	-	Back aperture	XLFluor4X	Olympus
9-10	100	-	-	-
10-11	10.1	Collection lens 1	LA1353-A	Thorlabs
11-12	25	-	-	-
12-13	12.5	Collection lens 2	LA1145	Thorlabs
13-14	23.4	-	-	-
14-15	15.45	Collection lens 3	LA1805-A	Thorlabs
15-16	12.1	-	-	-
16	-	PMT	R12829	Hamamatsu

2.3.1 Beam Intensity, Expansion, and Dispersion

We modeled our microscope with planar waves and circular apertures in Zemax. The invariant analysis presented in the previous section was limited to conditions for which the microscope was limited by diffraction, which were determined by comparing the Airy radius to the RMS spot size. However, a Ti:S laser is more accurately modeled as a Gaussian beam, rather than planar waves and circular apertures. It is useful to express the complex amplitude of the wave as separate functions of space and time:

$$U(\vec{r},t) = a(\vec{r})\exp[j\varphi(\vec{r})]\exp(j2\pi\upsilon t) = S(\vec{r})T(t) \tag{2.16}$$

$$S(\vec{r}) = A(\vec{r})\exp[j\varphi(\vec{r})] \tag{2.17}$$

$$T(t) = B(t)\exp(j2\pi\upsilon t) \tag{2.18}$$

where U is the complex amplitude, φ is the phase of the wave, υ is the frequency of the light, S is the spatial component of the complex amplitude, T is the temporal component of the complex amplitude, A is the spatial complex envelope, and B is the temporal complex envelope [80]. The spatial distribution of light for a Gaussian beam is

$$S(\rho,z) = A_0\frac{W_0}{W(z)}\exp\left[-\frac{\rho^2}{W^2(z)}\right]\exp\left[-jkz - jk\frac{\rho^2}{2R(z)} + j\zeta(z)\right] \tag{2.19}$$

$$W(z) = W_0\sqrt{1+\left(\frac{z}{z_0}\right)^2} \tag{2.20}$$

$$R(z) = z\left[1+\left(\frac{z_0}{z}\right)^2\right] \tag{2.21}$$

$$\zeta(z) = \tan^{-1}\left(\frac{z}{z_0}\right) \tag{2.22}$$

$$W_0 = \sqrt{\frac{\lambda z_0}{\pi}} \tag{2.23}$$

$$A_0 = \frac{A_1}{jz_0} \tag{2.24}$$

where S is the spatial component of the complex amplitude, A_1 is a constant, z_0 is the Rayleigh range, w is the beam waist, w_0 is known as the beam radius (i.e. beam waist at z=0), k is the wave number, and R is the wavefront radius [81]. The intensity of the beam is

$$I(\rho, z) = I_0 \frac{W_0^2 \exp\left(-\frac{2\rho^2}{W^2(z)}\right)}{W^2(z)} \tag{2.25}$$

$$I_0 = |A_0|^2 \tag{2.26}$$

For a CW laser, I_0 can be expressed with respect to the average power

$$I_0 = \frac{2P_{ave}}{\pi W_0^2} \tag{2.27}$$

where P_{ave} is the average power of the laser beam. However, as discussed in Appendix A, a Ti:S laser is typically used in TPM to increase the rate of two-photon absorption because it is a pulsed laser. Therefore, the temporal component of the complex amplitude must be expressed as a pulse train when analyzing the beam intensity. The time-averaged intensity of a pulse convolved with spike train is given by

$$\langle I_0^n(t) \rangle = g^{(n)} \left(\frac{2P_{ave}}{\pi W_0^2}\right)^n = \frac{g_p{}^{(n)}}{(f\tau)^{n-1}} \left(\frac{2P_{ave}}{\pi W_0^2}\right)^n \tag{2.28}$$

where n is the order of the coherence, g is the temporal coherence, f is the repetition rate of the laser, and τ is the full width half max (FWHM) of the pulse. For a Gaussian shaped pulse, $g_p{}^2$ = 0.66 and $g_p{}^3$ = 0.51. For a CW laser, $g^{(2)} = 1$ [80].

Beam Intensity

A polarizing beam splitter (PBS) (PBS122, Thorlabs) and achromatic half wave plate designed for 690-1200nm (AHWP05M-980) were used to coarsely control the intensity of light. Light exiting the Ti:S laser is linearly polarized, so a half-wave plate can be used to adjust the orientation of the polarization. The amount of light that is transmitted by the PBS depends on the orientation of the polarization, therefore turning the half wave plate controls the intensity of light entering the

microscope. A beam dump is positioned at the other output of the PBS to collect light that is not entering the microscope.

Fine control of the beam intensity is achieved by sending a control signal to an electro-optic modulator (EOM). To increase the longevity of the EOM, the bias voltage of the device should be minimized. This is one of the primary motivations to include the PCB and half wave plate to the system. As the beam is scanned across the sample, a blanker can be added using the EOM because the intensity can quickly be adjusted with the control signal. The EOM is calibrated before each experiment by placing a power meter (PM100D, Thorlabs) at the sample plane and varying the control voltage of the EOM. The control voltage is then plotted against the average power at the sample. The average power at the sample was <50mW for all *in vivo* experiments.

Expansion

The designs outlined in Section 2.2.2 require beam expansion before the input of the microscope. We chose to design Keplerian beam expanders with two achromatic doublets with ray optics and Gaussian beam models (Fig. 2.13(a)-(b)). The input beam radius and divergence of the Ti:S laser are 1.2mm and 1.2mrad, respectively, which results in a Rayleigh length of 1m. In a ray optics model, the total magnification of the expander is equal to the ratio of the focal lengths, and the lenses are separated by a distance equal to the sum of their focal lengths. For a more complete model of the beam expansion, we modeled the light as a Gaussian beam propagating through two thin lenses.

The first lens of the beam expander is positioned a distance of approximately 0.5m away from the output coupler of the laser (i.e. $z_L = 0.5$ in Fig. 2.13(b)). The transmission of the Gaussian beam through the first lens results in the following beam properties governed by the magnification of the beam after the first lens:

$$M_1 = \frac{f_1}{(z_L - f_1)\sqrt{1 + \left(\frac{z_0}{z_L - f_1}\right)^2}} \tag{2.29}$$

where M_1 is the magnification of the first lens, f_1 is the focal length of the first lens, z_L is the distance between the coupler and first lens, z_0 is the Rayleigh length of the beam with respect to the coupler. The beam waist after the lens is essentially located at the focal point of the lens

$$z_1 = M^2(z_L - f) + f \tag{2.30}$$

The waist radius and divergence at the focus are given by

$$W_0^{"} = MW_0 \tag{2.31}$$

$$\theta_0^{"} = \frac{\theta_0}{M} \tag{2.32}$$

where $W_0^{"}$ is the beam waist radius at the focus, W_0 is the beam waist radius at the coupler, $\theta_0^{"}$ is the divergence of the beam after the focus, and θ_0 is the divergence at the output coupler [81]. Eqs. 2.29-2.32 can then be applied to the beam propagating through the second lens so that the divergence θ_0', beam waist W_0', and waist location z' after the second lens can be determined as a function of the distance between the lenses. As an example, we modeled a Keplerian beam expander consisting of two lenses with f_1=z_1=30mm, f_2=30mm, and z_L=0.5m. The beam at the output coupler was modeled based on the specifications of the Ti:S laser (W_0 = 1.2mm, θ_0=1.2mrad, λ=800nm).

The divergence of the beam is minimum and magnification of the beam is maximum when the distance between the two lenses is equal to the sum of the focal lengths of the two lenses (Fig.

2.13(d)-(e)). In this case, the beam waist after the second lens coincides with the position of the second lens. As the distance between the two lenses increases, the beam waist location becomes farther from the second lens until the distance between the two lenses is equal to $z_1 + z_2 + W_0^{"}$. After which, the distance between the beam waist and second lens decreases (z' in Fig. 2.13(c)). Ideally, the beam waist after the second lens coincides with the galvanometer, which, in our microscope, is located a distance of approximately 0.6m from the second lens. Therefore, the distance between the two lenses would be slightly larger than the sum of the focal lengths (around

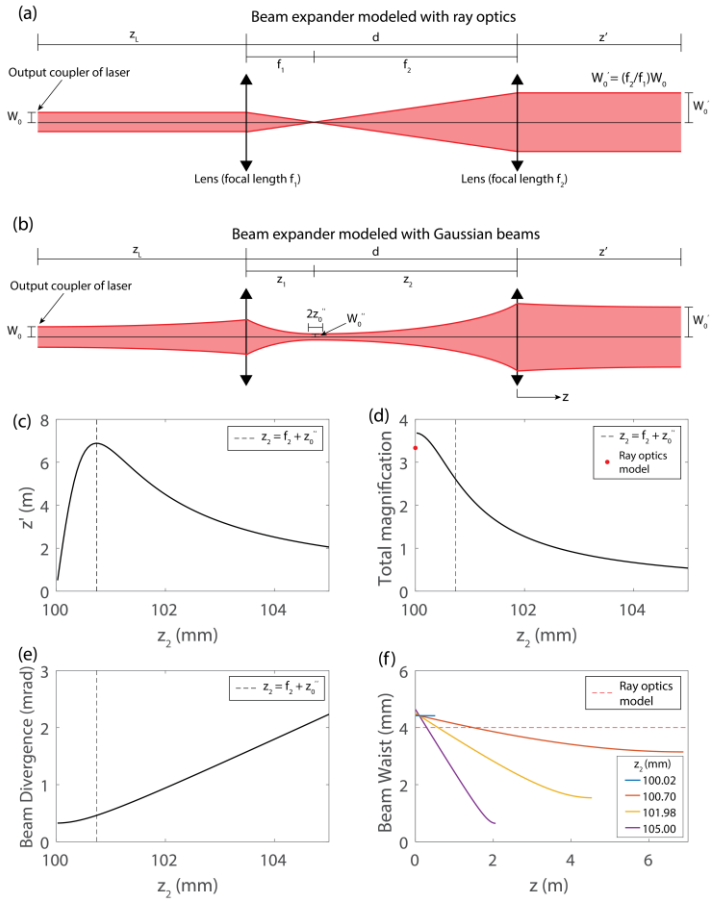

Fig. 2.13. Modeling beam expander with Gaussian beam. (a) Diagram for beam expanison modeled with ray optics. (b) Diagram of beam expansion modeled with Gaussian beam. (c) Location of beam waist from second lens *z'* as a function of z_2, which is maximized when z_2 is equal to the $f_2 + z_0$". (d) Total magnification of the relay as a function of z_2. (e) Beam divergence after the second lens as function of z_2. (f) Beam waist after the second lens for four different values of z_2.

20μm greater than the sum of focal lengths). In practice, adjusting the position with such accuracy is difficult, so the beam diameter should just be examined over distances greater than 1m after the second lens to determine if the beam waist appears constant after the second lens as predicted (Fig. 2.13(f)). When the lenses are separated by a distance equal to the sum of their focal lengths, the magnification predicted with Gaussian beams is actually greater than the magnification predicted with ray optics (Fig. 2.13(d)). Therefore, the ratio of the focal lengths is actual slightly less than the desired magnification of the beam expander

$$\frac{f_2}{f_1} < \frac{W_0'}{W_0} \tag{2.33}$$

where W_0' is equal to the beam waist after the second lens. For our designs, we required total beam expansion of 5 and 10. The first expander consisted of two achromatic doublets with effective focal lengths equal to 30mm and 100mm (AC254-030-B and AC254-100-B, Thorlabs), and the second expander consisted of two achromatic doublets with effective focal lengths equal to 30mm and 200mm (AC254-030-B and AC254-200-B, Thorlabs).

Dispersion

Because the rate of two-photon absorption is proportional to the intensity squared, the pulse duration should be minimized (Eq. 2.28) [80]. In dispersive media (e.g. glass in lenses) the pulse will broaden and thus decrease the rate of two-photon absorption. To prevent this from occurring, the pulse is "pre-chirped" before the microscope with prisms (Deep See, Spectra Physics). A full understanding of the dispersion of the pulse requires analyzing the complex amplitude and frequency-dependent phase added by each component, which is beyond the scope of this dissertation. Briefly, an ideal (i.e. transform-limited) pulse of light consists of superimposed waves of different frequency with the same phase (i.e. the phase is constant with respect to frequency).

In this case, the phase velocity and group velocity of the superimposed waves are the same . The FWHM of the spectral width $\Delta\nu$ (i.e. the spectral bandwidth of light that makes up the pulse) of a transform-limited Gaussian pulse is given by

$$\tau\Delta\nu = 0.44 \tag{2.34}$$

where τ is the temporal FWHM of the pulse. This product will be greater for any real pulse. As the pulse propagates through the microscope, it broadens because the index of refraction of the components it travels through vary with frequency, which causes different waves that compose the pulse to travel at different velocities (i.e. the material adds frequency dependent phase to the complex amplitude). Therefore, the phase and group velocity of the pulse are different after traveling through a dispersive medium. When analyzing the pulse properties, it may be useful to express the bandwidth of the pulse in terms of the wavelength of light

$$\Delta\lambda = \frac{\lambda_0^2}{c}\Delta\upsilon \tag{2.35}$$

where λ is the wavelength of light, and λ_0 is the wavelength corresponding to the center frequency [81].

The dispersion compensation prisms were calibrated by measuring the fluorescence signal of fluorescein measured by the microscope as a function of prism distance. When the signal was maximized, the negative dispersion added to the pulse by the DeepSee system compensated the dispersion added by the optical components in the microscope. The position of the prisms remained fixed for all imaging conditions. No measurements of the group velocity dispersion of the system were made.

2.3.2 Lateral and Axial Scanning

To scan in the x and y directions, a 2D mirror galvanometer was used (GVS012, Thorlabs). The control voltages sent to each galvanometer were determined by considering the voltage-to-mechanical angle scale factor (0.5V/mechanical degree), the desired FOV, time per frame, and number of lines per frame. The pixel dwell time was selected so that the pixel size was square. For example, if the frame rate was 1second and there were 500 lines per frame, then the pixel dwell time would be $1/500^2$, which is equal to 4μs. Eq. 2.2 and 2.4 were used to determine the angle at the mirror galvanometer given the desired FOV. The FOV was scanned with a saw-tooth pattern (maximum line rate of 350Hz), and a blanker was added using the EOM.

To scan in the axial direction, the microscope has a motorized lab-jack with 0.8nm resolution and <50μm bidirectional repeatability. Z-stacks were collected by scanning the FOV, moving the stage, and scanning the new axial position. Axial scanning with an electrically tunable lens (ETL) is presented in chapter 3.

2.3.3 Alignment and Opto-Mechanical Design

Several optical components had no commercially available mounts. Therefore, custom mounts were designed using Autocad (Autodesk) and manufactured at the Washington University School of Medicine machine shop or with a 3D printer (Ultimaker 2 Extended +, Ultimaker). Components that were custom designed included a dichroic mirror cube, lens mount for the scan lens, galvanometer mount, and objective mount adapter. Alignment of optical components was achieved using optical rail systems and micro-manipulators.

2.3.4 Software

Control signals for the galvanometers, EOM, and stage were generated using Matlab. The custom-written software enables the user to select the FOV dimensions, pixel dimensions, pixel dwell

time, scan origin for scanning off axis, and time per frame. Using callback functions, the output of the PMT was reshaped to display images in real-time so that the user can adjust the position of the sample or gain of the PMT amplifier. Because the microscope is capable of scanning such a large FOV with <1.7μm resolution, the software was also written so that the microscope could image subframes within the FOV with high resolution. Multiple subframes are then displayed in real-time. All images can be streamed to disc for image processing and analysis after the experiment. Z-stacks can also be acquired by serial communication with the motorized lab jack. A 1ms delay is added between frames during the stage's movement.

2.4 Experimental Results

2.4.1 Experimental Validation with Fluorescein and Fluorescent Microspheres

We tested the performance of our system experimentally by placing fluorescein at the sample plane and measuring the fluorescent signal over the FOV with the Olympus XLFluor4X underfilled to either NA 0.22 or NA 0.11 (Fig. 2.14(b)-(c)). For reference, we also measured the fluorescent signal using a 20X objective with the same relay system (Fig. 2.14(a)). Fluorescent signal remained above 0.4 times the maximum fluorescence signal over FOV diameters of 1.4mm, 7mm, and 9mm with the Olympus XLUMPLFLN (20X, NA 1.0), Olympus XLFluor4X underfilled to NA 0.22, and XLFluor4X underfilled to NA 0.11, respectively.

The resolution was measured over the FOV by imaging 0.5μm fluorescent microspheres (18859-1, Polysciences, Warrington, USA; Fig. 2.14(d)-(h)) and calculating the FWHM of the PSF. As expected, underfilling the back aperture enables larger field imaging, but worsens the resolution, especially axially in comparison to the Olympus XLUMPLFLN (Fig. 2.14(d)-(h)). However, our optimal design (XLFluor4X underfilled to NA 0.22) can achieve a SBP of 35MP, which is 3.2 times more than what can be achieved with a two-photon microscope using conventional objective

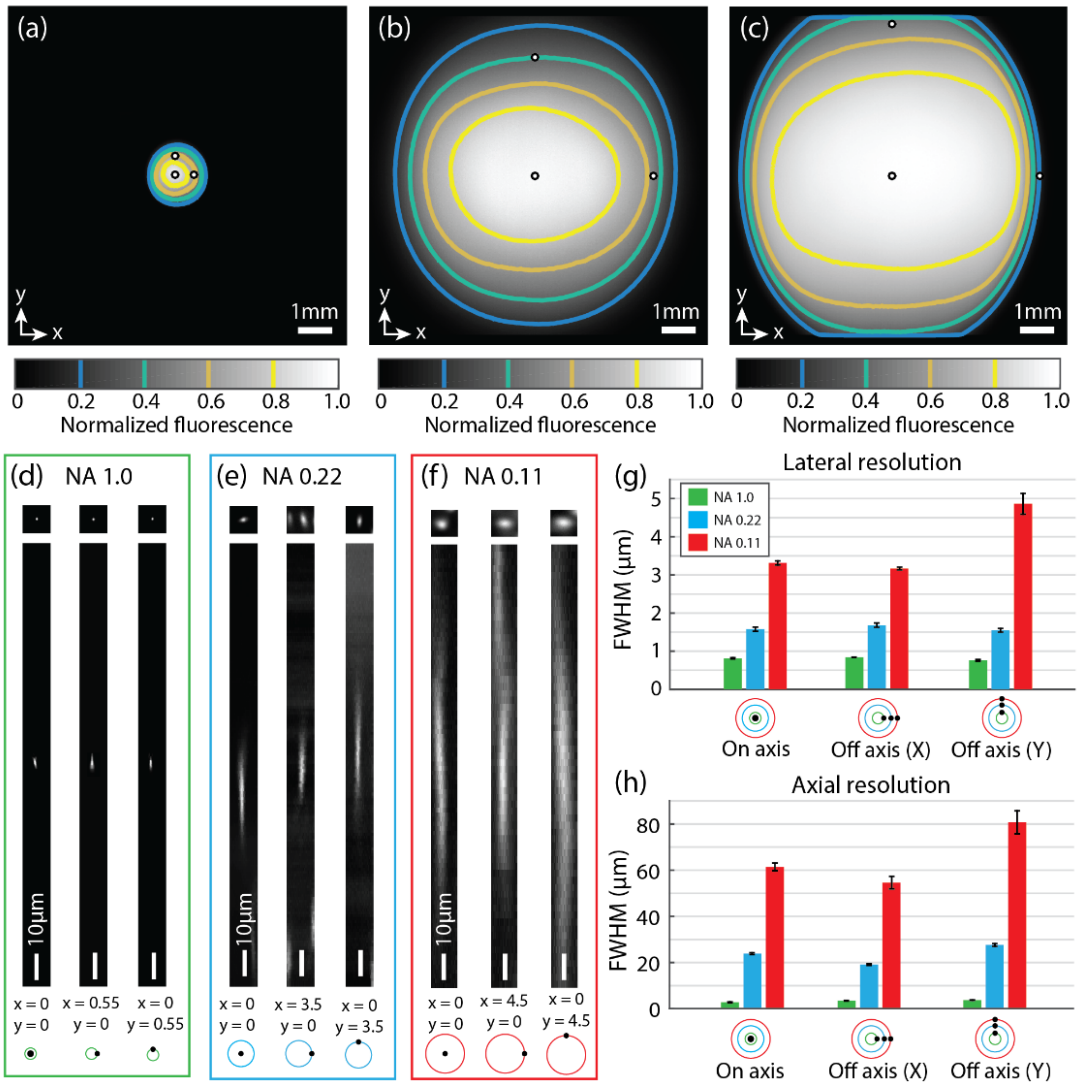

Fig. 2.14 Experimental FOV and resolution measurements. (a) Normalized fluorescence signal measured across the FOV using the high throughput relay shown in Fig. 2.12 and the Olympus XLUMPLFLN (20X, NA 1.0). (b) Same as (a), but for Olympus XLFluor4X with back aperture underfilled to an effective NA of 0.22 (10mm input beam diameter). (c) Same as (a)-(b), but for Olympus XLFluor4X with back aperture underfilled to an effective NA of 0.11 (5mm input beam diameter). (d) Lateral and axial cross section of PSF measured experimentally by imaging 0.5μm diameter fluorescent beads embedded in agarose. Results are for high throughput relay and NA 1.0 (Olympus XLUMPLFLN). Beads were imaged both on and off axis as specified underneath cross sections (e) Same as (d), but with the Olympus XLFluor4X and effective NA of 0.22. (f) Same as (d)-(e), but with back aperture underfilled to an effective NA of 0.11. (g) Estimation of lateral resolution measured as FWHM of PSF shown in (d)-(f). (h) Same as (g), but for axial resolution.

and scan optics. The lateral and axial resolution of the LF-TPM system over the 7mm diameter FOV is <1.7μm and <28μm, respectively. This demonstrates the performance and range of imaging fields achievable with these scan optics and objective.

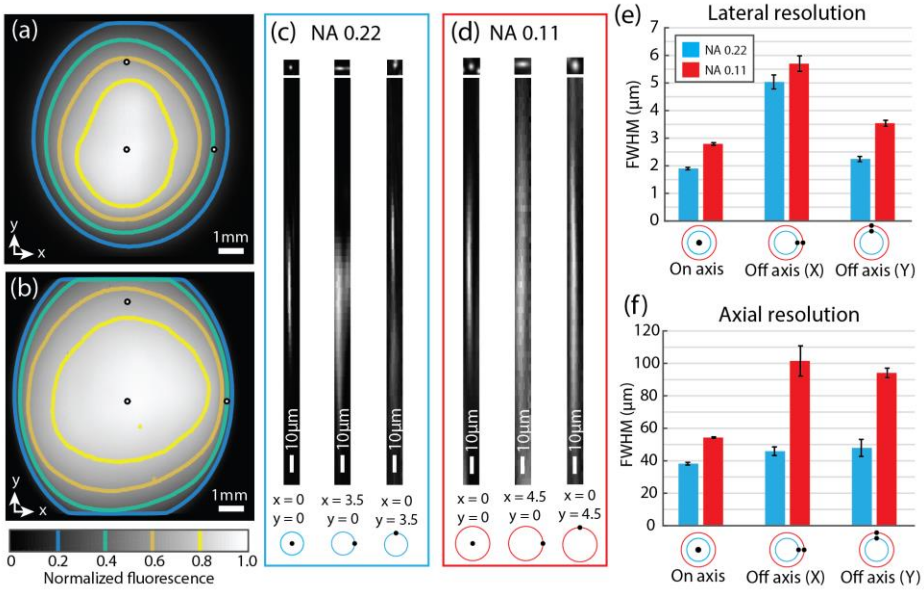

Fig. 2.15. Experimental FOV and resolution measurements for MVPLAPO 2XC. (a) Normalized fluorescence measured with high throughput relay shown in Fig. 2.13 and the MVPLAPO 2XC with back aperture underfilled to an effective NA of 0.22. Result is for 10mm input beam diameter. (b) Same as (a), but for MVPLAPO 2XC with back aperture underfilled to an effective NA of 0.11. (c) Lateral and axial cross section of PSF measured experimentally by imaging 0.5μm diameter fluorescent beads embedded in agarose. Results are for high throughput relay and MVPLAPO 2XC with back aperture underfilled to an effective NA of 0.22. Beads were imaged both on and off axis as specified underneath cross sections (d) Same as (c), but with and MVPLAPO 2XC with back aperture underfilled to an effective NA of 0.11. (e) Estimation of lateral resolution measured as FWHM of PSF shown in (c)-(d). (f) Same as (e), but for axial resolution.

At the preliminary stages of our design, we identified two high throughput objective lenses: XLFluor 4x and MVPLAPO 2XC. Our best imaging results were achieved with the XLFluor 4x, and therefore this objective was presented in the results of the manuscript. The MVPLAPO 2XC is designed for wide-field illumination in a macro zoom microscope (MVX10, Olympus, Tokyo, Japan), and there have been no reports of its use in a laser scanning microscope. Nonetheless, we

analyzed the performance of this objective experimentally using fluorescent microspheres (18859-1, Polysciences, Warrington, USA). The resolution measured with this lens was considerable worse off axis in comparison to the XLFluor 4x, and was therefore not used for LF-TPM (Fig. 2.15).

2.4.2 In-vivo Applications of LF-TPM

For an exemplary application of the system, we performed *in vivo* imaging of the mouse cerebral vasculature and microglia (Fig. 2.16). All animal studies were approved by the Washington University School of Medicine Animal Studies Committee (protocol #20160217) under guidelines and regulations consistent with the Guide for the Care and Use of Laboratory Animals, Public Health Service Policy on Humane Care and Use of Laboratory Animals, the Animal Welfare Act and Animal Welfare Regulations, and ARRRIVE guidelines. To image the cerebral micro-architecture, we removed an approximately 9mm diameter portion of the mouse skull. Mice were anesthetized with 4.0% isoflurane inhalation in oxygen for induction and 1.5-2.0% for surgery. The fur around incision site was removed with hair removal lotion, and the mouse was placed in a stereotaxic frame to secure the head before surgery. To prevent swelling of the brain, Dexamethasone (2mg/kg) and Mannitol (20% in 0.9% saline; 200µl) were administered subcutaneously prior to surgery. Lidocaine was then applied to the surgical region. The skin on the top of the skull was lifted with forceps, cut using sterile scissors, and removed to expose the skull for the craniotomy. Using a dental drill, an approximately 9mm diameter circle was gently drilled approximately 1mm posterior to Bregma. Drilling was continued until only a thin layer of bone remained. Using thin tip forceps, the skull was removed after applying a drop of saline to the surgery site. Mice were then imaged with the LF-TPM system under 1.5% isoflurane inhalation [54, 82].

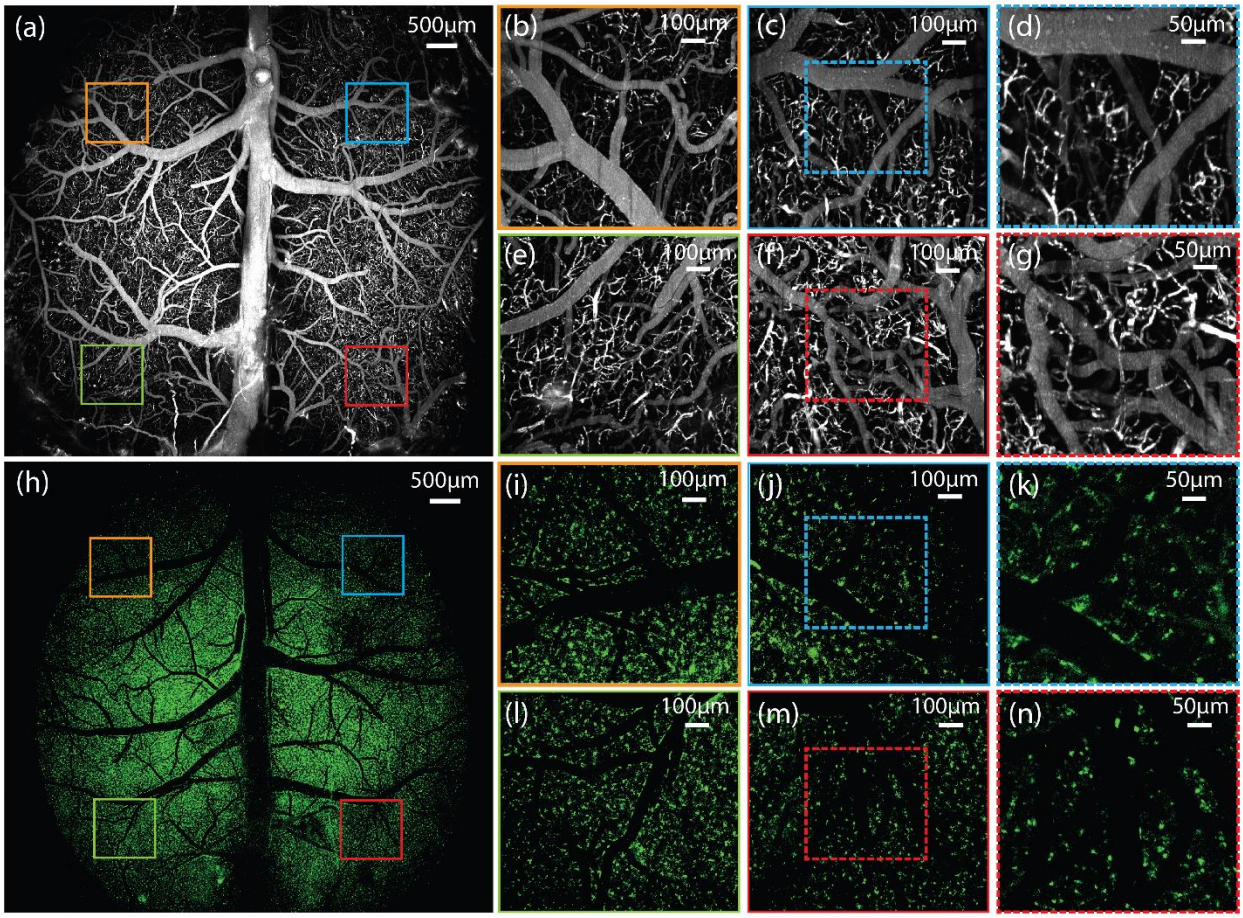

Fig. 2.16 Cerebral vasculature and microglia imaged over the mouse cortex with LF-TPM. (a) Maximum projection image of cerebral vessels imaged with LF-TPM after tail vein injection of fluorescein-dextran. Dimensions of box are 8 x 8mm^2. (b) 1x 1mm^2 FOV imaged 3mm off axis at orange box shown in (a). (c) 1 x 1mm^2 FOV imaged 3mm off axis at blue box in (a). (d) 500 x 500µm^2 FOV highlighted by dashed blue box in (c). (e) 1 x 1mm^2 FOV imaged 3mm off axis at green box shown in (a). (f) 1x 1mm^2 FOV imaged 3mm off axis at red box shown in (a). (g) 500 x 500µm^2 FOV highlighted by dashed red box in (f). (h)-(n) Same as (a)-(g), but for microglia imaged in Cx3Cr1$^{GFP+/-}$ mice.

We then imaged the cerebral vasculature in male C57BL6 mice after tail vein injection of fluorescein-dextran and the microglia in mice with GFP knocked-in to the Cx3Cr1 locus (Cx3Cr1$^{GFP+/-}$). To maximize the information transmitted by our system, we imaged the mouse cortex under optimal system conditions (i.e. XLFluor4X underfilled to NA 0.22, SBP approximately 35MP). Due to the curvature of the mouse brain, full field imaging required axial

scanning using a motorized stage (MLJ050, Thorlabs). To demonstrate the capabilities of our system, we scanned both a low resolution scan of the full FOV (Fig. 2.16(a) and 2.16(h); 8 x 8mm^2, 1000 x 1000 pixels), and high resolution scan of smaller fields 3mm off axis (Fig. 2.16(b)-(e) and 2.16(i)-(l); 1 x 1mm^2, 1000 x 1000 pixels). Also included are images with similar FOV to conventional TPM (Fig. 2.16(f)-(g) and 2.16(m)-(n); 500 x 500μm^2, 500 x 500 pixels). For all imaging, the mouse remained in the same lateral (x,y) position relative to the objective. We also calculated the FWHM of capillary vessel diameters to determine resolution capabilities of our system for *in vivo* applications. The system was able to image vessel diameters as small as 3μm over the entire FOV, as well as approximately 22,500 microglia with cell body diameter of approximately 5μm over the cortex of Cx3Cr1$^{GFP+/-}$ mice.

2.5 Discussion

Both conventional TPM and MOI-WFI have improved our understanding of the functional architecture of the mouse cortex. However, both of these imaging modalities are limited by the trade-off between resolution and FOV. In this report, we have demonstrated the potential that LF-TPM has in studying the mouse brain over multiple spatial scales. Our results demonstrate almost a 100-fold increase in FOV area and 3.2-fold increase in information transmission in comparison to conventional TPM, all while maintaining <1.7μm and <28μm lateral and axial resolution, respectively (Table 2.4). Here we highlighted *in vivo* imaging of the cerebral vasculature and microglia cell bodies over a 7mm diameter FOV. In addition to improving our understanding of the cellular and vascular mechanisms underpinning resting-state functional brain connectivity, LF-TPM may also improve our understanding of the cellular dynamics of other neural phenomena that occur over large regions of the mouse cortex such as cortical spreading depression [30, 83, 84], retinal waves [31], and Mayer waves [32, 85]. Imaging individual microglia cells over such a large

portion of the cerebral vasculature also has the potential for fundamental discoveries in the inflammatory responses that occur in stroke, multiple sclerosis, and neurodegenerative diseases [59, 75, 86].

In comparison to other groups that have extended the FOV in TPM by custom designing each component, our design depends on a simple optical invariant framework, first to evaluate potential optics and secondly to design scan relays suitable for large FOV imaging [49, 65]. This approach permits the microscope designer to isolate components and compare the performance of single components to the throughput demands of the objective lens free from the complexities of a fully integrated microscope design. As a result, it can be easily adapted to increase the FOV in any other custom-built laser-scanning microscope, making it ideal for groups searching for cost-effective large FOV microscopes constructed with off-the-shelf components.

Table 2.4 Imaging capabilities of isolated objectives, conventional TPM, and LF-TPM. Lateral resolution for comventional TPM with pixel averaging is effection resolution, not optical resolution. For LF-TPM, the theoretical and experimental lateral resolution are included.

Objective or system	**NA**	**Lateral Resolution (µm)**	**FOV diameter (Ømm)**	**Rectangular FOV (mm x mm)**	**Pixels for rectangular FOV**	**FOV area (mm^2)**	**SBP (MP)**
Olympus XLFluor 4X	0.28	1.08	6.63	4.69 x 4.69	8709 x 8709	21.98	75.85
Olympus XLUMPLFLN 20X	1	0.31	1.10	0.78 x 0.78	5081 x 5081	0.61	25.82
Conventional TPM	1	0.31	0.71	0.50 x 0.50	3280 x 3280	0.25	10.76
Conventional TPM (pixel averaging)	1	1.96	0.71	0.50 x 0.50	512 x 512	0.25	0.26
LF-TPM system	0.22	1.37/1.68	7.00	4.95 x 4.95	5893 x 5893	24.50	34.72

One of the limitations of analyzing the optical invariant function of isolated components is that it may not account for additive aberrations introduced when integrating multiple optical components. Therefore, it may be necessary to identify several potential scanning lens candidates and test multiple combinations of optical relays. Other LF-TPM designs consist of custom-designed optics that may have lower throughput in isolation, but compensate for aberrations introduced by other optics in the system, such as the remote focusing objective designed by Sofroniew *et al* and the scan compensation lenses implemented by Tsai *et al* [65, 66]. In cases such as these, the design strategy in this report can be applied, but it requires analyzing subsystems with counteracting aberrations together. There may also be other optimization parameters in addition to throughput, such as propagation time delay difference, that could improve the SNR of the system, which were overlooked in the analysis described here [65].

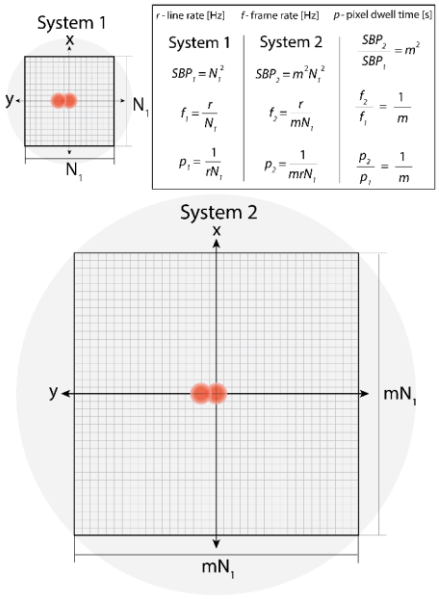

Fig. 2.17 Differences in frame rate and pixel rate for systems with different SBP. System 1 resolution and FOV require N_1 lines to sufficiently sample FOV. System 2 resolution and FOV require a factor of m more lines to be scanned. The resulting frame rate f of the systems that results from imaging the full SBP is equal to the line rate r divided by the number of scanned lines. Despite increased SBP, system 2 frame rate decreases by a factor of m. The pixel dwell time p for system 2 also decreases by a factor of m in comparison to system 1.

Despite these limitations in this design approach, the primary drawback is the lack of commercially available scanning optics that match the demands of high throughput objectives, as testament to our difficulty in identifying a high throughput, long focal length tube lens.

Separate from the optical invariant design approach, our current system has two potential shortcomings: imaging speed and an anisotropic PSF in the axial and lateral dimensions. Due to the raster scanning necessary to acquire images, a major challenge in applying LF-TPM to functional brain imaging is imaging speed and SNR. Consider an imaging system that requires N x N pixels to sufficiently sample the FOV given the SBP of the system (Fig. 2.17). If a LF-TPM system requires m more lines to scan and the line rate r is the same in both systems, then the frame rate and pixel dwell time p will decrease by a factor or m.

Fortunately, traditional mirror galvanometers have the advantage of flexible scanning patterns that enable imaging multiple sub-regions or unique scan geometries within the FOV [14, 87]. Another option for increasing the frame rate and SNR is to simply scan the entire FOV with fewer lines. This is already commonly done in conventional TPM systems, which typically undersample images by a factor of around 3-5 to collect 512 x 512 pixel images with frame rates of 1Hz with traditional galvanometers or 30Hz using resonant scanners [13, 24, 88]. The effective lateral resolution in such an imaging paradigm is around 2μm, which is actually greater than the capabilities of our system (Table 2.4). If the SNR of the system is sufficient, the limiting factor to the imaging speed of our LF-TPM system is the scan rate of the mirror galvanometer. We opted to reduce the complexity of our system by using a single relay, and thus are limited to imaging at approximately 100 lines/sec. Multi-focal TPM or other PSF engineering techniques may also serve to improve the image acquisition rate in LF-TPM [63, 64, 89].

The anisotropic PSF of our system is a result of our decision to maximize SBP and FOV by underfilling a low NA objective. Although functional measurements of individual cells may be confounded by a PSF that stretches beyond subcellular resolution in the axial direction, an ellipsoidal shaped PSF may also be advantageous depending on the imaging conditions. Indeed, the Bessel beam has been utilized for live sample imaging of neurons to extend the depth of field and increase volumetric imaging rates [90, 91]. Furthermore, lower excitation NA can potential enable deeper imaging in tissue due to the index mismatch between the immersion fluid and the tissue [92]. Because the collection NA remains the same even when the objective is underfilled, the collection efficiency of the microscope does not decrease. Although the collection efficiency is predicted to be proportional to the collection NA squared for non-scattering media using a paraxial model, the collection efficiency actually depends on the throughput of the objective for scattering samples. Singh et al. also recently showed that the dependence of the collection efficiency is less dependent on the NA than predicted with paraxial model when modeling epi-fluorescence collection with diffraction limited lenses [53, 68, 92].

Regardless of the challenges discussed here, LF-TPM holds great promise for *in vivo* imaging of the mouse cortex. Here we have presented an intuitive design approach for developing LF-TPM with off-the-shelf components. As highlighted by our modeling and experimental results, analysis of the optical invariant can lead to lower cost LF-TPM designs, as well as minimize the need for complex optical design using optical engineering software.

Chapter 3: Adaptive Field Two-Photon Microscopy

3.1 Introduction

Conventional optical sectioning microscopy is generally limited to imaging a FOV <1mm [65]. When these microscopes are used to image mice *in vivo*, the specimen plane of the microscope intersects a single layer of the cortex by tilting the mouse head or the microscope so that the optical axis of the microscope is perpendicular to the cranial window [93, 94]. However, due to the large FOV capabilities of the system we presented in Chapter 2, the curvature of the mouse brain prevents imaging of the full FOV in a single frame and instead only an elliptic region of the brain is imaged by the microscope (Fig. 3.1) [49]. Therefore, full field imaging of the surface of the brain for LF-TPM requires scanning in the axial direction [6, 65]. Consider the *in vivo* data collected in Section 2.4.2 from a mouse with tail vein injection of fluorescein (Fig. 3.2(a)). To visualize the cerebral vasculature over the volume, a maximum projection image can be synthesized from the z-stack by taking the maximum value at each pixel over the entire volume and plotting it in a single image (Fig. 3.2(b)) [95, 96]. A surface profile of the mouse brain can

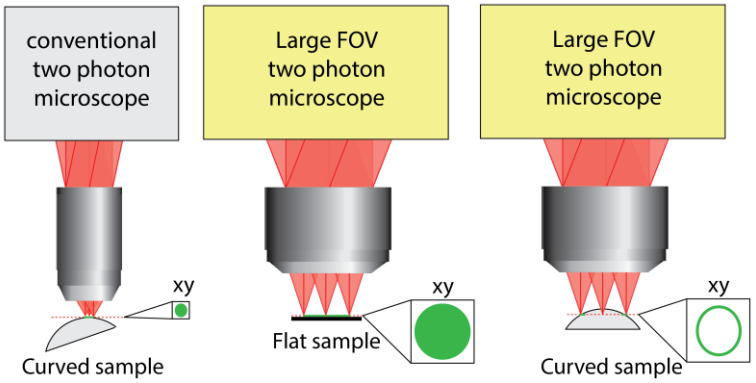

Fig. 3.1. Curvature of mouse brain prevents full frame imaging in LF-TPM. Full field in vivo imaging can be achieved with conventional TPM by tilting the mouse or microscope. However, the full FOV can not be imaged in curved samples with LF-TPM.

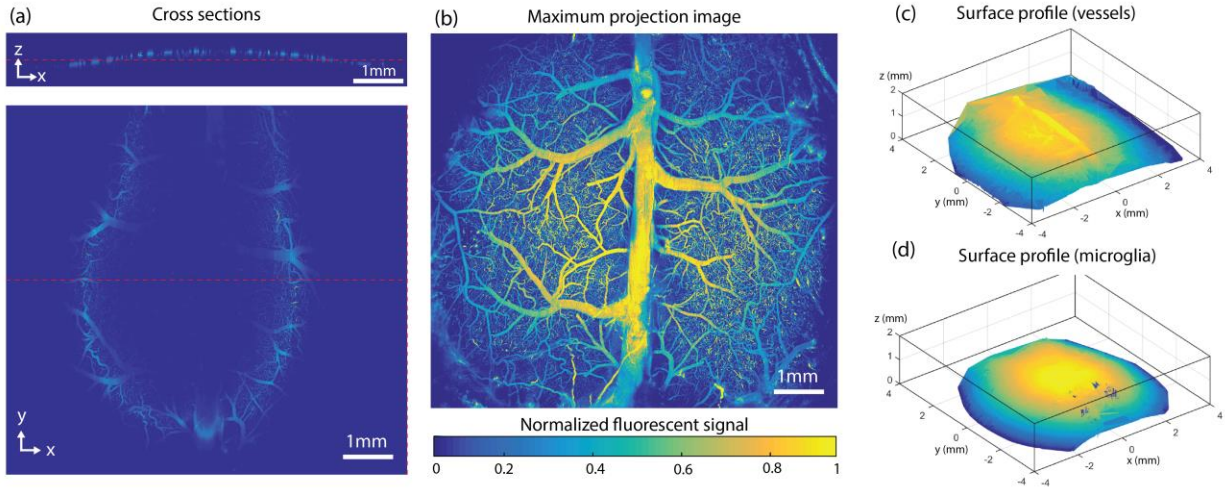

Fig. 3.2. Volumetric imaging and surface profiling of the mouse brain with LF-TPM. (a) Axial and lateral cross sections imaged with LF-TPM. The red dashed line in the axial cross section shows the position of the axial cross section in the lateral slice and vise versa. (b) Maximum projection image of the mouse cerebral vasculature. (c) Surface profile acquired by plotting axial position of maximum value as a function of xy position for mouse with tail vein injection of fluorescein. Data is from (a)-(c). (d) Same as (c), but for $Cx3Cr1^{GFP+/-}$ mice.

also be generated by plotting the axial position of the maximum value at each pixel (Fig. 3.2(c)-(d)). However, the long acquisition times for scanning a volume prevent LF-TPM utility for many *in vivo* applications, such as functional imaging of calcium dynamics [13, 87] and fast changes to vascular or neural dynamics after drug administration to the animal, such as induced vasomotion after injection of N^G-nitro-L-arginine [97]. For example, the surface of the mouse brain extends over 1-1.5mm in the axial direction over the system's 7mm diameter FOV. Because the axial resolution of the microscope is <28μm, imaging of the surface of the brain requires around 70-100 frames, thus increasing the full-frame rate by a factor of 70-100. Many of the pixels in a single image of the z-stack contain no information about the sample, and thus precious scanning time is wasted as the microscope scans these dark regions [90, 98, 99]. To overcome the challenge of imaging large FOV with fine axial resolution, we present adaptive large FOV TPM (ALF-TPM). The technique enables imaging a single field with arbitrary curvature by using an electrically

tunable lens (ETL), and has the potential for improving imaging speed by a factor of 100 for LF-TPM.

Before presenting the technique, we review several ways that conventional TPM systems acquire images from different axial positions in a sample. An elementary approach to image a different cross section in a sample is to move the sample in the axial direction with a manual or motorized stage [96]. However, motorized stages required for moving a small animal will usually have slow response times in comparison to other techniques. Another method is to move the objective while the sample remains fixed [6]. The objective lens is mounted to a fast piezo-electric positioner (e.g. 10Hz for amplitudes of 200-300μm), and the objective focal planes is continuously swept through the volume in synchronized with the scanning of the beam [100]. Using a piezo-electric positioner and unique x-y scanning modes, Göbel et al. were able to image calcium activity of approximately 200 cells at 10Hz over a 250 x 250 x 250μm^3 volume [101].

Instead of moving the objective and sample, axial scanning can also be achieved by changing the divergence of light at the back aperture with acousto-optic deflectors (AODs), spatial light modulators, or ETLs [6]. These optical components introduce positive or negative curvature in the wavefront, which alters the position at which light is focused in the sample. Because objectives are designed to accept planar wave fronts at the back aperture, these approaches to axial scanning introduce optical aberrations that degrade the resolution of the microscope. However, because AODs and ETLs require no movement, they are faster than piezo-electric positioners and stages (e.g. acouto-optic lenses can reach 400kHz axial scan rates over a range of 100μm [102]). Both AODs and ETLs have been coupled with a TPM system for imaging calcium dynamics in the mouse cortex. ETLs can be positioned directly at the back of the objective lens, at a conjugate aperture plane, or before the scanning engine of the microscope. If the ETL does not coincide with

the back focal plane of the objective lens when positioned at the back of the objective, then changes in the axial focus due to the ETL will result in magnification changes of the microscope [103, 104]. Another way to adjust the wavefront at the back aperture is to use Bessel beams, which extends the PSF in the axial direction [90, 91]. This enables fast volumetric imaging, but may aggregate signals from cells that are located in the same lateral position within the volume [65, 70].

Remote focusing enables faster axial scanning than piezo-electric positioners without introducing spherical aberrations to the system [6]. A perfect 3D imaging system can only be achieved when the magnification of the system is equal to the ratio of the refractive indices at the object and image plane [105]. This is clearly not satisfied in optical microscopes so instead only the sine condition is satisfied which imposes an aberration-free transformation between points that lie only in a single plane. Remote focusing works by conjugating a mirror to the object plane with a perfect optical system (i.e. total magnification is equal to the ratio of the indices of refraction). A beam splitter and tube lens are then used to magnify the image by the ratio of the focal length of the tube lens and objective. The axial position imaged can then be changed by moving the mirror, thus enabling axial scan rates in the range of kHz [65, 106].

Although all of these axial focusing techniques have been applied to fast volumetric imaging of the mouse brain, they have not been applied to imaging an arbitrary surface within a single frame. Therefore, we introduced an ETL to a large FOV TPM system and calibrated the ETL to scan an arbitrary surface. Our approach has the potential to reduce volumetric imaging rate by a factor of 100, while scanning over an entire layer of the mouse cortex.

3.2 Axial Focusing with Electrically Tunable Lens

3.2.1 System Overview

ALF-TPM includes an ETL before the scanner of the microscope (Fig. 3.3(a)). All other components are the same as described in section 2.3. The ETL (EL-10-30-C-NIR-LD-MV, Optotune, Dietikon, Switzerland) has a focal length tuning range of -667 to +286 mm, corresponding to a control current of 0-250mA, and an offset lens with focal length equal to -150mm. A change in the focal length in the lens results in a change in the divergence of the beam at the back aperture (Fig. 3.3(b)), thus enabling fast axial scanning. The tuning range of the ETL enables an axial scanning range of approximately 1.5mm (see Section 3.2.2) with a <2.5ms step response, which is close to matching the maximum line rate of the galvanometer. This step response time is probably conservative in comparison to the rate at which the ETL can be driven with a sinusoidal or sawtooth control signal, although the manufacturer does not provide these specifications.

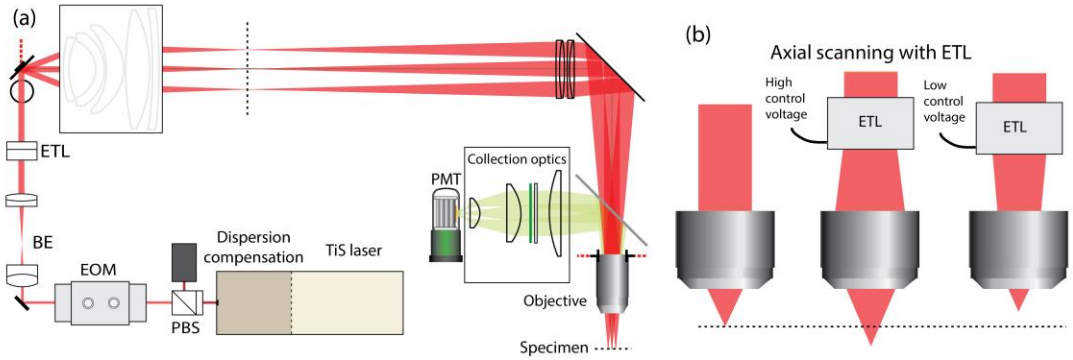

Fig. 3.3. ALF-TPM schematic. (a) System layout. ETL is positioned before scanner to prevent changes in system magnification when imaging at different axial positions. (b) Axial scanning with ETL.

3.2.2 Calibration

To calibrate the ETL with respect to axial position at the sample, we positioned a 16μm thick slide at the object plane of the microscope (F24630, Thermofisher, St Peters, Missouri) on a motorized

stage (MLJ050, Thorlabs). The motorized stage was then incremented by 100μm. For each stage position, the ETL was swept through a range of control voltages to determine the control voltage at which the mean image intensity was maximized (Fig. 3.4(a)-(b)). This ETL control voltage adjusts the divergence of the beam at the back aperture such that the axially shifted sample coincides with the focal plane of the system. The procedure was repeated to create a calibration curve of the ETL voltage with respect to position for an axial range of 1.1mm (Fig. 3.4(c)). The mean signal acquired when imaging a cuvette of fluorescein was then plotted for each axial position scanned by the ETL. Decreases in average power caused by different operating conditions of the ETL result in decreased fluorescence signal of the system (Fig. 3.4(d)). The control signal of the EOM was adjusted for each axial position to compensate for decreases in signal caused by the ETL.

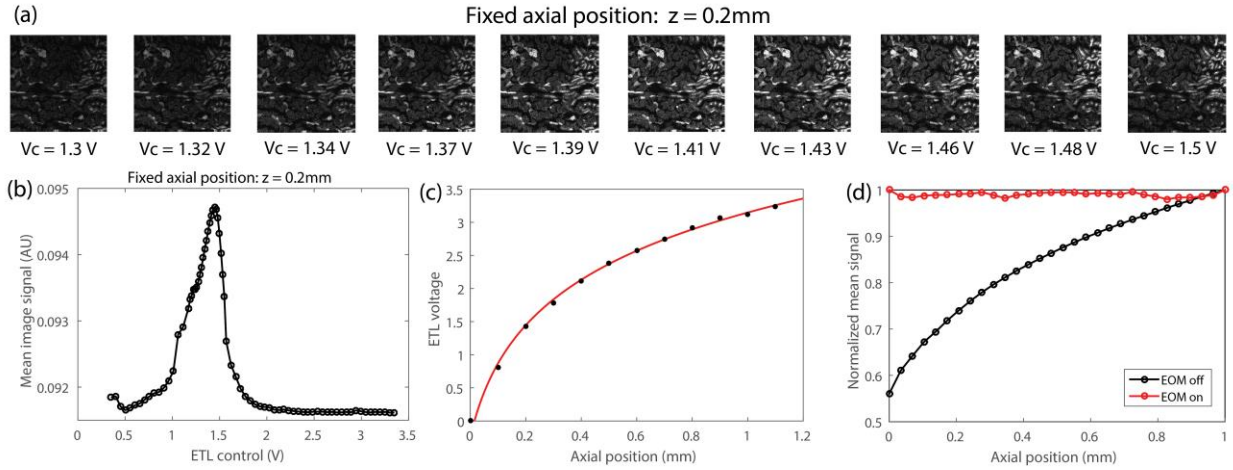

Fig. 3.4. ETL and EOM calibration. (a) Images acquired with ALF-TPM for thin specimen positioned at axial position 0.2mm above focal plane of microscope without ETL. (b) Mean image signal plotted as a function of ETL control voltage. At maximum, the ETL is adjusting divergence at back aperture such that the light is focused onto sample. (c) Calibration curve for ETL. ETL control voltage is plotted as a function of axial position. Best log fit is plotted as red curve. (d) Normalized mean signal as a function of axial position. Power losses due to ETL changes can be compensated by adjusting the control signal of the EOM.

3.2.3 Axial Scanning of Arbitrary Surface

To scan arbitrary surfaces, a maximum projection image is acquired by scanning a volume with the ETL (Fig. 3.5(a)-(c)) From this data, an ETL calibration voltage image (CVI) can obtained by plotting the ETL voltage corresponding to the maximum signal acquired at each pixel as a function of position (Fig. 3.5(d)). The CVI is then smoothed by a Gaussian filter with 400µm standard deviation to removed heterogeneities. As the beam is scanned across the surface, the focal plane of the system can be adjusted with the ETL based on the control voltage determined by the CVI (Fig. 3.5(e)). As opposed to other ETL microscopy applications, this approach enables imaging of an arbitrary surface so that no time is wasted scanning dark regions of the sample. Representative control signals for the x-galvanometer, y-galvanometer, and ETL for a single frame are shown in Fig. 3.5(f).

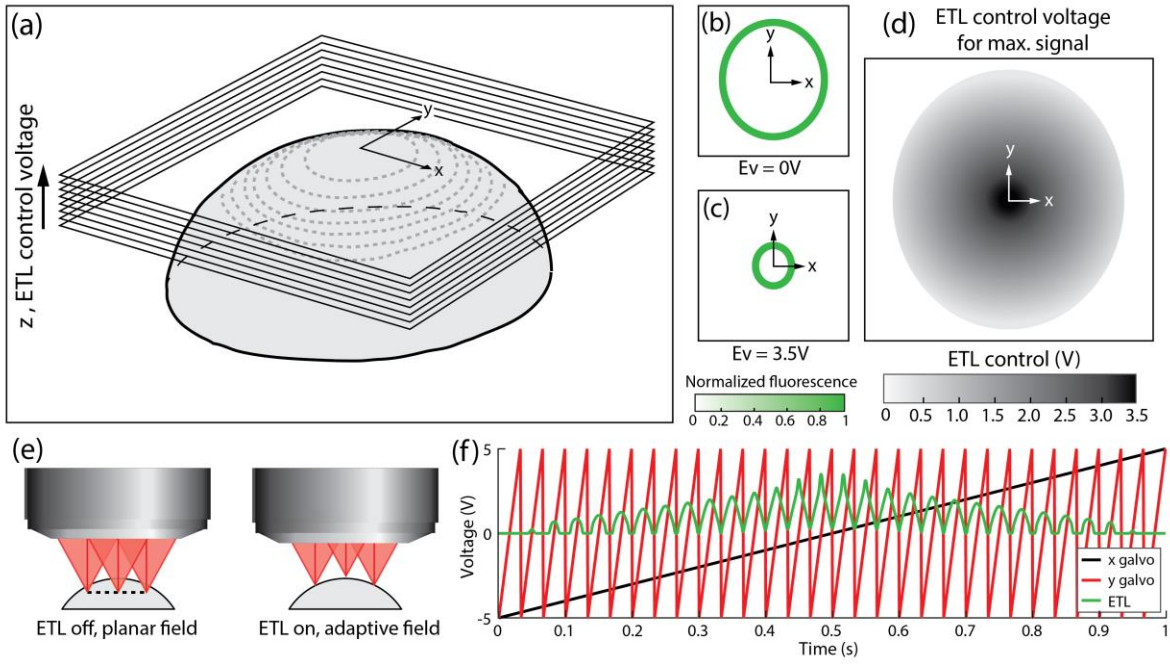

Fig. 3.5. Adaptive field imaging concept. (a) Diagram showing ETL z-stack acquistion. (b) Cross section of curved sample with ETL control voltage equal to 0V. (c) Same as (b), but for different control voltage. (c) Calibration voltage image. Control voltage required for adjust axial focus over curved sample. (e) Planar field imaging and adaptive field imaging with ETL. (f) Representative control signals for galvanometers and ETL.

3.3 Experimental Results

3.3.1 Fluorescent Phantom Development

We tested ALF-TPM by imaging a curved cylindrical fluorescent phantom. The phantoms were designed to match the curvature of the mouse brain: an axial range of 1mm over 7mm diameter FOV. A 100uM fluorescein 1% agarose gel was poured into a petri dish. After the gel hardened, it was left at room temperature to dry out so that it formed an elastic fluorescent sheet with thickness of approximately 40μm. The dried gel was then wrapped around a 1/2" diameter optical post for imaging with the ALF-TPM system (Fig. 3.6(a)). The depth over which the phantom extends *d* was calculated using

$$d = r - \sqrt{r^2 - F^2} \tag{3.1}$$

where r is the radius of the optical post (6.3mm) and F was the half FOV (3.5mm), resulting in an axial range of 1.1mm, which matches the axial range over which the mouse brain must be imaged to acquire full-field images with our LF-TPM system.

3.3.2 Cylindrical Fluorescent Phantom

A z-stack of the cylindrical phantom was acquired using the calibration data from section 3.2.2 (Fig. 3.6(b)). The laser power at the sample was <10mW. A total of 60 images were acquired at a rate of 15s per image. After acquiring the z-stack, a maximum projection image and axial cross section were generated to visualize the curved sheet (Fig. 3.6(c)-(d)). The CVI was generated for determining the control voltage required for imaging the curved surface of the phantom (Fig. 3.6(e)). Smoothing of the image generates sinusoidal control signals that should improve the performance of the ETL in comparison to large bandwidth control signals (Fig. 3.6(f)).

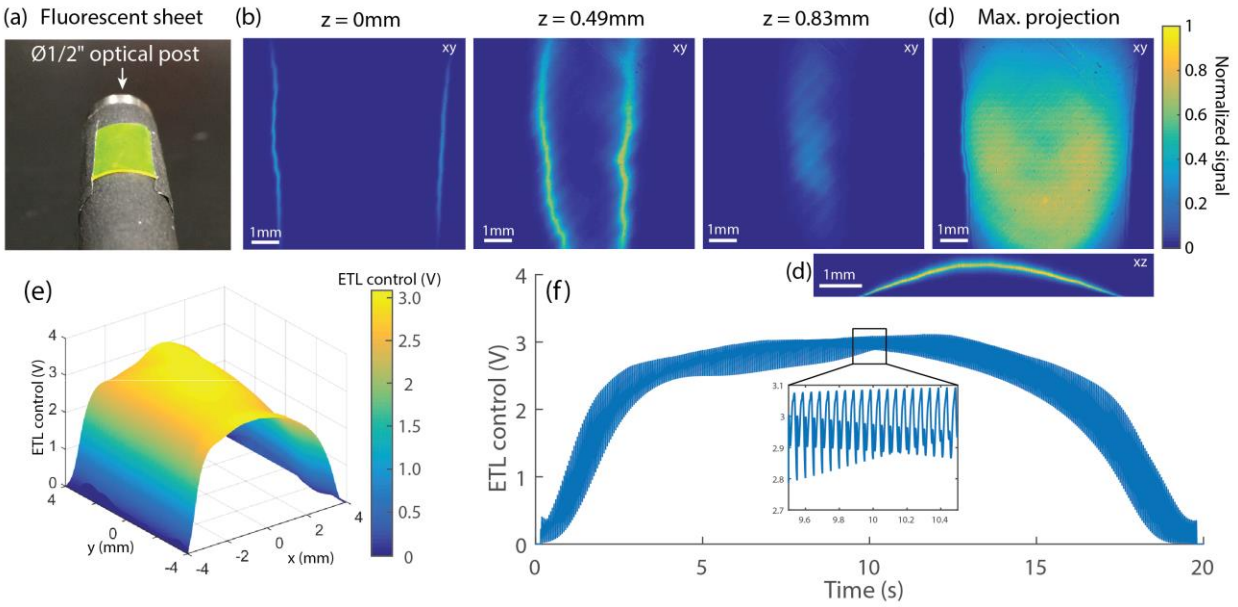

Fig. 3.6. Generating calibration voltage image for curved sample. (a) Dried fluorescent gel bent over ½" diameter optical post. (b) Lateral cross sections of sample. (c) Maximum projection image. (d) Axial cross section. (e) ETL control voltage required for scanning the curvature of the sample. (f) ETL control signal as a function of time.

Using the control signal determined by the CVI, we then imaged the surface of the dried gel within a single image using the ETL and compared it to imaging without the ETL (Fig. 3.7 (a)-(b)). The acquisition time for imaging the curved field was 60 times less than the time required to acquire the z-stack. To quantify the error of the adaptive field image, we created a curved field image stack by moving the stage while the ETL generated a curved field. The axial position for which the signal was maximum at each pixel was compared to the axial position that the initial curved field was acquired. This axial position difference was then plotted as a function of space over the sample (Fig. 3.7(c)) to better quantify the axial error in the system.

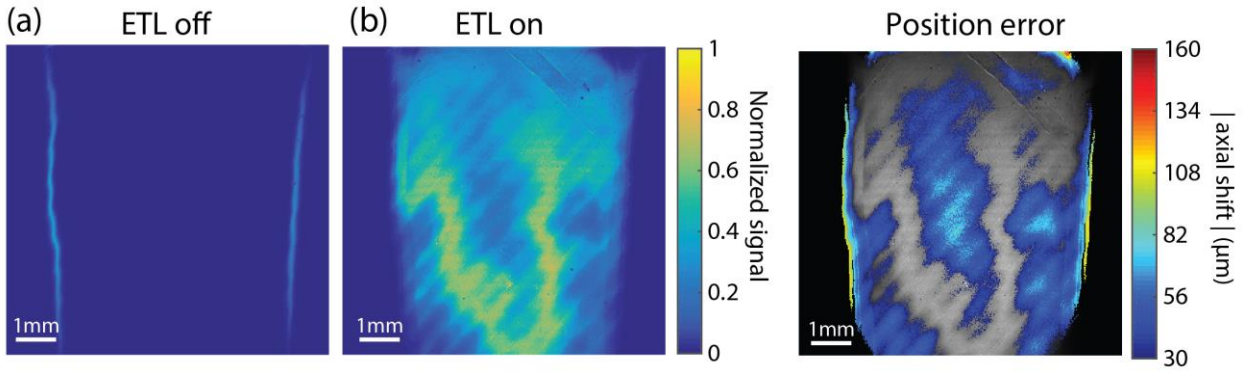

Fig. 3.7. Experimental results of adaptive field imaging with ALF-TPM. (a) Image of fluorescent dried gel acquired with ETL off. Acquisition time is 15s. (b) Image of fluorescent dried gel acquired with ETL on. Acquistion time is 15s. (c) Position error as a function of lateral position. Plotted is the absolute value of the difference between the axial position of the image in (b) and the axial position with maximized signal.

3.4 Discussion

With recent increases in the SBP and depth capabilities of TPM [7, 65, 66], as well as full-skull craniotomy preparations [82], the ellipsoidal shape of the mouse brain becomes a major problem for full FOV imaging. In this chapter, I have presented preliminary results for ALF-TPM using an ETL that has the potential to improve the frame rate of large FOV optical sectioning microscopes.

Our results demonstrate the imaging of a curved sample within a single frame using an ETL with <80μm axial error over the majority of the FOV. This result alone reduces full field imaging time by a factor of around 100 by eliminating scanning of dark regions in the sample. Because the brain is a thick sample, the minor errors measured in using this approach will only result in imaging cortical layers that differ by <80μm, which may not be an issue for many experiments. However, this axial error may be generous because the shape of the mouse brain is ellipsoidal, not cylindrical, so the ETL may require axial scanning along the fast scanning direction. This may be issue, because the response time of the ETL may not be fast enough for axial scanning in this direction. Our preliminary results with ellipsoidal phantoms (data not shown) demonstrate that line rates of

approximately 25Hz can be achieved using this method. These rates may be too slow for measuring biological signals of interest in the mouse brain [14, 29].

An issue we have not yet addressed are optical aberrations and changes in beam diameter at the back aperture introduced by the ETL, which both may worsen the resolution of the microscope [6, 105]. If the magnification of an optical system is not equal to the ratio of the indices of refraction in object and image space, then the Herschel condition must be satisfied for aberration-free imaging of axial positions that do not coincide with the focal plane of the objective [105-106]. The expected degradation of resolution must be analyzed with analytical solutions and optical engineering software. We have begun modeling of ALF-TPM using Zemax, and predict the beam diameter at the back aperture to change by a factor of 0.7 to 1.4. Underfilling of the back aperture by this amount will significantly change the PSF of the system. Furthermore, the objective is not designed for accepting diverging and converging wavefronts at the back aperture, so resolution may be even worse than expected when considering only changes in the beam magnification at the back aperture. To fully quantify the resolution, fluorescent beads must be imaged as described in Section 2.4.1. Remote focusing, which enables prefect axial scanning, may be the ideal solution depending on the results of these future resolution experiments [65].

Neglecting degradation of the PSF, ALF-TPM still only images a single slice in the mouse brain, whereas other axial scanning methods enable fast volumetric imaging [16, 101]. To image cortical volumes, the adaptive field should also be scanned through the volume. This could potentially be achieved using any of the methods described in the introduction, such as piezo-electric positioners and remote focusing. In sparely labeled mice, ALF-TPM with an ETL coupled with Bessel beams, which require lower excitation NA, may be the best solution for fast volumetric imaging of the mouse brain [90-91].

Chapter 4: Imaging large-scale neural phenomena with OISI

In Chapter 2 and Chapter 3, I presented my work in developing multiscale TPM systems. The major limitation of these systems is imaging speed (e.g. 1s/frame to 20s/frame), which is a crucial component of functional brain imaging. To complement the systems with slow imaging speed, I have conducted research on large-scale neural phenomena using OISI, which has a frame rate of 30Hz. Although this system has a significantly lower SBP in comparison to LF-TPM, it's imaging speed and large FOV make it a useful system for studying functional connectivity, Mayer waves, and PIDs.

4.1 Optical Intrinsic Signal Imaging Methods

4.1.1 System Design

The OISI system used in this chapter consists of LEDs operating at four wavelengths (478 nm, 588 nm, 610 nm, and 625 nm) mounted on a metal ring that provide wide-field illumination to the mouse brain. An EMCCD camera (iXon 897, Andor Technologies) was mounted above the ring of LEDs, and anesthetized mice were positioned such that light diffusely reflected from the brain was detected by the camera. The camera acquired 128 x 128 pixel images (4x4 binning on camera) at a frame rate of 120 Hz over a FOV of approximately 1cm x 1cm. Synchronization of the camera and LEDs was achieved using a data acquisition unit (NI PCI-6733, National Instruments) and custom-written software (MATLAB, Mathworks). After temporally multi-plexing the four illumination wavelengths, the system has a full spectral frame rate of 30 Hz.

4.1.2 Digital Imaging and Signal Processing of OISI Data

Diffusely reflected light collected by the camera was converted into ΔHbO_2 and ΔHb_R using the Modified Beer-Lambert law [72, 107]. Images (for each contrast) were then smoothed with a 5 x

5 pixel Gaussian filter with standard deviation of 1.2 pixels (the effective dimensions on the mouse cortex correspond to a 390 x 390 micron box and 100 micron standard deviation). Spectral analysis of hemodynamic signals was conducted using the fast-Fourier transform (FFT) algorithm. Hemodynamic traces were filtered over different frequency bands between 0.01 Hz to 5.12 Hz by applying digital high-pass and low-pass 5^{th} order Butterworth filters.

In order to examine how the frequency content in the spontaneous activity was spatially distributed over the cortex, spectral maps were also created for each mouse. The FFT of each ΔHbO_2 trace over the cortex of a mouse was computed, and the magnitude of the spectrum within a chosen bandwidth was integrated and normalized with respect to bandwidth, similar to the amplitude of low frequency fluctuations (ALFF) algorithm [108].

For data to be used in the analysis, we required the hemodynamic spectrum to be inversely proportional to frequency and/or any peak within the bandwidth in which HONS have been reported (0.1-0.4 Hz) to be distinct (the magnitude at full width half max was less than 80% of the magnitude of the peak). One animal failed to pass these criteria, and was therefore excluded from the analysis.

4.1.3 Animal Preparation

All animal studies were approved by the Washington University School of Medicine Animal Studies Committee (protocol #20130217) under guidelines and regulations consistent with the Guide for the Care and Use of Laboratory Animals, Public Health Service Policy on Humane Care and Use of Laboratory Animals, and the Animal Welfare Act and Animal Welfare Regulations. Briefly, male Swiss Webster mice (*n*=20, 6-10 weeks, 22-32g, Harlan Laboratories, Indianapolis, IN, USA) were anesthetized with a ketamine-xylazine mixture (86.9 mg/kg Ketamine, 13.4 mg/kg Xylazine) [75]. Mice were then mounted on a stereotactic frame, and their body temperature was

maintained at 37ºC via feedback from a rectal probe. Once securely mounted, the majority of the cerebral cortex was exposed by making a midline incision along the top of the head.

4.1.4 Seed-Based Functional Connectivity

RSFC analysis can be conducted using either ΔHbO_2 or ΔHb_R data. If not specified otherwise, data were filtered between 0.01-0.08 Hz, as described previously [26, 75, 109]. All time traces over the mouse cortex were averaged to create a global signal that was regressed from every pixel. Global signal regression was also performed using the first principal component as a global signal estimator [110]. Sixteen seed locations based on a histological atlas were chosen for functional connectivity analysis: right and left frontal, cingulate, motor, somatosensory, retrosplenial, visual and auditory cortices, as well as the olfactory bulb. Pixel time traces within 0.25 mm of a seed locus (about 30 pixels) were averaged to create a seed time trace. The Pearson r correlation coefficient was calculated between each seed's time trace and every other pixel in the brain, creating a functional connectivity map for that seed. Contralateral homotopic functional connectivity values were determined by calculating the correlation coefficient between homologous regions. The locality of high correlations in resting-state brain maps was quantified by calculating the percentage of the RSFC maps that had correlation values greater than or equal to 0.8.

4.1.5 Statistical Analysis for Mayer Waves Study

A total of 76 five-minute blocks were analyzed in this study (20 minutes of data for 19 mice). Contralateral homotopic functional connectivity values calculated for the eight homologous regions (frontal, cingulate, motor, somatosensory, retrosplenial, visual, auditory, and olfactory) were plotted against the intensity of HONS. Simple linear regression was then performed on the

data, and the coefficient of determination (r^2) was calculated to quantify the correlation between the magnitude of HONS and contralateral homotopic functional connectivity values.

The contralateral homotopic functional connectivity values for the 76 five-minute blocks were then separated into three groups based on the magnitude of HONS present in the block. Eight ANOVA tests were conducted to determine if there was a statistical difference in the mean contralateral homotopic functional connectivity values across these three groups for the eight different seed regions. Critical values for accepting or rejecting the null hypothesis were corrected for multiple comparisons using Benjamini and Hochberg's FDR-controlling procedure ($\alpha = 0.05$).

4.2 Cerebral Functional Connectivity and Mayer Waves

4.2.1 Introduction

Neural activity measured in the resting brain is synchronized and can be analyzed to identify functional brain networks in humans [111, 112], monkeys [113], and rodents [26, 114]. These resting-state functional connectivity (RSFC) measures are typically performed by analyzing hemodynamic activity at frequencies less than 0.08 or 0.1 Hz [115]. RSFC has made a significant impact on how functional connections in the brain are interpreted, and its use in functional magnetic resonance imaging (fMRI) is spearheading the effort to map the functional connectome of the human brain [7]. Application of RSFC techniques in mice has also shown great promise in elucidating the functional structure of the mammalian brain, especially in studies that employ powerful genetic manipulations not possible in humans [116]. The general utility of RSFC in mice has been demonstrated by successful differentiation of resting-state brain networks of wild-type mice and mouse models of Alzheimer's disease and stroke [75, 117].

However, in addition to RSFC phenomena, there are numerous studies of two other low frequency hemodynamic oscillations known as vasomotion and Mayer waves that go back several

decades [118-120]. Although RSFC, vasomotion, and Mayer waves fall within a similar frequency range, the relationship between these phenomena (if any) is rarely addressed and studied, particularly in rodents [121, 122]. As RSFC analysis becomes an increasingly popular technique in functional neuroimaging studies in mice and humans, it is essential to determine how vasomotion and/or Mayer waves affect the low-frequency hemodynamic fluctuations used in RSFC calculations.

Vasomotion is defined as an oscillation of vascular tone that is independent of heartbeat, respiration, and neuronal activity. It has been described *in vitro* and throughout the bodies of various species *in vivo*, including the brains of rats [123], awake rabbits [124], cats [125], and humans [126]. Mayer waves, in contrast, are global oscillations in arterial blood pressure (ABP) that correlate with sympathetic neural activity [119] . While both vasomotion and Mayer waves have been reported at similar frequencies (e.g. 0.1-0.4 Hz), by definition, Mayer waves are synchronous in large parts of the body, whereas vasomotion has been mostly investigated in small networks of vessels and is generally considered to be myogenic in origin [119, 120, 127]. It has also been reported that vasomotion can be affected by anesthesia and hypertension, both of which affect large areas of the body, complicating the differentiation of Mayer waves and vasomotion even further [128, 129].

Regardless of the differences in the mechanisms of vasomotion and Mayer waves, both produce distinctive sinusoidal hemodynamic oscillations in the frequency range of 0.1 to 0.4 Hz. Consequently, they can be identified by a peak with narrow spectral width in the frequency spectrum of hemodynamic measurements. In comparison, hemodynamic oscillations used in RSFC analysis are broadband and inversely proportional to frequency (i.e. spectrum has a 1/f

profile). For the purposes of our report, vasomotion and Mayer waves will be more broadly classified as hemodynamic oscillations with narrow spectral width (HONS).

Herein we examine the interaction between HONS and RSFC in a mouse model. Specifically, we analyzed differential changes of oxy- and deoxy-hemoglobin (ΔHbO_2 and ΔHb_R) over the majority of the mouse cortex using a custom-built optical intrinsic signal imaging (OISI) system. Conducting the study using OISI in mice enabled us to image hemodynamics at 30 Hz, providing access to higher frequency bands than typically available in fMRI without aliasing heart and breathing signals. Our results reveal that RSFC patterns analyzed below 0.08 Hz are largely independent of the presence or magnitude of HONS at higher frequencies. After filtering, these slow fluctuations produce resting-state brain maps with high correlations in focal brain regions that have similar topography to correlation maps identified in previous resting-state studies in rodents, as well as functional maps generated by sensory-evoked activation [26, 75, 116, 117]. Finally, we demonstrate how RSFC results can be misinterpreted when hemodynamics are filtered in a frequency band that include frequencies over which sufficiently high HONS exist.

4.2.2 Identification of HONS with OISI

To investigate the interaction between HONS and RSFC, we began by characterizing HONS and developing a method for quantifying their magnitude. In order to determine if HONS were present in each mouse, we evaluated time courses from regions corresponding to either superficial vasculature or cortex and compared their spectral features (Fig. 4.1(a)-(c)). This initial survey revealed that spontaneous activity in some mice exhibited a 1/f profile with no distinct peaks other than breathing and pulse in the frequency spectrum (Mouse 1, Fig. 4.1(c_1)), while other mice exhibited either modest (Mouse 2, Fig. 4.1(c_2)) or strong (Mouse 3, Fig. 4.1(c_3)) HONS between 0.16 and 0.32 Hz.

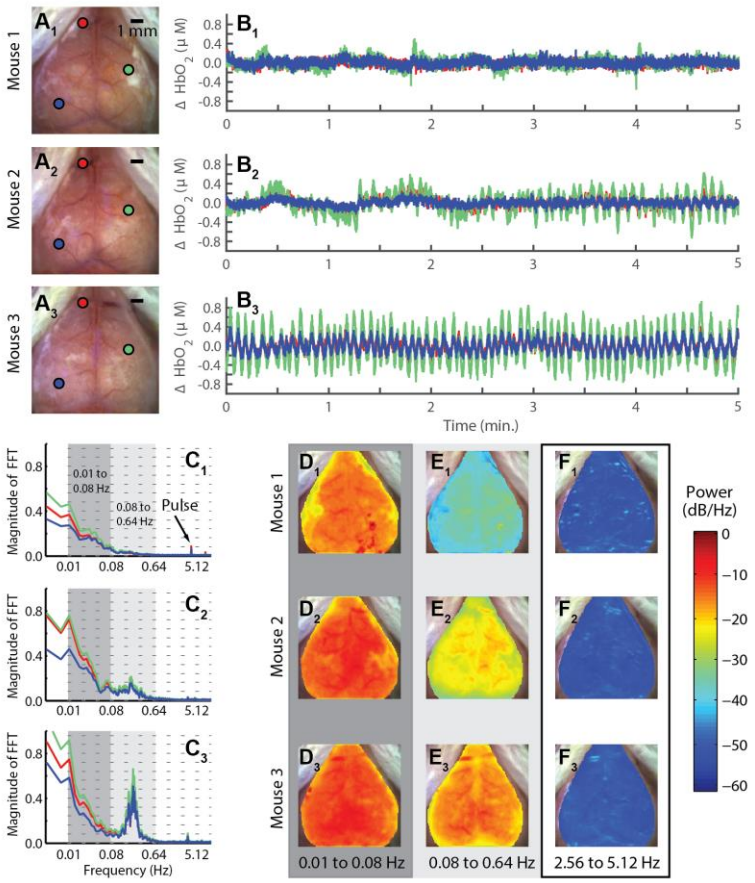

Fig. 4.1. Measurements of low frequency hemodynamics in mouse cortex reveal varying degrees of hemodynamic oscillations with narrow spectral widths (HONS). (**a**). White light images of three mouse cortices (Mice 1-3) with three points selected on each cortex. (**b**) ΔHbO_2 traces of the three points selected in white light image of three mice shown in A. (**c**) Frequency spectra of traces shown in B. The frequency axis is on a log scale, but the labels are linear. The dark gray indicates the canonical bandwidth for functional connectivity analysis (0.01-0.08 Hz), and the light gray indicates the bandwidth in which HONS were found in some of the mice (0.08-0.64 Hz). (**d**) Spectral maps for 0.01 to 0.08 Hz (dark gray region in C). (**e**) Spectral maps for 0.08 to 0.64 Hz (light gray region in C). (**f**) Spectral maps for 2.56 to 5.12 Hz.

To aid in classifying the type of HONS present, the spatial distribution of power was examined over different frequency bands. Specifically, we examined the canonical band used in RSFC analysis (0.01-0.08 Hz; called the RSFC band hereafter, Fig. 4.1(d)), the band containing the distinctive peak identified in Mouse 3 (0.08 to 0.64 Hz; called the HONS band hereafter, Fig.

4.1(e)), and a higher band containing frequencies associated with pulse (2.56 to 5.12 Hz, Fig. 4.1(f)). The spectral maps generated for the HONS band indicates that the HONS identified in Mice 2 and 3 were present over a large region (~1 cm^2).

4.2.3 Broadband Spatiotemporal Patterns in a Mouse with Strong HONS

To further evaluate how the spatiotemporal characteristics of the resting-state signal evolve over time, spontaneous activity in ΔHbO_2, ΔHb_R, and total hemoglobin (ΔHbT) contrasts were analyzed. For illustration, data (Fig. 4.2) are shown for a mouse exhibiting a strong peak in the HONS band (Mouse 3 from Fig. 4.1). Time courses of ΔHbO_2 and ΔHb_R averaged over the brain are out-of-phase and exhibit a peak near 0.2 Hz (Fig. 4.2(a)-(c)). Interestingly, ΔHbT in the brain remained relatively constant over the duration of these oscillations (Fig. 4.2(b)). The image sequence illustrates an oscillation in ΔHbO_2 that propagates over the entire cortex Fig. 4.2(d)).

Two critical steps in RSFC analysis are temporal filtering, and removal of shared regional variance (e.g. the global signal) by linear regression. Both of these are likely to reduce the influence of HONS signals on RSFC analysis. To illustrate the effect of these preprocessing steps, the full-band spontaneous hemodynamics reported in Fig. 4.2 above were separately filtered over either the RSFC or HONS bands for the mouse that had high magnitude HONS (Mouse 3 of Fig. 4.1). After filtering to either band, the global signal was created by averaging all brain pixels within the FOV (Fig. 4.2(a)), and regressed from every pixel's time trace. Within the RSFC band (Fig. 4.3(a)), synchronized spontaneous activity is observed in distinct functional regions (e.g. cingulate cortex from 0 to 4.8 seconds and visual cortex from 22.5 to 28.1 seconds). Conversely, during this same epoch, hemodynamic oscillations within the HONS band (Fig. 4.3(b)) are less spatially specific and resemble wave-like oscillations that can be seen in both cortical tissue and vasculature.

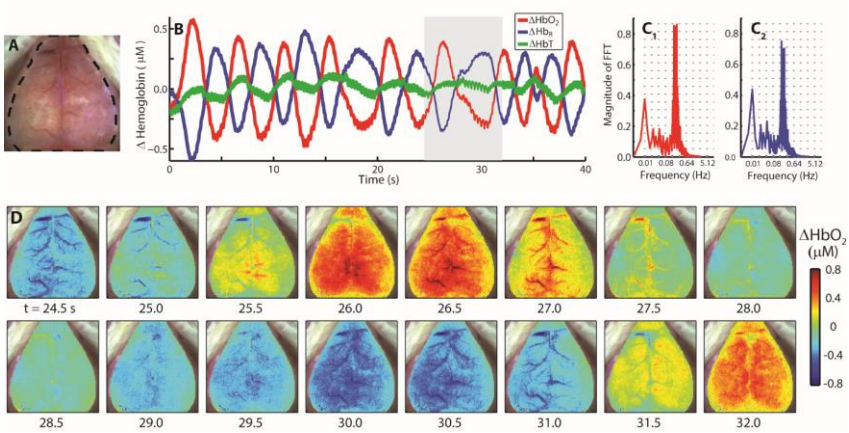

Fig. 4.2. The spatio-temporal features of HONS. (**a**) White light image of Mouse 3 with dashed region indicating which part of image contained a cerebral hemodynamic signal. (**b**) Average ΔHbO_2, ΔHb_R, and ΔHbT traces for the entire region marked in A over 40 seconds. (**c**) FFT of ΔHbO_2 (red) and ΔHb_R (blue) traces shown in B. The spectral peak is at ~0.2 Hz. The frequency axis is on a log scale, but the labels are linear. (**d**) A representative image sequence corresponding to gray region in B. The HONS propagate across the entire cortex.

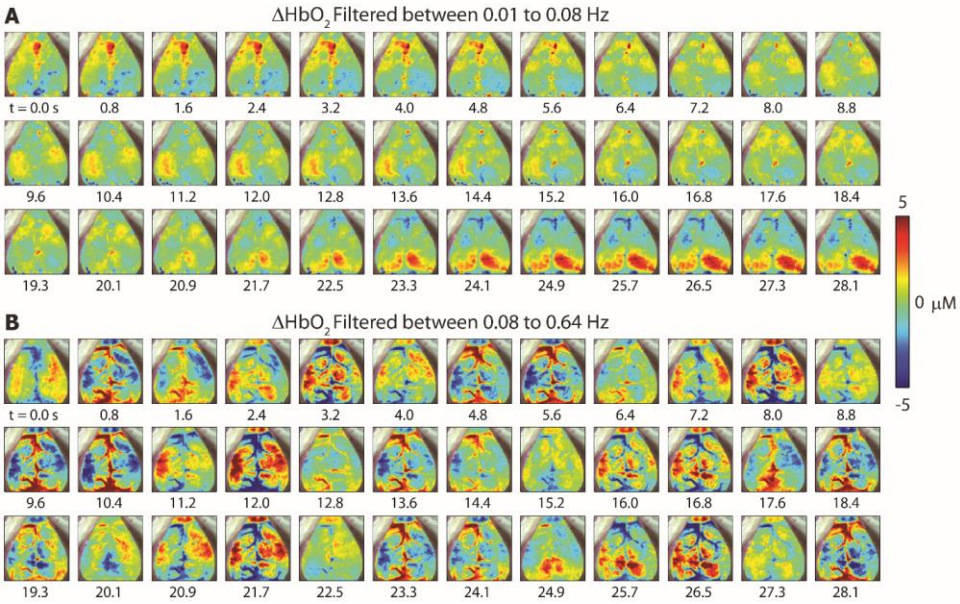

Fig. 4.3. Spatio-temporal patterns of ΔHbO_2 filtered within different bandwidths with removal of the global signal (Mouse 3 in Fig. 4.1). (**a**) Filtered between 0.01 to 0.08 Hz and resampled to 1.25 Hz. Spontaneous correlated activity in somatosensory and visual cortices is present during this 28 second epoch. (**b**) Filtering between 0.08 and 0.64 Hz, a bandwidth containing the distinct peak in the frequency spectrum. The spatio-temporal patterns vary dramatically from those in A.

4.2.4 Effects of Temporal Filtering and Global Signal Regression

We evaluated RSFC within different bandwidths in order to evaluate the effects of HONS and temporal filtering on the topography of functional connectivity patterns. Specifically, ΔHbO_2 traces were filtered using nine different bandwidths with equal relative bandwidth ranging from 0.01 to 5.12 Hz (vertical lines in spectra plots of Fig. 4.1(c)), after which seed-based correlation analysis was used to make RSFC maps (Fig. 4.4).

Similar connectivity patterns are observed over frequency bands less than 0.08 Hz, despite the presence of HONS in Mice 2 and 3 (Fig. 4.4 (a_1-a_3), (b_1-b_3), (c_1-c_3). These correlation maps are comparable to those calculated in previous rodent studies, which generally show strong contralateral homotopic connectivity [26, 75, 116, 117]. High correlations ($r \geq 0.8$) were present in spatially confined regions of the cortex when hemodynamic traces were filtered between 0.04-0.08 Hz. The degree of focal confinement was quantified by calculating the percentage of the cortical field of view with correlation values above 0.8, where a small value indicates a highly focal pattern (3.7% for mouse 1, 7.6% for mouse 2, and 5.0% for Mouse 3).

However, when ΔHbO_2 traces were filtered over bands containing HONS, correlation maps differed dramatically across mice. For example, seed-based correlation maps were mostly bi-modal between the cerebrum and cerebral vasculature in mice with HONS **(**correlation maps contain values near +1 or -1, Fig. 4.4(c_5-c_6). When data were filtered between 0.16-0.32 Hz the correlation values above 0.8 were not focally confined and were present over a large percentage of the cortex in mice with HONS (3.8% for Mouse 1, 19.0% for Mouse 2, and 40.0% for Mouse 3). Correlation maps from higher frequency bands (e.g. > 0.64 Hz) did not have well localized contralateral homotopic regions of high correlation (e.g. Fig. 4.4(a_7-a_9).

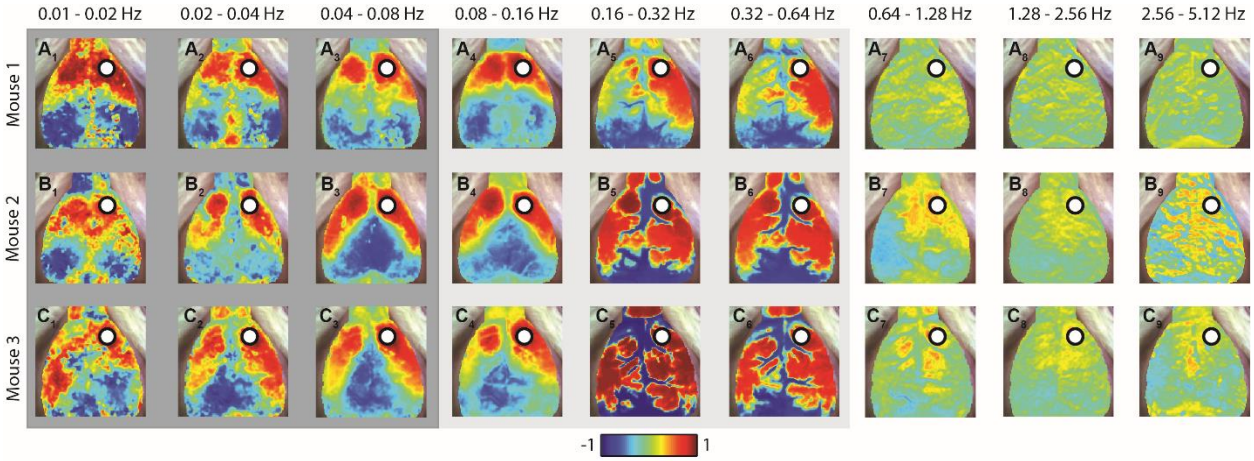

Fig. 4.4. Robustness of resting state functional connectivity in the presence of HONS. Correlation maps generated after filtering with nine different bandwidths with equal relative bandwidth ranging from 0.01 to 5.12 Hz for Mouse 1 (no HONS, $\mathbf{a}_{1\text{-}9}$), Mouse 2 (moderate HONS, $\mathbf{b}_{1\text{-}9}$), and Mouse 3 (strong HONS, $\mathbf{c}_{1\text{-}9}$). Scale bar is for the Pearson correlation coefficient. High correlations ($r \geq 0.8$) were present in spatially confined regions of the cortex when hemodynamic traces were filtered over frequency bands less than the HONS frequency.

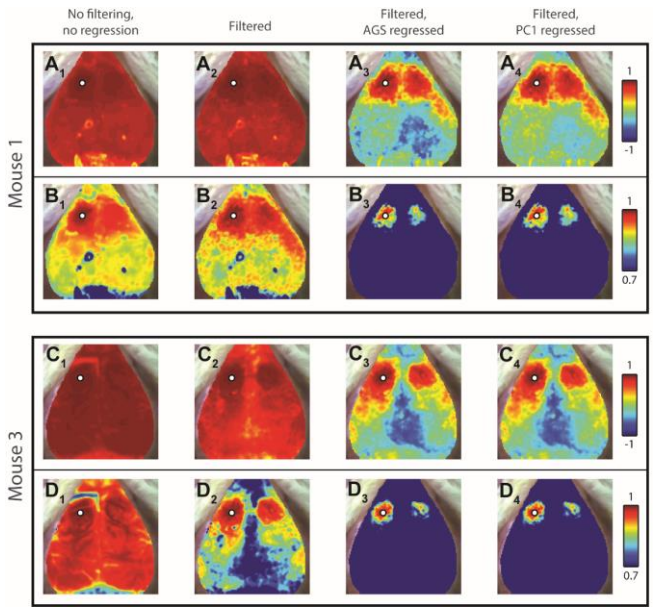

Fig. 4.5. **Effects of global signal regression on seed-based correlation maps in mice with and without HONS.** (**a**) Seed based correlation map for left motor seed during a block with no HONS after four stages of processing: (1) no filtering and no regression, (2) filtering all traces between 0.01 – 0.08 Hz, (3) filtering and regressing out the average global signal (AGS), and (4) filtering and regressing out the first principal component (PC1). The scale bar is for the correlation coefficient, and is set between -1 and 1. The spatial correlation of the correlation maps generated

with the two global signal estimators (B_3 and B_4) is 0.98. The anti-correlation has a greater magnitude when the AGS is used in regression in comparison to PC1 (minimum for AGS is -0.7 and the minimum for the first PC is -0.5). (**b**) Same as A, but with scale bar that has range of 0.7 to 1 to show spatial structure of correlation maps before filtering and regression (**c**) Same as A, but for a mouse with HONS. (**d**) Same as B, but for a mouse with HONS (Mouse 3 in Fig. 1).

We also investigated the effects of global signal regression on the correlation maps generated for mice with and without HONS using two different global signal estimators: the average global signal and the first principal component (Fig. 4.5). Correlation maps were compared across four conditions: (1) no filtering and no regression, (2) filtering in the RSFC bandwidth (0.01-0.08 Hz) and no regression, (3) filtering in the RSFC band followed by global signal regression using the average global signal, and (4) filtering in the RSFC band followed by global signal regression using the first principal component. To visualize the data across the different distributions of correlation coefficients, we displayed the data over two different ranges: [0.7 to 1] and [-1 to 1] (Fig. 4.5). Both filtering and global signal regression focalized high correlations to specific homotopic regions of the brain.

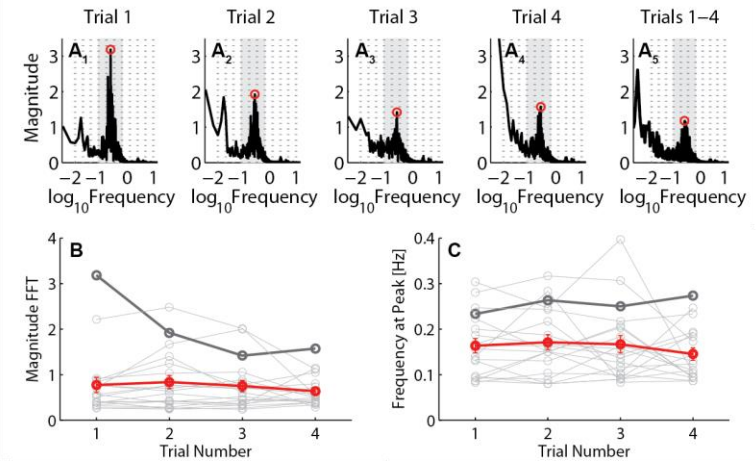

Fig. 4.6. Variability of HONS within the same mouse and across mice. (**a**) Averaged FFT for four five-minute blcoks of a single mouse and the FFT of the entire twenty minute (A_5). (**b**) Peak in the spectrum within the HONS band for every block. Points that are connected correspond to blocks for a single mouse. In dark gray is the mouse

shown in A. In red is the average height of the peak in the FFT for all mice, which is constant over the four blocks. (**c**) Frequency at which the peak in the FFT within the HONS band was detected for all nineteen mice. In dark gray is the mouse in A, and in red is the average frequency across the four blocks for all mice.

4.2.5 Quantifying the Magnitude of HONS Within and Across Mice

Plotting the height of the peak in the FFT across the four five-minute blocks demonstrates that the presence of HONS varies across mice, as well as within mice (Fig. 4.6). To leverage the variability of HONS, all subsequent group analyses were conducted on five-minute blocks.

In order to make comparisons of RSFC in blocks with and without HONS, it was necessary to develop a quantitative metric for the intensity of HONS. There was a total of 76 five-minute blocks analyzed (20 minutes of data for 19 mice). For each five-minute block, the FFT of every ΔHbO_2 trace over the mouse cortex was averaged (Fig. 4.7(a), representative frequency spectra from Mice 1-3). Two metrics were used for quantifying HONS across all 76 blocks: (1) the ratio of the total power within the HONS band and the total power within the RSFC band, and (2) the maximum peak of the averaged spectra within the HONS band. There was a strong correlation (r^2=0.76, p=7.40e-25) between the maximum peak in the HONS band and the ratio of the power within the HONS and RSFC bands (Fig. 4.7(b)). However, the total power in the HONS band was uncorrelated (r^2=0.05, p=0.058) with the total power in the RSFC band (Fig. 4.7(c)). The second metric (maximum peak) was subsequently used to rank the magnitude of HONS in each block in ascending order and produced comparable ranking to the first metric (Fig. 4.7(d)). The metrics calculated for the three representative mice in Figures 4.1-4.4 are highlighted for reference. Given the continuous distribution of sorted blocks using peak magnitude, we opted to include three groups of nearly equal sizes (n=25, n=25, n=26) using the maximum peak metric (Fig. 4.7(d)). The spectral peak location across all blocks with strong HONS (i.e. blocks in Group 3) was 0.2 ± 0.01 Hz.

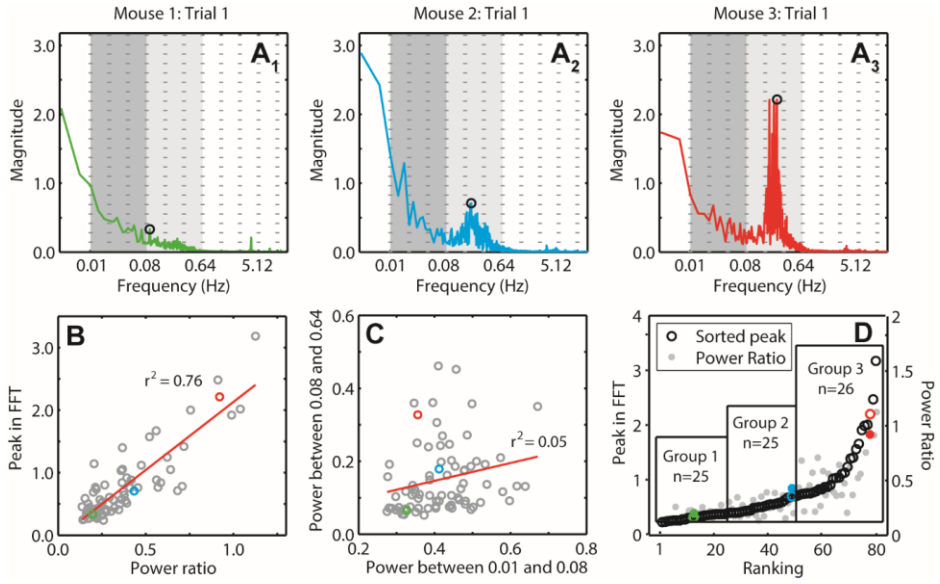

Fig. 4.7. Quantifying and sorting the intensity of HONS in mouse cortex. (**A**) Averaged FFT for five-minute block of Mouse 1 (A_1), Mouse 2 (A_2), and Mouse 3 (A_3). The peak in the spectrum within the bandwidth 0.08-0.64 Hz is marked. These spectra can be quantified by either measures of the peak magnitude or the ratio of the power in the HONS band (0.08-0.64 Hz) to the canonical RSFC band (0.01-0.08 Hz). The frequency axis is on a log scale, but the labels are linear. (**B**) Peak in the FFT within the HONS band plotted against the ratio of the power in the HONS band over the power in the RSFC band. The strong correlation indicates that both measures are congruent. (**C**) The power within the HONS band plotted against the power within the RSFC band. There is weak correlation between the power in these two bands, indicating separation between these two phenomena. (**D**) Results of sorting the 76 five-minute blocks with respect to the peak in the HONS band (also plotted is the power ratio). Values for Mouse 1 are marked in green, Mouse 2 in blue, and Mouse 3 in red. From this sorting, three groups are specified, and were used for group analyses.

4.2.6 Functional Connectivity Versus HONS Amplitude

To test whether the strength of the HONS signal affected the strength of RSFC, we took advantage of the variability in the magnitude of the HONS signal across the 76 blocks. Hemodynamic signals were filtered in the RSFC band, the average global signal was regressed, and seed-based correlation analysis was conducted. We then plotted contralateral homotopic functional connectivity values against the peak magnitude in the HONS band for all 76 blocks. Functional

connectivity patterns for seeds placed in left motor, right retrosplenial, and left visual exhibited variability from one block to another (Fig. 4.8(a)-(c)). However, there was no significant correlation between contralateral homotopic functional connectivity and the intensity of HONS for the three seed regions shown (olfactory: r^2=0.006, somatosensory: r^2=0.007, retrosplenial: r^2=0.004, see Fig. 4.8(a)-(c)), as well as when averaging across the eight homologous brain regions (r^2=0.006, Fig. 4.8(d)). The results for ΔHb_R were comparable to ΔHbO_2.

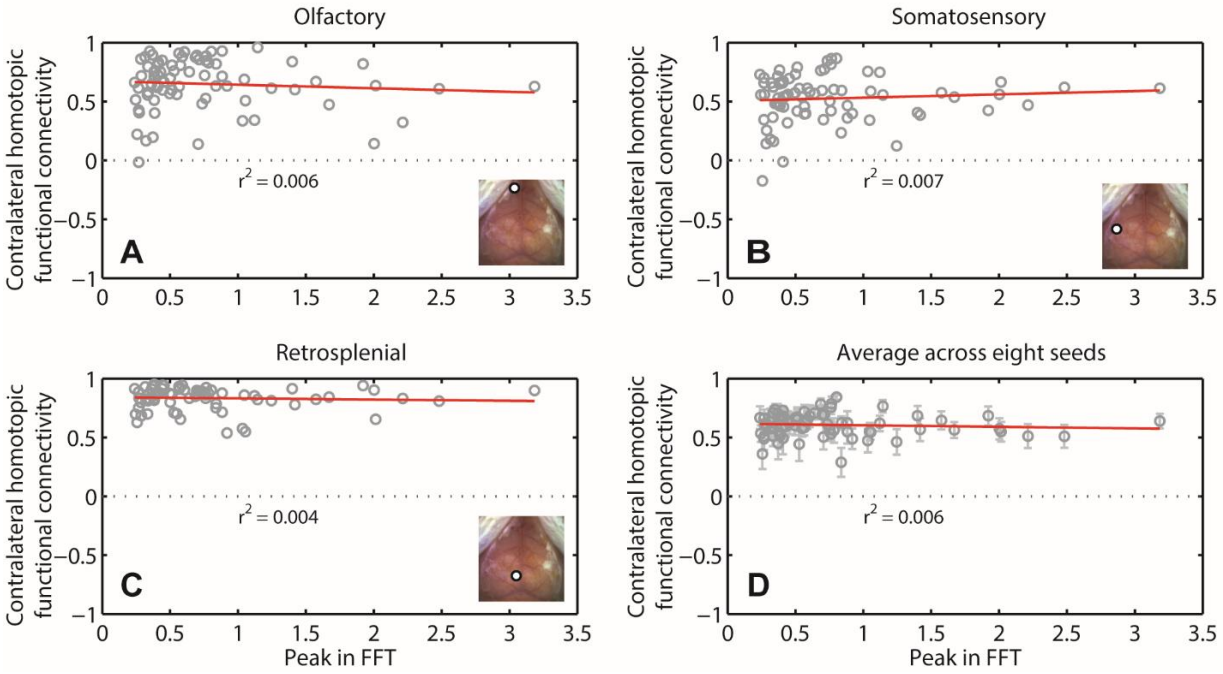

Fig. 4.8. Contralateral homotopic connectivity is not strongly correlated with the intensity of HONS. (**a**) Contralateral homotopic connectivity for olfactory seed measured after filtering ΔHbO_2 data within the RSFC band is plotted against the intensity of HONS. Each point corresponds to a single five-minute block. There is weak correlation between the peak in the FFT and contralateral homotopic connectivity. Inset shows white light image with seed region specified. (**b-c**) Same as A, but for somatosensory and retrosplenial cortices. (**d**) Average contralateral homotopic connectivity for eight brain regions (frontal, cingulate, motor, somatosensory, retrosplenial, visual, auditory, and olfactory) plotted against the intensity of HONS. R-squared value for linear fit of the data is also displayed. These results show that HONS do not affect the magnitude of correlation values when data are filtered between 0.01 to 0.08 Hz.

In addition to assessing the dependence of RSFC results on the magnitude of HONS using linear regression, we also conducted group analyses to determine if there was a smaller effect size only detectable after averaging across groups. We used the three groups established after ranking with respect to the peak in the HONS band: little to no detectable HONS (Group 1 in Fig. 4.7(d)), modest HONS (Group 2), and strong HONS (Group 3). The Pearson correlation coefficient between the 16 seeds was averaged within the three groups and displayed in a correlation matrix (Fig. 4.9(a), contralateral homotopic functional connectivity values are indicated with dashed boxes). There was no significant difference in the mean contralateral homotopic functional connectivity values across the three groups (see methods; Fig. 4.9(b)). We then averaged the correlation maps for the eight homologous regions (Fig. 4.9(c)-(e)). These maps show that resting-state brain networks identified using seed-based correlation analysis had similar spatial features regardless of the intensity of HONS measured in each group. Results were similar when the analysis was conducted with ΔHb_R.

We used our results from the group analysis to better quantify the topography of typical resting-state correlation maps in mice. Seed-based correlation maps averaged from the 25 blocks without HONS were treated as canonical RSFC maps in mice (Fig. 4.9(c)). The spatial structure of other seed-based correlation maps was then compared to these canonical RSFC maps and a similarity score was determined by calculating the 2-D spatial correlation coefficient between the two images. For example, the canonical motor seed map (Fig. 4.9(b_4)) was compared to the correlation maps produced after filtering ΔHbO_2 in nine different bandwidths for the three mice analyzed initially in this report (Fig. 4.4). Correlation maps produced when filtering in frequency bands less than 0.08 Hz had a high spatial similarity to the canonical motor seed map for all three mice (Fig. 4.10(a)-(e)). When data were filtered in a frequency band containing HONS, the spatial correlation

with the canonical motor seed map decreased in the two mice that had HONS. These results are in agreement with the loss of focal correlations measured by calculating the percent of the cortex with high correlation values (Fig. 4.10(f)).

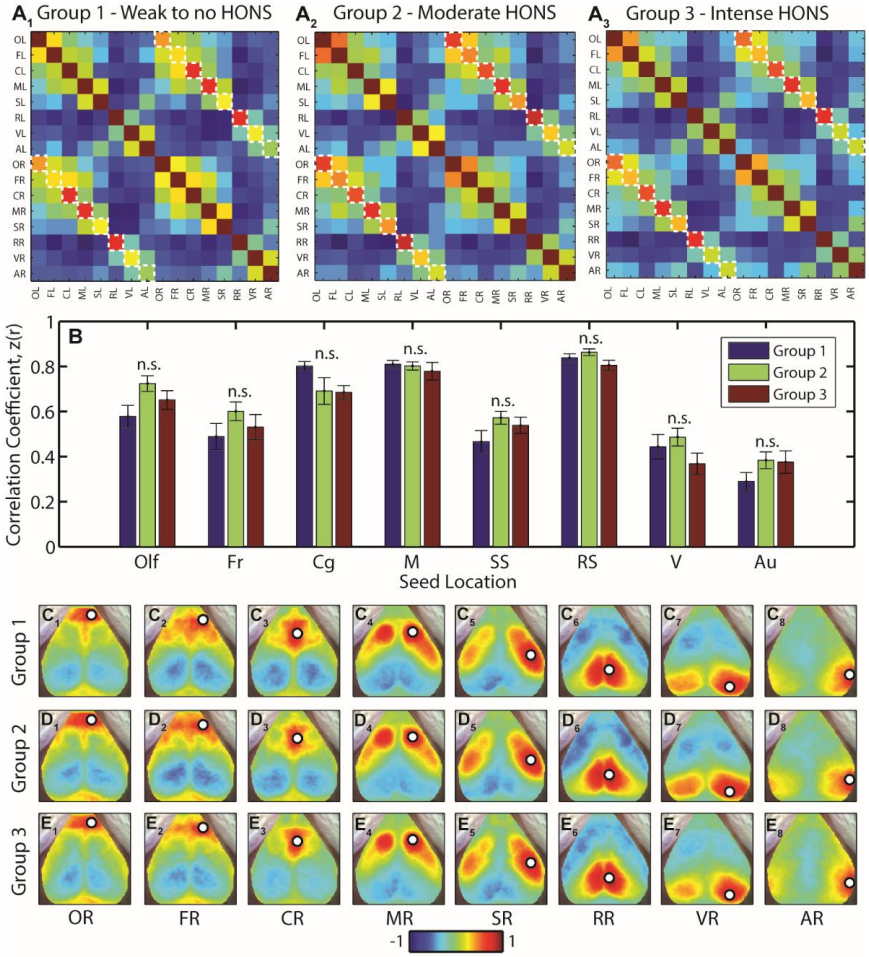

Fig. 4.9. Functional connectivity brain networks across groups are not affected in mice with HONS. (**a**) Seed-seed correlation matrices for the three groups indicated in Fig. 4.7. The results were generated after filtering ΔHbO_2 data within the RSFC band. Contralateral homotopic functional connectivity values are marked with a white dashed line. (**b**) Z-scores for contralateral homotopic functional connectivity values for eight seeds for all three groups. There is no statistically significant difference in contralateral homotopic functional connectivity values across the three groups. Multiple comparisons corrected for using Benjamini and Hochberg's FDR-controlling procedure ($\alpha = 0.05$). (**c**) Correlation maps for right olfactory bulb (C_1), frontal (C_2), cingulate (C_3), motor (C_4), somatosensory (C_5), retrosplenial (C_6), visual (C_7), and auditory (C_8) cortices for mice in group 1. (**d-e**) Same as C, but for groups 2 and 3.

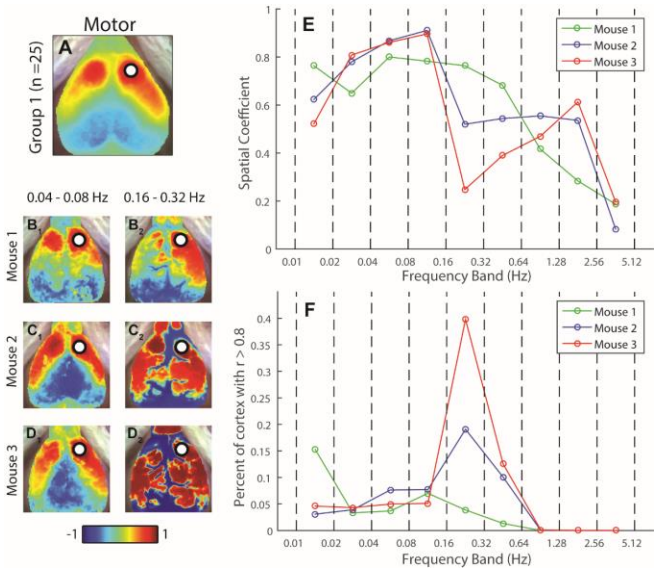

Fig. 4.10. **Quantitative analysis of correlation maps produced after filtering ΔHbO_2 in different frequency bands.** (**a**) Average motor seed correlation map for blocks that had little to no HONS (Fig. 4.9(c_4)). Seed is marked with white point. There were a total of 25 blocks averaged. (**b**) Correlation maps generated after filtering ΔHbO_2 in two bandwidths (0.04-0.08 Hz and 0.16-0.32 Hz) for a mouse with no HONS. (**c**) Same as B, but a mouse with moderate HONS. (**d**) Same as B, but a mouse with strong HONS. (**e**) Spatial correlation coefficient calculated between canonical map for motor seed (shown in A) and maps generated after filtering ΔHbO_2 in different bandwidths. In the mice with HONS, the spatial correlation coefficient drops in bandwidths containing the HONS frequency. (**f**) Percentage of the mouse cortex that contains correlation coefficients greater than or equal to 0.8 as a function of the bandwidth used to filter ΔHbO_2 traces. There are large regions of high correlations in mice with HONS when the data is filtered in bandwidths containing the HONS frequency.

We used our results from the group analysis to better quantify the topography of typical resting-state correlation maps in mice. Seed-based correlation maps averaged from the 25 blocks without HONS were treated as canonical RSFC maps in mice (Fig. 4.9(c)). The spatial structure of other seed-based correlation maps was then compared to these canonical RSFC maps and a similarity score was determined by calculating the 2-D spatial correlation coefficient between the two images. For example, the canonical motor seed map (Fig. 4.9(b_4)) was compared to the correlation maps produced after filtering ΔHbO_2 in nine different bandwidths for the three mice analyzed

initially in this report (Fig. 4.4). Correlation maps produced when filtering in frequency bands less than 0.08 Hz had a high spatial similarity to the canonical motor seed map for all three mice (Fig. 4.10(a)-(e)). When data were filtered in a frequency band containing HONS, the spatial correlation with the canonical motor seed map decreased in the two mice that had HONS. These results are in agreement with the loss of focal correlations measured by calculating the percent of the cortex with high correlation values (Fig. 4.10(f)).

4.2.7 Discussion

While resting-state patterns of functional connectivity have shed light on the functional organization of brain networks in humans [115], monkeys [113], and rodents [26, 114], the relationship between RSFC and other hemodynamic oscillations like Mayer waves and vasomotion has been rarely discussed in the fMRI literature despite their proximity in frequency [121]. Understanding if patterns of resting-state can be affected by those related to other vascular phenomena will aid in interpreting the etiology of functional connectivity patterns in health and their disruption in disease. In this report, we used OISI to analyze spontaneous hemodynamics in the cerebral cortex of mice and examined the relationship between RSFC and HONS.

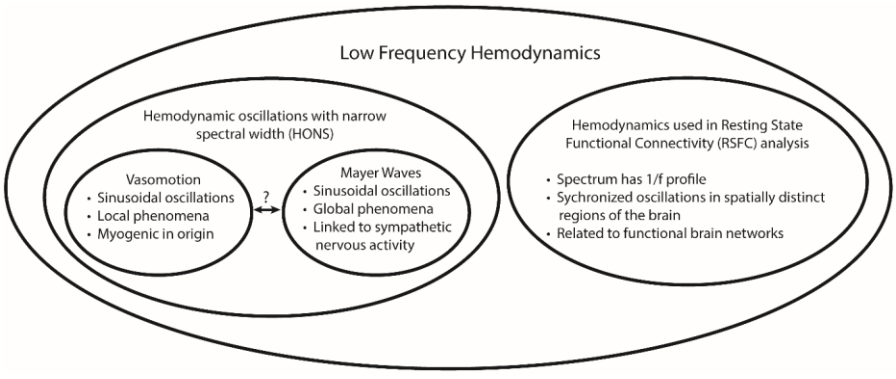

Fig. 4.11. **Classification of low frequency hemodynamic oscillations**. Mayer waves and vasomotion are hemodynamic oscillations with narrow spectrum that are typically reported around 0.1-0.4 Hz, and are more broadly defined as HONS in this report. In comparison, the hemodynamic spectrum of signals used in RSFC analysis has a 1/f profile. RSFC and HONS are different and can be isolated by applying temporal filters.

RSFC and HONS are different phenomena that can be separated by temporal filtering

The presence of HONS in the cerebral cortex is straightforward to detect in the hemodynamic spectra (Fig. 4.1). Unlike the characteristic 1/f profile exhibited by the spontaneous activity used for RSFC analysis, HONS are reasonably sinusoidal phenomena that consequently have a peak with narrow bandwidth, with the center frequency between 0.1-0.4 Hz (Fig. 4.11) [119, 130]. Because the magnitude of HONS varied within and across all 19 mice imaged, we were able to evaluate whether the magnitude of the HONS affected the temporal coherence of resting-state brain networks.

In mice with HONS, there still exists a rich, broadband spectrum of synchronous neural activity throughout the brain that can be used to identify functional networks (Figures 4.4, 4.8, 4.9). These resting-state brain networks were measured by filtering cerebral ΔHbO_2 and ΔHb_R signals between 0.01-0.08 Hz, a bandwidth that excluded potential HONS signals. The topography of these correlation maps are consistent with those measured in other resting-state studies in rodents, regardless of the presence of HONS. Furthermore, the regions of high correlation were well localized, supporting the use of seed-based analysis to map distinctive brain networks when data is filtered in a bandwidth not containing HONS (Fig. 4.10). At the level of individual five-minute scans, there was no correlation between the magnitude of HONS and the strength of functional connectivity between homotopic contralateral regions (Fig. 4.8), a canonical metric used in quantifying functional connectivity patterns [111, 114, 115, 131]. Finally, no difference in RSFC results between mice with and without HONS were measured after averaging results in larger group sizes (Fig. 4.9).

Therefore, our key finding is experimental confirmation that the HONS we have detected are a different phenomenon than those contributing to RSFC patterns in mice, and that they can be

readily characterized and separated by temporal filtering. Though assumed to be true by much of the literature, this provides experimental support that functional connectivity patterns that can recapitulate the functional architecture of the brain, have a completely different physiological source than the HONS measured [7, 112, 132, 133].

Impact of HONS on RSFC analysis in humans: how potential confounds can be avoided

Mayer waves and cerebral vasomotion have been reported in humans, suggesting that HONS may exist in subjects participating in resting-state fMRI studies [127, 134]. Although Mayer waves are primarily associated with changes in ABP during head tilt, they can still be present when subjects are in the supine position. For example, approximately 0.1 Hz oscillations have been detected in blood pressure measurements in eight out of ten healthy human subjects [85]. Cerebral vasomotion was also reported in an awake human subject using both multi-spectral optical intrinsic signal imaging (MS-OISI) and fMRI [126]. These reports, taken together, highlight the prevalence of HONS in humans.

Our data suggest that HONS (whether defined as Mayer waves or cerebral vasomotion) can be detected and separated from hemodynamic signals used in RSFC analysis. Although vasomotion is typically reported in small vascular networks, it too can be easily filtered out of hemodynamic signals due to its narrow spectral width. Spontaneous fluctuations such as Mayer waves and arterial pulsations have also successfully been eliminated in task based functional imaging in humans with diffuse optical tomography (DOT) by using other techniques, such as principal component analysis methods and adaptive filtering [135, 136]. In addition, a near-infrared spectroscopy (NIRS) study demonstrated that a spatially weighted coherence analysis could successfully separate respiration, heart-rate, and arterial pulsation from resting-state data [137]. These studies, as well as our results

in mice, provide support that resting-state fluctuations can be separated from HONS in both humans and mice.

RSFC analysis in humans generally assumes that RSFC is characterized by hemodynamics less than 0.08 or 0.1 Hz. Indeed, there exists evidence that this low-pass cut-off frequency is appropriate for measuring RSFC. The correlation coefficient for auditory, visual, and motor seeds in the resting human brain is highest between 0 to 0.1 Hz, and has been reported to decay by more than two-fold for frequencies ranging from 0.1 to 1.1 Hz in resting-state fMRI [109]. Similar results have also been reported in functional connectivity of homologous and fronto-posterior seed regions using NIRS [138]. In the absence of HONS, our results also show decreases in regional correlation coefficients as ΔHbO_2 was filtered in higher bandwidths (Fig. 4.4(a)).

However, we also found that in mice with significant HONS, the correlation coefficient calculated for hemodynamics filtered between 0.08-0.64 Hz either stayed the same, or increased, and did not reflect the connectivity of resting-brain networks. Instead, high correlation values were calculated for distant brain regions due to the large spatial distribution of the HONS measured (Fig. 4.2 and Fig. 4.10). For instance, the correlation coefficient between left and right motor seeds of Mouse 2 was high ($r = 0.9$) when ΔHbO_2 traces are filtered between 0.16-0.32 Hz (Fig. 4.4(b_5)). This finding could lead to severe misinterpretation of RSFC results for subjects that have significant HONS if the frequency band used for RSFC analysis overlaps with the HONS frequencies.

Another growing technique in RSFC that could be affected by HONS is coherence mapping. In contrast to time correlation, coherence maps are computed by evaluating how correlated the spectral content of hemodynamic signals are across a particular frequency band [139]. This approach has enabled the identification of brain networks that could not be identified using

temporal correlations [140]. However, coherence studies do not often report the presence or absence of HONS in the frequency bands analyzed, and can therefore be confounded when the analysis is extended to higher frequencies ranges in which HONS are potentially present.

Global signal regression

Global signal correction is a common processing step in RSFC analysis and has been shown to remove sources of physiological noise, such as vasomotion and Mayer waves [115, 136, 137]. In this report, we demonstrated that temporal filtering can successfully remove HONS from hemodynamic fluctuations used in RSFC analysis. Because global signal regression with the average global signal is implemented in the majority of RSFC studies, we chose to include it in our processing stream so that (1) we increased the spatial detail and sensitivity of our seed-based correlation maps, and (2) our discussion on human fMRI studies were more relatable. For comparison, we also processed the data without global signal. We demonstrated that the crucial processing step in eliminating HONS from our data was temporal filtering, however, the spatial specificity of the resting-state maps reported here are improved by regressing out the average global signal as expected (Fig. 4.5).

We found similar results when using the first principal component as a global signal estimator. The correlation maps calculated for Mouse 1 show extended anti-correlations when the average global signal was used for regression in comparison to the first principal component. This is in agreement with the spurious anti-correlations predicted by using the average global signal in global signal regression, however the differences between these correlation maps did not alter the primary findings of the study (spatial correlation coefficient was 0.991 for Mouse 1 and 0.997 for Mouse 3) [110]. In general, the spatial correlation between seed-based correlation maps produced with these two different global signal estimators was high ($r = 0.95 \pm 0.0077$; $n = 19$ mice * 4 blocks *

2 contrasts = 152) and the first principal component and the average global signal were also highly correlated ($r = 0.99 \pm 0.00018$; $n = 152$). We therefore focused on use of the average global signal for regression in our analysis, which is the most commonly used global signal estimator in fMRI studies.

The classification and variability of HONS

The classification of HONS as vasomotion or Mayer waves in the cortex is difficult, especially without imaging over a large FOV. Many *in vivo* vasomotion studies have been conducted with point measurements made with optical probes and laser-Doppler flowmetry [123, 125] or microscopes with small FOV [124]. An advantage of using laser-Doppler flowmetry or optical fibers for investigating HONS is their capability of measuring both superficial cortex and deeper brain structure. However, single measurements and small FOV microscopy make it difficult to determine the spatial distribution of 0.1 Hz oscillations over large regions of the body, which has been suggested to be a primary distinction between vasomotion and Mayer waves [120]. NIRS, MS-OISI, and DOT measure ΔHbO_2 and ΔHb_R over large FOVs, and therefore are more suitable for making this distinction [85, 126, 135].

Our OISI system also images a relatively large FOV (approximately 1 cm^2). We therefore were able to determine that the HONS measured were spatially distributed over a large region of the mouse brain (Fig. 4.1(e)), a hallmark of Mayer waves according to reviews in physiology. Given this finding, the HONS with center frequency around 0.2 Hz identified in this study are best characterized as Mayer waves. Reports have shown that the center frequency of the Mayer waves oscillation generally increases for smaller species (for awake subjects: 0.1 Hz for humans, 0.3 Hz for rabbits, and 0.4 Hz for rats). However, studies in rabbits have shown slower Mayer waves

under anesthesia (0.1-0.15 Hz) than when awake [119]. Thus the 0.2 Hz center frequencies seen in this study of mice under anesthesia are in general agreement with previous reports.

A more thorough distinction between cerebral vasomotion and Mayer waves in this report is elusive. Our imaging was performed through the skull, precluding direct imaging of small pial vessels. Furthermore, the hemodynamic measurements in regions corresponding with large blood vessels, likely draining veins, were correlated with the HONS measured over the entire cortex (Fig. 4.1(b_3), (c_3), and (d_3)). Classification of HONS and their relation to neural oscillations could be improved by measuring additional physiological parameters such as electrophysiology, ABP, calcium dynamics, and blood flow [85].

Another interesting aspect of our results was the variability in magnitude of the HONS in mice. As we have shown, the presence of HONS in the cortex varied drastically across and within mice (Fig. 4.6 and Fig. 4.7). From our data, we found no correlate within the RSFC band of the presence or magnitude of HONS (Fig. 4.7(c)). This uncertainty about the physiological cause and magnitude of HONS, is in accordance with the existing literature on Mayer waves and vasomotion [118, 125, 126]. A plausible explanation for the variance of HONS in this study is the competing effects that ketamine and xylazine have on sympathetic nervous system activity and blood pressure [117]. Although the administration of anesthesia was consistent across mice, the level of sedation during imaging was variable due to the IP delivery mechanism. The magnitude of Mayer waves, which are coupled with sympathetic nervous system activity, could be explained by the variance in the anesthesia [119].

Our ability to measure resting-state brain networks in mice anesthetized with ketamine/xylazine is also consistent with previous studies in mice and rats [26, 116, 117]. The spatial symmetry of resting-state brain networks has been shown to be similar regardless of

whether ketamine/xylazine or isoflurane are administered, providing support that intrinsic functional brain structure measured through RSFC analysis exists and is consistent across different anesthesia [117]. However, differences in the topography of resting-state brain networks in awake and anesthetized rodents has not been well studied. The development of *in-vivo* imaging in awake mice provides a promising technology for studying the dependence of HONS on different anesthetics, as well as the effects of anesthesia on RSFC.

Conclusion

Our results show differences in the spatiotemporal and spectral characteristics of HONS and hemodynamics used in RSFC analysis. Despite the proximity in frequency of these phenomena, they can easily be separated by applying appropriate temporal filters. We also demonstrated that the presence of HONS can confound conclusions drawn from RSFC analysis if they are not separated. Fortunately, the HONS frequency band is most often accessible to both fMRI and optical imaging. Therefore, a good practice in RSFC analysis is thorough examination of the hemodynamic (measured with OISI) or blood oxygen level dependent signal (measured with fMRI) frequency spectrum for the possible presence of vasomotion and/or Mayer waves.

4.3 Peri-Infarct Depolarization

4.3.1 Introduction

Focal brain ischemia results in repetitive waves of electrophysiological hyperactivity followed by silence in surrounding cortex, a phenomenon known as peri-infarct depolarization (PID). Propagating at a rate of 2 – 6 mm/min [141], PIDs are hypothesized to exacerbate ischemia in the penumbra [84]. Despite the potential role that PIDs play in ischemic injury, their spatiotemporal propagation over the entire mouse cortex has not been well studied [30, 142]. We have developed an OISI system and image processing algorithms that enable high throughout identification of

PIDs over majority of the mouse cortex. The automated and robust algorithm that has been developed is essential for analyzing the large datasets required to compare PIDs between different groups of mice.

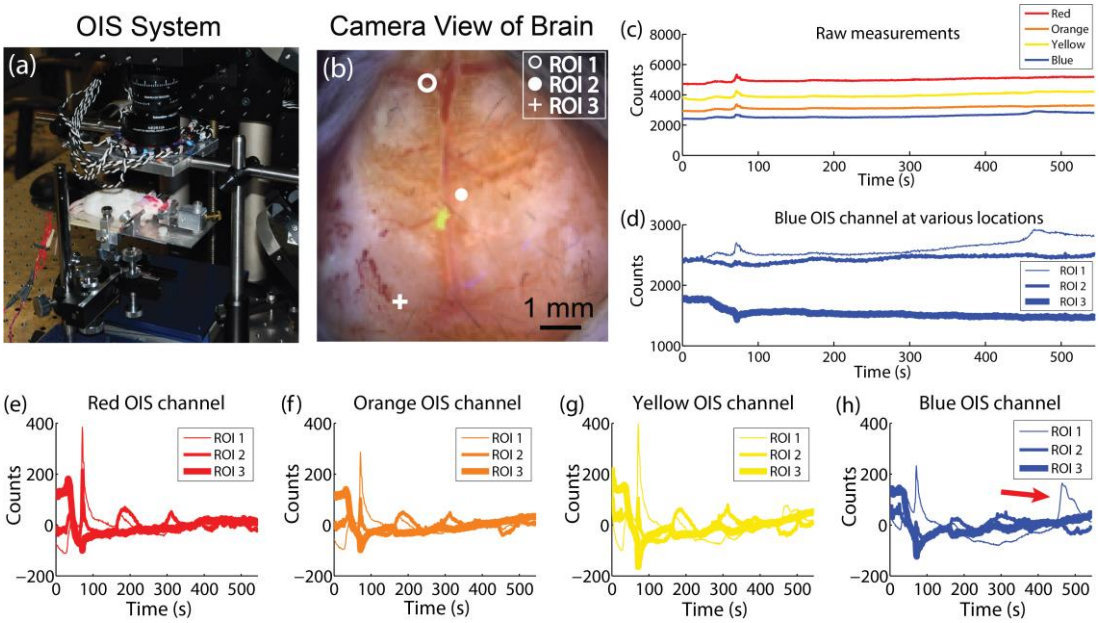

Fig. 4.12 Changes in reflectance detected during PIDs using OISI. (a) Illumination from sequentially flashing LEDs in four different wavelengths (478 nm, 588 nm, 610 nm, and 625 nm) arranged in a ring. Detection by an EMCCD camera is at 120 Hz with 4x4 pixel binning on camera (30 Hz after decoding of wavelengths). Crossed linear polarizers prevent artifacts from specular reflection off the skull. A five minute imaging session produces 1.2 GB of data. (b) A false color image of the mouse cortex generated from the red, yellow, and blue LED channels. The image shows the camera's field-of-view (approximately 1 cm^2) of the mouse brain with the cerebral cortex visible through the skull from the olfactory bulb to the superior colliculus and far laterally on the convexity. Three regions of interest are marked. Mice (male C57Bl6/J, 12-14 weeks old) were anesthetized with 0.75% isoflurane. (c) Raw measurements made by OISI system at ROI 1 shown in B during a five minute trail. The measurements from all four LEDs are shown. (d) Raw blue OISI measurement at the three ROIs. Note the difference in mean counts at each location. (e)-(h) Time traces for four OISI channels at three ROIs after detrending, subtracting the mean from each pixel. Marked in (h) with a red arrow is a PID that was detected in the blue OISI channel. Our data show that the blue OISI channel was most sensitive in measuring PIDs during middle cerebral artery occlusion (MCAO) in mice.

4.3.2 Methods

Ten mice (male C57Bl6/J, 12-14 weeks old) were anesthetized with 0.75% isoflurane and imaged up to 6 hours during middle cerebral artery occlusion (MCAO). Light emitting diodes (LEDs) operating at four wavelengths (478 nm, 588 nm, 610 nm, and 625 nm) illuminated the skull, and diffuse reflected light was detected by an EMCCD camera (Fig. 4.12(a)-(b)). For reference, we plotted both the average signal over the brain for each wavelength (Fig. 4.12(c)), as well as the blue reflectance data at three regions of interest (ROIs) in the brain (Fig. 4.12(d)). Images collected from light reflected at 478nm resulted in the largest percent change in signal during PIDs, and were therefore used for detecting and quantifying PIDs (Fig. 4.12(e)-(h)). To detect and visualize PIDs, the mean count value at each pixel was subtracted from that pixel's time trace.

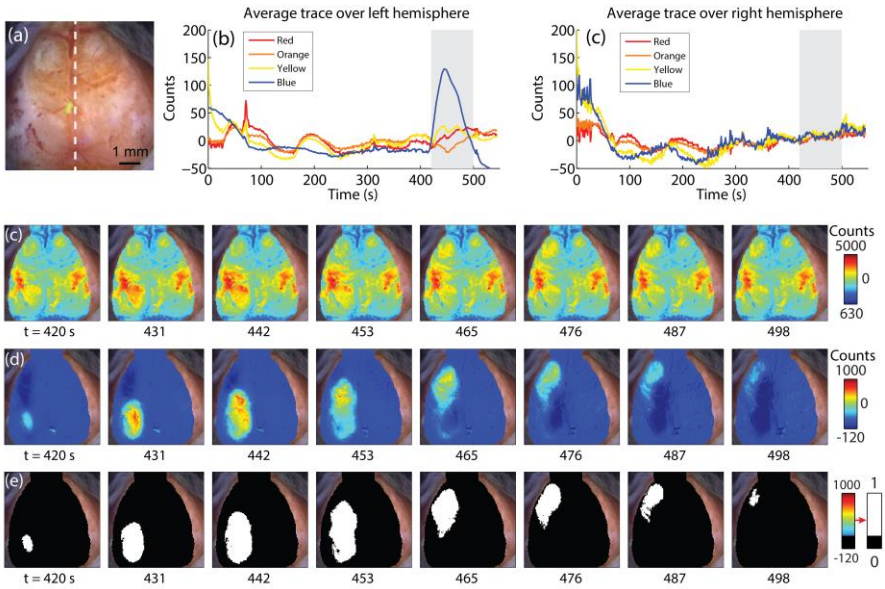

Fig. 4.13. Propagation of PIDs across mouse cortex after stroke. (a) False color image of mouse cortex. White dashed line separates left and right hemispheres. (b) Averaged time trace of all pixels on the left hemisphere. All four colors are shown. The region in gray indicates the epoch in which a PID is present. (c) Same as B, but traces over the right hemisphere are averaged. (d) Image sequence of raw blue OIS signal measured during the gray highlighted epoch in B and C. The frames have been resampled for fitting the entire epoch. (e) Same as D, but after the data has been processed. The PID is now easily visible. (f) Image sequence for same epoch after applying a threshold and creating a binary image mask.

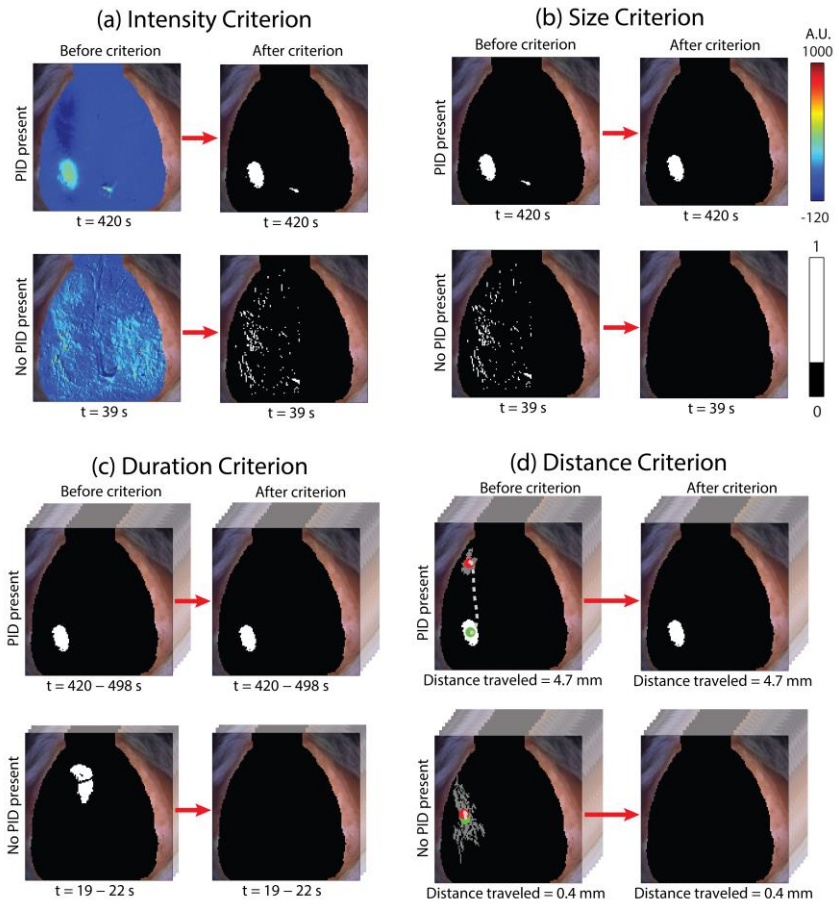

Fig. 4.14. Developing automated detection of PIDs in mouse cortex. Image processing criteria for automatically detecting PIDs measured with OISI. A. After processing data collected during imaging trial (typically nine minutes), images are converted to binary image masks. A threshold of 15% the maximum intensity over the entire field of view and trial is applied. Shown are examples of frames with and without PIDs before and after applying the threshold. B. Segments in the binary image less than 0.9 mm2 are removed from the mask. C. Visualization of duration criterion. Binary image sequences must have a segment for at least 20 seconds to be considered a potential PID. D. The final criterion applied requires that the first and last segment of an image sequence have a separation of 2.3mm. Segment in white corresponds to first frame of sequence and segment in gray corresponds to last frame in sequence. The green and red points indicate the centroids of the first and final segment respectively.

4.3.3 Results and Discussion

A representative PID detected in a mouse is shown in Fig. 4.13. The average signal over the left and right hemispheres of the brain reveal a PID propagating across the left hemisphere between

400 and 500 seconds (Fig. 4.13(a)-(c)). Without subtracting the mean from each pixel it is difficult to visualize the PID trajectory (Fig. 4.13(d)). However, after mean subtraction, it becomes clear that the PID propagates from the posterior to anterior region of the mouse cortex (Fig. 4.13(e)). Segmentation of the image is required for subsequent quantification of the PID (Fig. 4.13(f)).

PIDs were detected by applying several criteria to create an image mask over the trial: (1) an image intensity threshold, (2) a minimum image area threshold, and (3) a minimum distance of propagation threshold (Fig 4.14). In addition to detecting PIDs, the algorithm also calculated the duration, source and sink, average velocity, and spatial trace of the PID (Fig. 4.15). After the automated identification of PIDs, the user can inspect the intensity trace (Fig 4.12), the spatial location of the mask over the trial (Fig 4.15(a)), and the trace of the PID (Fig. 4.15(b)) to identify potential false positives and false negatives.

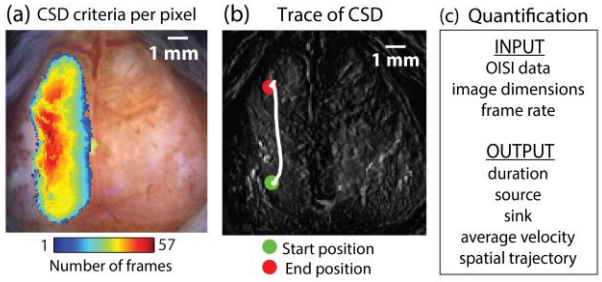

Fig. 4.15. Quantification of PIDs. (a) Number of frames for which each pixel satisfied all PID criteria. (b) Trajectory of weighted centroid of PID during propagation over the left hemisphere of the mouse cortex. (c) The input and output of PID detection algorithm.

The efficiency of the algorithm was determined by identifying PIDs manually and comparing these findings to the PIDs detected by the algorithm. Ten mice were imaged up to six hours during MCAO with our OISI system. Our algorithm automatically detected PIDs that occurred after MCAO in these mice. During the 50 hours of data analyzed, there was a total of 208 PIDs (4.15 PIDs/hour). The sensitivity and specificity of the algorithm was 0.93 and 0.97 respectively, and there was a false positive and false negative rate of 0.11 and 0.07. Using our data visualization

output, a user can identify these false positives and negatives at around five times faster than manually watching all trials.

Our imaging system and processing algorithm efficiently identifies PIDs over the mouse cortex, and provides quantitative information about the propagation of PIDs that cannot be calculated by manual inspection. This high-throughput approach to analyzing PIDs significantly reduces the need for manual user input. An exciting application of this system and detection algorithm is to identify differences in duration, number, or propagation of PIDs in mouse models of stroke. Drugs or genetic manipulations that reduce PIDs after MCAO could be tested for attenuation of ischemic brain injury.

Chapter 5: Conclusion

Improvement in optical imaging technology and FP engineering have revolutionized how researchers study the function and structure of the mouse brain. Across all the technologies available, there are fundamental trade-offs between FOV, resolution, SNR, and imaging speed [2, 13, 29, 143, 144]. Therefore, selecting an imaging modality for answering a particular biological question takes careful consideration of the imaging parameters necessary for the experiment and the other specifications that will be consequently compromised. Perhaps one of the greatest challenges in neuroscience is then connecting discoveries made at one spatial and temporal scale to how the brain is studied and understood at other spatial and temporal scales. My dissertation has focused on addressing this challenge by developing tools capable of imaging the mouse brain over a large range of spatial scales.

In developing LF-TPM, I focused specifically on the trade-off between FOV and resolution and have realized important design strategies for constructing a cost-effective system with large

FOV and cellular resolution. Our goal was to design a system with FOV that was comparable to OISI, while maintaining cellular resolution. In general, perhaps the better goal for designing multiscale imaging systems is maximizing the amount of information that can be collected from the sample, which is nicely summarized by considering the SBP of the optical imaging system. However, a more valuable metric to assess multiscale imaging should include volumetric imaging, implying that the SBP should also be representative of imaging depth and axial resolution. The analysis becomes more complicated because imaging depth, axial resolution, and collection efficiency all depend on the objective NA in counteracting ways (see Section 2.5). With these considerations, the ideal objective lens for maximizing the volumetric SBP would likely have focal length ranging from 10mm to 20mm and NA 0.8 to NA 0.6. Unfortunately, there are not many commercially available objectives with these specifications, and instead more focus is placed on developing higher NA objective lenses (NA>0.8). The bigger issue, which is the focus of Chapter 2 of my dissertation, is the lack of commercially available components capable of supporting high throughput objective lenses. Therefore, there is need in the field of multiscale imaging for objectives and optical components that are designed to optimize the volumetric SBP.

More importantly, however, true progress in multiscale imaging will likely require rethinking how information transmission is maximized within a single image and with respect to time in optical systems (i.e. how volumetric SBP and pixel rate can be maximized while maintaining sufficient SNR) beyond just increasing the optical throughput of the system. For instance, Fourier ptychography is capable of imaging a large SBP with a relatively low-cost system by iteratively illuminating the sample with differently angled plane waves [145].

Although optimizing the SBP informed our design decisions for developing the first-generation LF-TPM system presented in this dissertation, we put little emphasis on a crucial

parameter in functional imaging of the mouse brain: imaging speed [4, 16, 23]. Currently, the speed of our LF-TPM system is limited by use of traditional mirror galvanometers for scanning. Due to the fact that the back aperture is underfilled, a resonant galvanometer is close to matching the throughput of the microscope. Therefore, a solution is to introduce another relay or virtually conjugate the fast scanner with another galvanometer [49, 65, 88]. The latter option will be more challenging to implement, but will eliminate the need to design another optical relay. We have also considered introducing a diffractive optical element or spatial light modulator to multiplex the beam at the specimen, which would require parallel detection with a multi-channel PMT [6, 146]. Despite the current speed limitations and anisotropic PSF, the LF-TPM system that we developed holds promise in addressing the multiscale imaging challenges currently faced in the field of neuroscience.

In addition to my work in microscope design and implementation, I used OISI for studying the following large scale neural phenomena in mice: functional connectivity, Mayer waves, and PIDs. These studies complemented my work in LF-TPM because they provided imaging data with high temporal resolution (30Hz frame rate) and poor spatial resolution (approximately 200μm lateral resolution), whereas LF-TPM provided imaging data with the opposite trade-off. Similar to my work on extending the FOV in TPM for mesoscopic studies, there is potential for redesigning MOI-WFI for analyzing the dynamics of individual cells [147]. Although such a system would not have axial specificity, it would be simpler and be approximately ¼ the cost of our LF-TPM system. Aside from system development, my work using OISI has provided insight into the spatiotemporal patterns of spontaneous neural phenomena in the mouse cortex. The discoveries I have made in these studies and the design strategies outlined for developing LF-TPM will serve as important

stepping stones in advancing mesoscopic imaging of the structure and function of the mouse cortex.

References

1. A. K. Dunn, A. Devor, A. M. Dale, and D. A. Boas, "Spatial extent of oxygen metabolism and hemodynamic changes during functional activation of the rat somatosensory cortex," NeuroImage **27**, 279-290 (2005).

2. A. N. King, C. F. Manning, and J. S. Trimmer, "A unique ion channel clustering domain on the axon initial segment of mammalian neurons," The Journal of comparative neurology **522**, 2594-2608 (2014).

3. R. Prevedel, Y. G. Yoon, M. Hoffmann, N. Pak, G. Wetzstein, S. Kato, T. Schrodel, R. Raskar, M. Zimmer, E. S. Boyden, and A. Vaziri, "Simultaneous whole-animal 3D imaging of neuronal activity using light-field microscopy," Nature methods **11**, 727-730 (2014).

4. M. B. Ahrens and F. Engert, "Large-scale imaging in small brains," Current opinion in neurobiology **32**, 78-86 (2015).

5. D. H. Lim, J. M. LeDue, and T. H. Murphy, "Network analysis of mesoscale optical recordings to assess regional, functional connectivity," Neurophotonics **2**(2015).

6. N. Ji, J. Freeman, and S. L. Smith, "Technologies for imaging neural activity in large volumes," Nature neuroscience **19**, 1154-1164 (2016).

7. S. M. Smith, D. Vidaurre, C. F. Beckmann, M. F. Glasser, M. Jenkinson, K. L. Miller, T. E. Nichols, E. C. Robinson, G. Salimi-Khorshidi, M. W. Woolrich, D. M. Barch, K. Ugurbil, and D. C. Van Essen, "Functional connectomics from resting-state fMRI," Trends in cognitive sciences **17**, 666-682 (2013).

8. J. A. Filosa and J. A. Iddings, "Astrocyte regulation of cerebral vascular tone," American journal of physiology. Heart and circulatory physiology **305**, H609-619 (2013).

9. J. J. Jun, N. A. Steinmetz, J. H. Siegle, D. J. Denman, M. Bauza, B. Barbarits, A. K. Lee, C. A. Anastassiou, A. Andrei, C. Aydin, M. Barbic, T. J. Blanche, V. Bonin, J. Couto, B. Dutta, S. L. Gratiy, D. A. Gutnisky, M. Hausser, B. Karsh, P. Ledochowitsch, C. M. Lopez, C. Mitelut, S. Musa, M. Okun, M. Pachitariu, J. Putzeys, P. D. Rich, C. Rossant, W. L. Sun, K. Svoboda, M. Carandini, K. D. Harris, C. Koch, J. O'Keefe, and T. D. Harris, "Fully integrated silicon probes for high-density recording of neural activity," Nature **551**, 232-236 (2017).

10. M. H. Mohajerani, D. A. McVea, M. Fingas, and T. H. Murphy, "Mirrored bilateral slow-wave cortical activity within local circuits revealed by fast bihemispheric voltage-sensitive dye imaging in anesthetized and awake mice," The Journal of neuroscience : the official journal of the Society for Neuroscience **30**, 3745-3751 (2010).

11. T. W. Chen, T. J. Wardill, Y. Sun, S. R. Pulver, S. L. Renninger, A. Baohan, E. R. Schreiter, R. A. Kerr, M. B. Orger, V. Jayaraman, L. L. Looger, K. Svoboda, and D. S. Kim,

"Ultrasensitive fluorescent proteins for imaging neuronal activity," Nature **499**, 295-300 (2013).

12. W. R. Zipfel, R. M. Williams, and W. W. Webb, "Nonlinear magic: multiphoton microscopy in the biosciences," Nature biotechnology **21**, 1369-1377 (2003).

13. S. P. Peron, J. Freeman, V. Iyer, C. Guo, and K. Svoboda, "A Cellular Resolution Map of Barrel Cortex Activity during Tactile Behavior," Neuron **86**, 783-799 (2015).

14. P. J. Drew, A. Y. Shih, and D. Kleinfeld, "Fluctuating and sensory-induced vasodynamics in rodent cortex extend arteriole capacity," Proceedings of the National Academy of Sciences of the United States of America **108**, 8473-8478 (2011).

15. G. F. Hammen, D. Turaga, T. E. Holy, and J. P. Meeks, "Functional organization of glomerular maps in the mouse accessory olfactory bulb," Nature neuroscience **17**, 953-961 (2014).

16. M. B. Bouchard, V. Voleti, C. S. Mendes, C. Lacefield, W. B. Grueber, R. S. Mann, R. M. Bruno, and E. M. Hillman, "Swept confocally-aligned planar excitation (SCAPE) microscopy for high speed volumetric imaging of behaving organisms," Nature photonics **9**, 113-119 (2015).

17. A. Perez-Alvarez, A. Araque, and E. D. Martin, "Confocal microscopy for astrocyte in vivo imaging: recycle and reuse in microscopy," Frontiers in cellular neuroscience **7**(2013).

18. M. B. Ahrens, M. B. Orger, D. N. Robson, J. M. Li, and P. J. Keller, "Whole-brain functional imaging at cellular resolution using light-sheet microscopy," Nature methods **10**, 413-420 (2013).

19. S. Wolf, W. Supatto, G. Debregeas, P. Mahou, S. G. Kruglik, J. M. Sintes, E. Beaurepaire, and R. Candelier, "Whole-brain functional imaging with two-photon light-sheet microscopy," Nature methods **12**, 379-380 (2015).

20. T. Schrodel, R. Prevedel, K. Aumayr, M. Zimmer, and A. Vaziri, "Brain-wide 3D imaging of neuronal activity in Caenorhabditis elegans with sculpted light," Nature methods **10**, 1013-1020 (2013).

21. J. P. Nguyen, F. B. Shipley, A. N. Linder, G. S. Plummer, M. Liu, S. U. Setru, J. W. Shaevitz, and A. M. Leifer, "Whole-brain calcium imaging with cellular resolution in freely behaving Caenorhabditis elegans," Proceedings of the National Academy of Sciences of the United States of America **113**, E1074-E1081 (2016).

22. P. J. Keller and M. B. Ahrens, "Visualizing Whole-Brain Activity and Development at the Single-Cell Level Using Light-Sheet Microscopy," Neuron **85**, 462-483 (2015).

23. R. M. Power and J. Huisken, "A guide to light-sheet fluorescence microscopy for multiscale imaging," Nature methods **14**, 360-373 (2017).

24. K. Ohki, S. Chung, Y. H. Ch'ng, P. Kara, and R. C. Reid, "Functional imaging with cellular resolution reveals precise micro-architecture in visual cortex," Nature **433**, 597-603 (2005).

25. Y. Ma, M. A. Shaik, S. H. Kim, M. G. Kozberg, D. N. Thibodeaux, H. T. Zhao, H. Yu, and E. M. Hillman, "Wide-field optical mapping of neural activity and brain haemodynamics: considerations and novel approaches," Philosophical transactions of the Royal Society of London. Series B, Biological sciences **371**(2016).

26. B. R. White, A. Q. Bauer, A. Z. Snyder, B. L. Schlaggar, J. M. Lee, and J. P. Culver, "Imaging of functional connectivity in the mouse brain," PloS one **6**, e16322 (2011).

27. A. Devor, A. K. Dunn, M. L. Andermann, I. Ulbert, D. A. Boas, and A. M. Dale, "Coupling of total hemoglobin concentration, oxygenation, and neural activity in rat somatosensory cortex," Neuron **39**, 353-359 (2003).

28. J. A. Heimel, R. J. Hartman, J. M. Hermans, and C. N. Levelt, "Screening mouse vision with intrinsic signal optical imaging," Eur J Neurosci **25**, 795-804 (2007).

29. P. W. Wright, L. M. Brier, A. Q. Bauer, G. A. Baxter, A. W. Kraft, M. D. Reisman, A. R. Bice, A. Z. Snyder, J. M. Lee, and J. P. Culver, "Functional connectivity structure of cortical calcium dynamics in anesthetized and awake mice," PloS one **12**(2017).

30. A. M. Ba, M. Guiou, N. Pouratian, A. Muthialu, D. E. Rex, A. F. Cannestra, J. W. Chen, and A. W. Toga, "Multiwavelength optical intrinsic signal imaging of cortical spreading depression," Journal of neurophysiology **88**, 2726-2735 (2002).

31. J. B. Ackman, T. J. Burbridge, and M. C. Crair, "Retinal waves coordinate patterned activity throughout the developing visual system," Nature **490**, 219-225 (2012).

32. J. R. Bumstead, A. Q. Bauer, P. W. Wright, and J. P. Culver, "Cerebral functional connectivity and Mayer waves in mice: Phenomena and separability," Journal of cerebral blood flow and metabolism : official journal of the International Society of Cerebral Blood Flow and Metabolism **37**, 471-484 (2017).

33. L. Tian, S. A. Hires, T. Mao, D. Huber, M. E. Chiappe, S. H. Chalasani, L. Petreanu, J. Akerboom, S. A. McKinney, E. R. Schreiter, C. I. Bargmann, V. Jayaraman, K. Svoboda, and L. L. Looger, "Imaging neural activity in worms, flies and mice with improved GCaMP calcium indicators," Nature methods **6**, 875-881 (2009).

34. K. M. Dean and A. E. Palmer, "Advances in fluorescence labeling strategies for dynamic cellular imaging," Nat Chem Biol **10**, 512-523 (2014).

35. T. W. Chen, T. J. Wardill, Y. Sun, S. R. Pulver, S. L. Renninger, A. Baohan, E. R. Schreiter, R. A. Kerr, M. B. Orger, V. Jayaraman, L. L. Looger, K. Svoboda, and D. S. Kim, "Ultrasensitive fluorescent proteins for imaging neuronal activity," Nature **499**, 295-+ (2013).

36. P. T. So, C. Y. Dong, B. R. Masters, and K. M. Berland, "Two-photon excitation fluorescence microscopy," Annual review of biomedical engineering **2**, 399-429 (2000).

37. E. M. Hillman, "Optical brain imaging in vivo: techniques and applications from animal to man," Journal of biomedical optics **12**, 051402 (2007).

38. A. Ibraheem and R. E. Campbell, "Designs and applications of fluorescent protein-based biosensors," Current opinion in chemical biology **14**, 30-36 (2010).

39. J. Akerboom, T. W. Chen, T. J. Wardill, L. Tian, J. S. Marvin, S. Mutlu, N. C. Calderon, F. Esposti, B. G. Borghuis, X. R. Sun, A. Gordus, M. B. Orger, R. Portugues, F. Engert, J. J. Macklin, A. Filosa, A. Aggarwal, R. A. Kerr, R. Takagi, S. Kracun, E. Shigetomi, B. S. Khakh, H. Baier, L. Lagnado, S. S. H. Wang, C. I. Bargmann, B. E. Kimmel, V. Jayaraman, K. Svoboda, D. S. Kim, E. R. Schreiter, and L. L. Looger, "Optimization of a GCaMP Calcium Indicator for Neural Activity Imaging," Journal of Neuroscience **32**, 13819-13840 (2012).

40. Q. Chen, J. Cichon, W. Wang, L. Qiu, S. J. Lee, N. R. Campbell, N. Destefino, M. J. Goard, Z. Fu, R. Yasuda, L. L. Looger, B. R. Arenkiel, W. B. Gan, and G. Feng, "Imaging neural activity using Thy1-GCaMP transgenic mice," Neuron **76**, 297-308 (2012).

41. G. W. Hennig, T. W. Gould, S. D. Koh, R. D. Corrigan, D. J. Heredia, M. C. Shonnard, and T. K. Smith, "Use of Genetically Encoded Calcium Indicators (GECIs) Combined with Advanced Motion Tracking Techniques to Examine the Behavior of Neurons and Glia in the Enteric Nervous System of the Intact Murine Colon," Frontiers in cellular neuroscience **9**, 436 (2015).

42. J. Jonkman and E. Stelzer, "Resolution and contrast in confocal and two-photon microscopy," in *Confocal and two-photon microscopy : foundations, applications, and advances*, A. Diaspro, ed. (Wiley-Liss, New York, 2002), pp. 101-151.

43. C. Xu and W. W. Webb, "Measurement of two-photon excitation cross sections of molecular fluorophores with data from 690 to 1050 nm," J Opt Soc Am B **13**, 481-491 (1996).

44. J. P. Zinter and M. J. Levene, "Maximizing fluorescence collection efficiency in multiphoton microscopy," Optics express **19**, 15348-15362 (2011).

45. A. Singh, J. D. McMullen, E. A. Doris, and W. R. Zipfel, "Comparison of objective lenses for multiphoton microscopy in turbid samples," Biomedical optics express **6**, 3113-3127 (2015).

46. E. P. Perillo, J. E. McCracken, D. C. Fernee, J. R. Goldak, F. A. Medina, D. R. Miller, H. C. Yeh, and A. K. Dunn, "Deep in vivo two-photon microscopy with a low cost custom built mode-locked 1060 nm fiber laser," Biomedical optics express **7**, 324-334 (2016).

47. G. E. Stutzmann and I. Parker, "Dynamic multiphoton imaging: a live view from cells to systems," Physiology (Bethesda) **20**, 15-21 (2005).

48. A. Fiser, D. Mahringer, H. K. Oyibo, A. V. Petersen, M. Leinweber, and G. B. Keller, "Experience-dependent spatial expectations in mouse visual cortex," Nature neuroscience **19**, 1658-1664 (2016).

49. J. N. Stirman, I. T. Smith, M. W. Kudenov, and S. L. Smith, "Wide field-of-view, multi-region, two-photon imaging of neuronal activity in the mammalian brain," Nature biotechnology **34**, 857-862 (2016).

50. D. Huber, D. A. Gutnisky, S. Peron, D. H. O'Connor, J. S. Wiegert, L. Tian, T. G. Oertner, L. L. Looger, and K. Svoboda, "Multiple dynamic representations in the motor cortex during sensorimotor learning," Nature **484**, 473-478 (2012).

51. R. Kawakami, K. Sawada, A. Sato, T. Hibi, Y. Kozawa, S. Sato, H. Yokoyama, and T. Nemoto, "Visualizing hippocampal neurons with in vivo two-photon microscopy using a 1030 nm picosecond pulse laser," Scientific reports **3**(2013).

52. D. A. Dombeck, C. D. Harvey, L. Tian, L. L. Looger, and D. W. Tank, "Functional imaging of hippocampal place cells at cellular resolution during virtual navigation," Nature neuroscience **13**, 1433-U1180 (2010).

53. M. Kondo, K. Kobayashi, M. Ohkura, J. Nakai, and M. Matsuzaki, "Two-photon calcium imaging of the medial prefrontal cortex and hippocampus without cortical invasion," eLife **6**(2017).

54. R. Mostany and C. Portera-Cailliau, "A craniotomy surgery procedure for chronic brain imaging," Journal of visualized experiments : JoVE (2008).

55. R. Mostany and C. Portera-Cailliau, "A method for 2-photon imaging of blood flow in the neocortex through a cranial window," Journal of visualized experiments : JoVE (2008).

56. J. D. Driscoll, A. Y. Shih, P. J. Drew, G. Cauwenberghs, and D. Kleinfeld, "Two-photon imaging of blood flow in the rat cortex," Cold Spring Harbor protocols **2013**, 759-767 (2013).

57. T. Sasaki, N. Takahashi, N. Matsuki, and Y. Ikegaya, "Fast and accurate detection of action potentials from somatic calcium fluctuations," Journal of neurophysiology **100**, 1668-1676 (2008).

58. D. Smetters, A. Majewska, and R. Yuste, "Detecting action potentials in neuronal populations with calcium imaging," Methods-a Companion to Methods in Enzymology **18**, 215-221 (1999).

59. D. Davalos, J. Grutzendler, G. Yang, J. V. Kim, Y. Zuo, S. Jung, D. R. Littman, M. L. Dustin, and W. B. Gan, "ATP mediates rapid microglial response to local brain injury in vivo," Nature neuroscience **8**, 752-758 (2005).

60. K. E. Poskanzer and R. Yuste, "Astrocytes regulate cortical state switching in vivo," Proceedings of the National Academy of Sciences of the United States of America **113**, E2675-2684 (2016).

61. I. Veilleux, J. A. Spencer, D. P. Biss, D. Cote, and C. P. Lin, "In Vivo Cell Tracking With Video Rate Multimodality Laser Scanning Microscopy," IEEE J. Sel. Top. Quantum Electron **14**, 10-18 (2008).

62. D. Debarre, E. J. Botcherby, T. Watanabe, S. Srinivas, M. J. Booth, and T. Wilson, "Image-based adaptive optics for two-photon microscopy," Optics letters **34**, 2495-2497 (2009).

63. K. Bahlmann, P. T. So, M. Kirber, R. Reich, B. Kosicki, W. McGonagle, and K. Bellve, "Multifocal multiphoton microscopy (MMM) at a frame rate beyond 600 Hz," Optics express **15**, 10991-10998 (2007).

64. L. Sacconi, E. Froner, R. Antolini, M. R. Taghizadeh, A. Choudhury, and F. S. Pavone, "Multiphoton multifocal microscopy exploiting a diffractive optical element," Optics letters **28**, 1918-1920 (2003).

65. N. J. Sofroniew, D. Flickinger, J. King, and K. Svoboda, "A large field of view two-photon mesoscope with subcellular resolution for in vivo imaging," eLife **5**(2016).

66. P. S. Tsai, C. Mateo, J. J. Field, C. B. Schaffer, M. E. Anderson, and D. Kleinfeld, "Ultra-large field-of-view two-photon microscopy," Optics express **23**, 13833-13847 (2015).

67. A. Negrean and H. D. Mansvelder, "Optimal lens design and use in laser-scanning microscopy," Biomedical optics express **5**, 1588-1609 (2014).

68. E. Beaurepaire and J. Mertz, "Epifluorescence collection in two-photon microscopy," Applied optics **41**, 5376-5382 (2002).

69. L. C. Cheng, N. G. Horton, K. Wang, S. J. Chen, and C. Xu, "Measurements of multiphoton action cross sections for multiphoton microscopy," Biomedical optics express **5**, 3427-3433 (2014).

70. J. N. Kerr and W. Denk, "Imaging in vivo: watching the brain in action," Nature reviews. Neuroscience **9**, 195-205 (2008).

71. P. Tian, A. Devor, S. Sakadzic, A. M. Dale, and D. A. Boas, "Monte Carlo simulation of the spatial resolution and depth sensitivity of two-dimensional optical imaging of the brain," Journal of biomedical optics **16**, 016006 (2011).

72. S. R. Arridge, M. Cope, and D. T. Delpy, "The theoretical basis for the determination of optical pathlengths in tissue: temporal and frequency analysis," Physics in medicine and biology **37**, 1531-1560 (1992).

73. T. D. Harris, "Two-Photon Fluorescent Probes" (2012), retrieved https://www.janelia.org/lab/harris-lab-apig/research/photophysics/two-photon-fluorescent-probes.

74. M. H. Mohajerani, A. W. Chan, M. Mohsenvand, J. LeDue, R. Liu, D. A. McVea, J. D. Boyd, Y. T. Wang, M. Reimers, and T. H. Murphy, "Spontaneous cortical activity alternates between motifs defined by regional axonal projections," Nature neuroscience **16**, 1426-1435 (2013).

75. A. Q. Bauer, A. W. Kraft, P. W. Wright, A. Z. Snyder, J. M. Lee, and J. P. Culver, "Optical imaging of disrupted functional connectivity following ischemic stroke in mice," NeuroImage **99**, 388-401 (2014).

76. P. S. Tsai, N. Nishimura, E. J. Yoder, E. M. Dolnick, A. W. G., and D. Kleinfeld, "Principles, Design, and Construction of a Two-Photon Laser-Scanning Microscope for In Vitro and In Vivo Brain Imaging," in *In vivo optical imaging of brain function*, R. D. Frostig, ed. (CRC Press, Boca Raton, 2002), pp. 113–171.

77. W. J. Smith, "Optical System Considerations," in *Modern optical engineering : the design of optical systems*, 4th ed. (McGraw Hill, New York, 2008), pp. 53-67.

78. W. B. Wetherell, "Afocal systems," in *Handbook of optics. Volume II, Design, fabrication, and testing; sources and detectors; radiometry and photometry*, 3rd ed., M. Bass, C. DeCusatis, J. M. Enoch, V. Lakshminarayanan, G. Li, C. A. MacDonald, V. N. Mahajan, and E. W. Van Stryland, eds. (McGraw-Hill, New York, 2010), p. 1 electronic text.

79. M. Mansuripur, "Abbe's sine condition," in *Classical optics and its applications* (Cambridge University Press, New York, 2009), pp. 1-8.

80. C. Xu, "Cross-sections of fluorescence molecules in multiphoton microscopy," in *Confocal and two-photon microscopy : foundations, applications, adn advances*, A. Diaspro, ed. (Wiley-Liss, New York, 2002), pp. 75-99.

81. B. E. A. Saleh and M. C. Teich, “Beam Optics,” in *Fundamentals of photonics*, 2nd ed. (Wiley ; John Wiley distributor, Hoboken, N.J. Chichester, 2007), pp. 74-101.

82. T. H. Kim, Y. P. Zhang, J. Lecoq, J. C. Jung, J. Li, H. K. Zeng, C. M. Niell, and M. J. Schnitzer, "Long-Term Optical Access to an Estimated One Million Neurons in the Live Mouse Cortex," Cell reports **17**, 3385-3394 (2016).

83. R. M. Dijkhuizen, J. P. Beekwilder, H. B. van der Worp, J. W. Berkelbach van der Sprenkel, K. A. Tulleken, and K. Nicolay, "Correlation between tissue depolarizations and damage in focal ischemic rat brain," Brain research **840**, 194-205 (1999).

84. J. P. Dreier, "The role of spreading depression, spreading depolarization and spreading ischemia in neurological disease," Nature medicine **17**, 439-447 (2011).

85. V. V. Nikulin, T. Fedele, J. Mehnert, A. Lipp, C. Noack, J. Steinbrink, and G. Curio, "Monochromatic ultra-slow (~0.1 Hz) oscillations in the human electroencephalogram and their relation to hemodynamics," NeuroImage **97**, 71-80 (2014).

86. M. Prinz and J. Priller, "The role of peripheral immune cells in the CNS in steady state and disease," Nature neuroscience **20**, 136-144 (2017).

87. J. L. Chen, F. F. Voigt, M. Javadzadeh, R. Krueppel, and F. Helmchen, "Long-range population dynamics of anatomically defined neocortical networks," eLife **5**(2016).

88. N. D. Kirkpatrick, E. Chung, D. C. Cook, X. Han, G. Gruionu, S. Liao, L. L. Munn, T. P. Padera, D. Fukumura, and R. K. Jain, "Video-rate resonant scanning multiphoton microscopy: An emerging technique for intravital imaging of the tumor microenvironment," Intravital **1**(2012).

89. R. Prevedel, A. J. Verhoef, A. J. Pernia-Andrade, S. Weisenburger, B. S. Huang, T. Nobauer, A. Fernandez, J. E. Delcour, P. Golshani, A. Baltuska, and A. Vaziri, "Fast volumetric calcium imaging across multiple cortical layers using sculpted light," Nature methods **13**, 1021-1028 (2016).

90. R. Lu, W. Sun, Y. Liang, A. Kerlin, J. Bierfeld, J. D. Seelig, D. E. Wilson, B. Scholl, B. Mohar, M. Tanimoto, M. Koyama, D. Fitzpatrick, M. B. Orger, and N. Ji, "Video-rate volumetric functional imaging of the brain at synaptic resolution," Nature neuroscience **20**, 620-628 (2017).

91. G. Theriault, M. Cottet, A. Castonguay, N. McCarthy, and Y. De Koninck, "Extended two-photon microscopy in live samples with Bessel beams: steadier focus, faster volume scans, and simpler stereoscopic imaging," Frontiers in cellular neuroscience **8**, 139 (2014).

92. C. K. Tung, Y. Sun, W. Lo, S. J. Lin, S. H. Jee, and C. Y. Dong, "Effects of objective numerical apertures on achievable imaging depths in multiphoton microscopy," Microscopy research and technique **65**, 308-314 (2004).

93. C. H. Tran and G. R. Gordon, "Acute two-photon imaging of the neurovascular unit in the cortex of active mice," Frontiers in cellular neuroscience **9**, 11 (2015).

94. A. Nimmerjahn, "Two-photon imaging of microglia in the mouse cortex in vivo," Cold Spring Harbor protocols **2012**(2012).

95. X. Yang, Y. Pu, C. L. Hsieh, C. A. Ong, D. Psaltis, and K. M. Stankovic, "Two-photon microscopy of the mouse cochlea in situ for cellular diagnosis," Journal of biomedical optics **18**, 31104 (2013).

96. B. H. Zinselmeyer, J. Dempster, D. L. Wokosin, J. J. Cannon, R. Pless, I. Parker, and M. J. Miller, "Two-photon microscopy and multidimensional analysis of cell dynamics," Methods in enzymology **461**, 349-378 (2009).

97. B. M. Ances, J. H. Greenberg, and J. A. Detre, "Interaction between nitric oxide synthase inhibitor induced oscillations and the activation flow coupling response," Brain research **1309**, 19-28 (2010).

98. B. J. Vakoc, R. M. Lanning, J. A. Tyrrell, T. P. Padera, L. A. Bartlett, T. Stylianopoulos, L. L. Munn, G. J. Tearney, D. Fukumura, R. K. Jain, and B. E. Bouma, "Three-dimensional microscopy of the tumor microenvironment in vivo using optical frequency domain imaging," Nature medicine **15**, 1219-1223 (2009).

99. A. Y. Shih, J. D. Driscoll, P. J. Drew, N. Nishimura, C. B. Schaffer, and D. Kleinfeld, "Two-photon microscopy as a tool to study blood flow and neurovascular coupling in the rodent brain," Journal of cerebral blood flow and metabolism : official journal of the International Society of Cerebral Blood Flow and Metabolism **32**, 1277-1309 (2012).

100. A. T. Hammond and B. S. Glick, "Raising the speed limits for 4D fluorescence microscopy," Traffic **1**, 935-940 (2000).

101. W. Gobel, B. M. Kampa, and F. Helmchen, "Imaging cellular network dynamics in three dimensions using fast 3D laser scanning," Nature methods **4**, 73-79 (2007).

102. A. Kaplan, N. Friedman, and N. Davidson, "Acousto-optic lens with very fast focus scanning," Optics letters **26**, 1078-1080 (2001).

103. B. F. Grewe, F. F. Voigt, M. Van't Hoff, and F. Helmchen, "Fast two-layer two-photon imaging of neuronal cell populations using an electrically tunable lens," Biomedical optics express **2**, 2035-2046 (2011).

104. G. Katona, G. Szalay, P. Maak, A. Kaszas, M. Veress, D. Hillier, B. Chiovini, E. S. Vizi, B. Roska, and B. Rozsa, "Fast two-photon in vivo imaging with three-dimensional random-access scanning in large tissue volumes," Nature methods **9**, 201-208 (2012).

105. E. J. Botcherby, R. Juskaitis, M. J. Booth, and T. Wilson, "An optical technique for remote focusing in microscopy," Opt Commun **281**, 880-887 (2008).

106. E. J. Botcherby, M. J. Booth, R. Juskaitis, and T. Wilson, "Real-time extended depth of field microscopy," Optics express **16**, 21843-21848 (2008).

107. S. Prahl, "Optical Absorption of Hemoglobin," Oregon Medical Laser Center (2002).

108. J. A. Turner, E. Damaraju, T. G. van Erp, D. H. Mathalon, J. M. Ford, J. Voyvodic, B. A. Mueller, A. Belger, J. Bustillo, S. McEwen, S. G. Potkin, Fbirn, and V. D. Calhoun, "A multi-site resting state fMRI study on the amplitude of low frequency fluctuations in schizophrenia," Frontiers in neuroscience **7**, 137 (2013).

109. D. Cordes, V. M. Haughton, K. Arfanakis, J. D. Carew, P. A. Turski, C. H. Moritz, M. A. Quigley, and M. E. Meyerand, "Frequencies contributing to functional connectivity in the cerebral cortex in "resting-state" data," AJNR. American journal of neuroradiology **22**, 1326-1333 (2001).

110. F. Carbonell, P. Bellec, and A. Shmuel, "Global and system-specific resting-state fMRI fluctuations are uncorrelated: principal component analysis reveals anti-correlated networks," Brain connectivity **1**, 496-510 (2011).

111. B. Biswal, F. Z. Yetkin, V. M. Haughton, and J. S. Hyde, "Functional connectivity in the motor cortex of resting human brain using echo-planar MRI," Magnetic resonance in medicine : official journal of the Society of Magnetic Resonance in Medicine / Society of Magnetic Resonance in Medicine **34**, 537-541 (1995).

112. M. De Luca, S. Smith, N. De Stefano, A. Federico, and P. M. Matthews, "Blood oxygenation level dependent contrast resting state networks are relevant to functional activity in the neocortical sensorimotor system," Experimental brain research **167**, 587-594 (2005).

113. J. L. Vincent, G. H. Patel, M. D. Fox, A. Z. Snyder, J. T. Baker, D. C. Van Essen, J. M. Zempel, L. H. Snyder, M. Corbetta, and M. E. Raichle, "Intrinsic functional architecture in the anaesthetized monkey brain," Nature **447**, 83-86 (2007).

114. C. P. Pawela, B. B. Biswal, Y. R. Cho, D. S. Kao, R. Li, S. R. Jones, M. L. Schulte, H. S. Matloub, A. G. Hudetz, and J. S. Hyde, "Resting-state functional connectivity of the rat brain," Magnetic resonance in medicine : official journal of the Society of Magnetic Resonance in Medicine / Society of Magnetic Resonance in Medicine **59**, 1021-1029 (2008).

115. M. D. Fox and M. E. Raichle, "Spontaneous fluctuations in brain activity observed with functional magnetic resonance imaging," Nature reviews. Neuroscience **8**, 700-711 (2007).

116. M. P. Vanni and T. H. Murphy, "Mesoscale transcranial spontaneous activity mapping in GCaMP3 transgenic mice reveals extensive reciprocal connections between areas of somatomotor cortex," The Journal of neuroscience : the official journal of the Society for Neuroscience **34**, 15931-15946 (2014).

117. R. M. Hutchison, S. M. Mirsattari, C. K. Jones, J. S. Gati, and L. S. Leung, "Functional networks in the anesthetized rat brain revealed by independent component analysis of resting-state FMRI," Journal of neurophysiology **103**, 3398-3406 (2010).

118. C. Aalkjaer and H. Nilsson, "Vasomotion: cellular background for the oscillator and for the synchronization of smooth muscle cells," British journal of pharmacology **144**, 605-616 (2005).

119. C. Julien, "The enigma of Mayer waves: Facts and models," Cardiovascular research **70**, 12-21 (2006).

120. R. K. Pradhan and V. S. Chakravarthy, "Informational dynamics of vasomotion in microvascular networks: a review," Acta Physiol (Oxf) **201**, 193-218 (2011).

121. K. Murphy, R. M. Birn, and P. A. Bandettini, "Resting-state fMRI confounds and cleanup," NeuroImage **80**, 349-359 (2013).

122. D. Zhang and M. E. Raichle, "Disease and the brain's dark energy," Nature reviews. Neurology **6**, 15-28 (2010).

123. J. E. Mayhew, S. Askew, Y. Zheng, J. Porrill, G. W. Westby, P. Redgrave, D. M. Rector, and R. M. Harper, "Cerebral vasomotion: a 0.1-Hz oscillation in reflected light imaging of neural activity," NeuroImage **4**, 183-193 (1996).

124. W. G. Hundley, G. J. Renaldo, J. E. Levasseur, and H. A. Kontos, "Vasomotion in cerebral microcirculation of awake rabbits," The American journal of physiology **254**, H67-71 (1988).

125. C. Rivadulla, C. de Labra, K. L. Grieve, and J. Cudeiro, "Vasomotion and neurovascular coupling in the visual thalamus in vivo," PloS one **6**, e28746 (2011).

126. A. Rayshubskiy, T. J. Wojtasiewicz, C. B. Mikell, M. B. Bouchard, D. Timerman, B. E. Youngerman, R. A. McGovern, M. L. Otten, P. Canoll, G. M. McKhann, 2nd, and E. M. Hillman, "Direct, intraoperative observation of ~0.1 Hz hemodynamic oscillations in awake human cortex: implications for fMRI," NeuroImage **87**, 323-331 (2014).

127. W. H. Cooke, J. B. Hoag, A. A. Crossman, T. A. Kuusela, K. U. Tahvanainen, and D. L. Eckberg, "Human responses to upright tilt: a window on central autonomic integration," The Journal of physiology **517 (Pt 2)**, 617-628 (1999).

128. S. A. Landsverk, P. Kvandal, A. Bernjak, A. Stefanovska, and K. A. Kirkeboen, "The effects of general anesthesia on human skin microcirculation evaluated by wavelet transform," Anesthesia and analgesia **105**, 1012-1019, table of contents (2007).

129. D. J. Lefer, C. D. Lynch, K. C. Lapinski, and P. M. Hutchins, "Enhanced vasomotion of cerebral arterioles in spontaneously hypertensive rats," Microvascular research **39**, 129-139 (1990).

130. H. Nilsson and C. Aalkjaer, "Vasomotion: mechanisms and physiological importance," Molecular interventions **3**, 79-89, 51 (2003).

131. A. T. Eggebrecht, S. L. Ferradal, A. Robichaux-Viehoever, M. S. Hassanpour, H. Dehghani, A. Z. Snyder, T. Hershey, and J. P. Culver, "Mapping distributed brain function and networks with diffuse optical tomography," Nature photonics **8**, 448-454 (2014).

132. M. D. Greicius, G. Srivastava, A. L. Reiss, and V. Menon, "Default-mode network activity distinguishes Alzheimer's disease from healthy aging: evidence from functional MRI," Proceedings of the National Academy of Sciences of the United States of America **101**, 4637-4642 (2004).

133. W. Guo, C. Xiao, G. Liu, S. C. Wooderson, Z. Zhang, J. Zhang, L. Yu, and J. Liu, "Decreased resting-state interhemispheric coordination in first-episode, drug-naive paranoid schizophrenia," Progress in neuro-psychopharmacology & biological psychiatry **48**, 14-19 (2014).

134. R. Furlan, A. Porta, F. Costa, J. Tank, L. Baker, R. Schiavi, D. Robertson, A. Malliani, and R. Mosqueda-Garcia, "Oscillatory patterns in sympathetic neural discharge and cardiovascular variables during orthostatic stimulus," Circulation **101**, 886-892 (2000).

135. F. Tian, H. Niu, B. Khan, G. Alexandrakis, K. Behbehani, and H. Liu, "Enhanced functional brain imaging by using adaptive filtering and a depth compensation algorithm in diffuse optical tomography," IEEE transactions on medical imaging **30**, 1239-1251 (2011).

136. Y. Zhang, D. H. Brooks, M. A. Franceschini, and D. A. Boas, "Eigenvector-based spatial filtering for reduction of physiological interference in diffuse optical imaging," Journal of biomedical optics **10**, 11014 (2005).

137. Y. J. Zhang, L. Duan, H. Zhang, B. B. Biswal, C. M. Lu, and C. Z. Zhu, "Determination of dominant frequency of resting-state brain interaction within one functional system," PloS one **7**, e51584 (2012).

138. S. Sasai, F. Homae, H. Watanabe, and G. Taga, "Frequency-specific functional connectivity in the brain during resting state revealed by NIRS," NeuroImage **56**, 252-257 (2011).

139. J. L. Marchini and B. D. Ripley, "A new statistical approach to detecting significant activation in functional MRI," NeuroImage **12**, 366-380 (2000).

140. F. T. Sun, L. M. Miller, and M. D'Esposito, "Measuring interregional functional connectivity using coherence and partial coherence analyses of fMRI data," NeuroImage **21**, 647-658 (2004).

141. G. G. Somjen, "Mechanisms of spreading depression and hypoxic spreading depression-like depolarization," Physiological reviews **81**, 1065-1096 (2001).

142. Z. Bere, T. P. Obrenovitch, G. Kozak, F. Bari, and E. Farkas, "Imaging reveals the focal area of spreading depolarizations and a variety of hemodynamic responses in a rat microembolic stroke model," Journal of cerebral blood flow and metabolism : official journal of the International Society of Cerebral Blood Flow and Metabolism **34**, 1695-1705 (2014).

143. E. Jonckers, D. Shah, J. Hamaide, M. Verhoye, and A. Van der Linden, "The power of using functional fMRI on small rodents to study brain pharmacology and disease," Frontiers in pharmacology **6**, 231 (2015).

144. L. Schermelleh, R. Heintzmann, and H. Leonhardt, "A guide to super-resolution fluorescence microscopy," The Journal of cell biology **190**, 165-175 (2010).

145. G. A. Zheng, R. Horstmeyer, and C. H. Yang, "Wide-field, high-resolution Fourier ptychographic microscopy," Nature photonics **7**, 739-745 (2013).

146. K. H. Kim, C. Buehler, K. Bahlmann, T. Ragan, W. C. Lee, E. Nedivi, E. L. Heffer, S. Fantini, and P. T. So, "Multifocal multiphoton microscopy based on multianode photomultiplier tubes," Optics express **15**, 11658-11678 (2007).

147. A. I. Mohammed, H. J. Gritton, H. A. Tseng, M. E. Bucklin, Z. J. Yao, and X. Han, "An integrative approach for analyzing hundreds of neurons in task performing mice using wide-field calcium imaging," Scientific reports **6**(2016).

148. A. Mendez-Vilas and J. Diaz, *Two-Photon Fluorescence Microscopy: Basic Principles, Advantages and Risks*, Modern Research and Educational Topics in Microscopy (Formatex, Badajoz, Spain, 2007), Vol. 1.

149. I. B. Juhasz and A. I. Csurgay, "Fluorescence in two-photon-excited diffusible samples exposed to photobleaching: a simulation-based study," Journal of biomedical optics **20**(2015).

150. A. Diaspro and C. J. Sheppard, "Two-photon Excitation Fluorescence Microscopy," in *Confocal and two-photon microscopy : foundations, applications, and advances*, A. Diaspro, ed. (Wiley-Liss, New York, 2002).

151. T. Nemoto, "Living cell functions and morphology revealed by two-photon microscopy in intact neural and secretory organs," Mol Cells **26**, 113-120 (2008).

152. M. Matsuzaki, G. C. R. Ellis-Davies, and H. Kasai, "Three-dimensional mapping of unitary synaptic connections by two-photon macro photolysis of caged glutamate," Journal of neurophysiology **99**, 1535-1544 (2008).

Appendix A: Two-Photon Absorption

A fluorophore can be excited from its ground state to an excited state by absorption of a photon with energy equal to the bandgap of the two states. Energy is lost due to vibrational relaxation, and then a photon of less energy is emitted. This process of excitation and emission is called one-photon fluorescence, and it is at the basis of confocal microscopy, wide-field fluorescence microscopy, and light sheet microscopy. It is also possible for two photons of less energy of the bandgap to simultaneously interact with a fluorophore to excite it. After some losses due to vibration, a single photon is emitted. Unsurprisingly, this process is called two-photon fluorescence (Fig. 1.2) [12, 36, 76].

The probability of two-photon absorption by a fluorophore is much lower than the probability of one-photon absorption. For example, a fluorophore experiences a one-photon absorption event on the order of once per second on a sunny day, whereas two-photon absorption by the same fluorophore occurs once every 10 million years [148]. A couple questions may come to mind now: "Why is two-photon absorption so improbable?" and "Why is it used for optical sectioning microscopy?"

A complete answer to the first question requires analysis of one and two-photon absorption using the Schrödinger equation, first-order perturbation theory, and Fermi's golden rule, which are beyond the scope of this dissertation [149]. For another, more intuitive, explanation using the Poisson distribution, see ref [150]. At the basis of this latter explanation is the assumption that the probability of two-photon absorption should be proportional to the probability of finding two photons within the volume of the fluorophore at the same time. This probability is much less than the probability of finding a single photon within the volume of a fluorophore, and thus in most light conditions two-photon absorption is essentially impossible.

Through these derivations, it is also shown that the rate of two-photon absorption is proportional to the square of the light intensity and that the two-photon cross section of the fluorophore is 10^{33} times smaller than the one-photon cross section [151]. The cross section of a fluorophore can be thought of as an interaction term between a fluorophore and photons, it is often conceptualized as "how big" the fluorophore appears to photons . These results provide a good starting point for a more rigorous analysis of two-photon absorption. Through this analysis, we will gain an understanding of some important consequences of two-photon absorption that make it useful for optical sectioning imaging.

The rate at which a fluorophore transitions from the ground to excited state due to one-photon absorption is given by:

$$R_1(\vec{r},t) = \sigma_1 F(\vec{r},t) = \sigma_1 F_0(t) S(\vec{r}) \tag{A.1}$$

where R_1 is the rate of one-photon absorption for a fluorophore located at position specified by the 3D spatial vector $\vec{r}$, t is time, σ_1 is the one-photon cross-section in units of cm^2/photon, and F is the photon flux in units of photons/(cm^2s) [149]. The time and spatial dependence of the photon flux can be separated and written as $F_0(t)S(\vec{r})$, where $F_0(t)$ is the photon flux at the center of the light source and S(r) is a spatial distribution [80]. Note that the photon flux is the intensity divided by the energy of a photon:

$$E_p = h\upsilon = \frac{hc}{\lambda} \tag{A.2}$$

where E_p is the energy of a photon, h is Planck's constant, ν is the frequency of the photon, c is the speed of light, and λ is the wavelength of light. The two-photon absorption rate for a fluorophore depends on the square of the photon flux:

$$R_2(\vec{r},t) = \sigma_2 F(\vec{r},t)^2 = \sigma_2\left(F_0(t)S(\vec{r})\right)^2 \tag{A.3}$$

where σ_2 is the two-photon cross-section in units of cm^4 s/$photon^2$ [148].

In microscopy applications, the excitation source for both one-photon and two-photon fluorescence is generally a laser beam, which is best approximated by a Gaussian beam [81]. Therefore, the equation for a Gaussian beam is used to express Eq. (A.1) and (A.2) as a function of parameters available to the microscopist (e.g. laser power, pulse rate, beam waist, etc.):

$$F_0(t) = \frac{2P(t)}{E_p \pi {w_0}^2} \tag{A.4}$$

where P is the average power of the laser and w_0 is the beam radius at the laser aperture. To simplify the analysis, $F_0(t)$ is written as a time average so that the one-photon and two-photon absorption rate are independent of time. For single-photon absorption, $F_0(t)$ becomes:

$$F_0 = \frac{2P_{ave}}{E_p \pi {w_0}^2} \tag{A.5}$$

where P_{ave} is the average power of the laser. For two-photon absorption, the result is less intuitive. The time average of $F_0(t)$ squared is

$$\langle F_0^2(t)\rangle = g^{(2)} F_0^2 \tag{A.6}$$

where $g^{(2)}$ is the second-order temporal coherence of the excitation source. For a CW laser, $g^{(2)} = 1$. For a pulsed laser $g^{(2)} = \frac{0.66}{f\tau}$, where f is the repetition rate of the laser and τ is the pulse duration [80]. A summary of the rates of one-photon and two-photon absorption of a fluorophore located at position designated by $\vec{r}$ is provided in Table A.1.

Table A.1. Time-averaged one-photon and two-photon absorption rate of a fluorophore as a function of space

Condition	Expression
One-photon absorption (CW)	$R_1(\vec{r}) = \frac{2\sigma_1 P_{ave}}{E_p \pi {w_0}^2} S(\vec{r})$
One-photon absorption (pulsed)	$R_1(\vec{r}) = \frac{2\sigma_1 P_{ave}}{E_p \pi {w_0}^2} S(\vec{r})$
Two-photon absorption (CW)	$R_2(\vec{r}) = \sigma_2 \left(\frac{2P_{ave}}{E_p \pi {w_0}^2}\right)^2 S^2(\vec{r})$
Two-photon absorption (pulsed)	$R_2(\vec{r}) = \frac{0.66\sigma_2}{f\tau} \left(\frac{2P_{ave}}{E_p \pi {w_0}^2}\right)^2 S^2(\vec{r})$

The spatial distribution factor for a Gaussian beam is given as:

$$S(\vec{r}) = \frac{w_0^2 \exp\left(-\frac{2(x^2+y^2)}{w^2(z)}\right)}{w^2(z)} \tag{A.6}$$

where W(z) is the beam width defined in Eq. 2.20, and W_0 is the beam waist defined in Eq. 2.23. It should be noted that the fluorescence signal is not equal to the rate of absorption. Other factors such as collection efficiency, fluorophore concentration, quantum efficiency, and collection NA all contribute to the SNR of the microscope [80, 81].

The point of this derivation was to help realize how two important properties of TPM result from the dependence of two-photon absorption on the intensity of light squared: axial specificity without a pinhole and the advantage of pulsed lasers in TPM [36]. To demonstrate that two-photon absorption is localized to the focal point, the rate due to one-photon and two-photon absorption was plotted as a function of space after being focused by a lens with focal length equal to 15mm (Fig. A.1(a)-(b)). The beam waist radius before the lens was set to 12.5mm and the wavelength for one-photon and two-photon absorption was set to 460nm and 800nm, respectively. The axial specificity of two-photon is difficult to realize by plotting the spatial dependence of the absorption

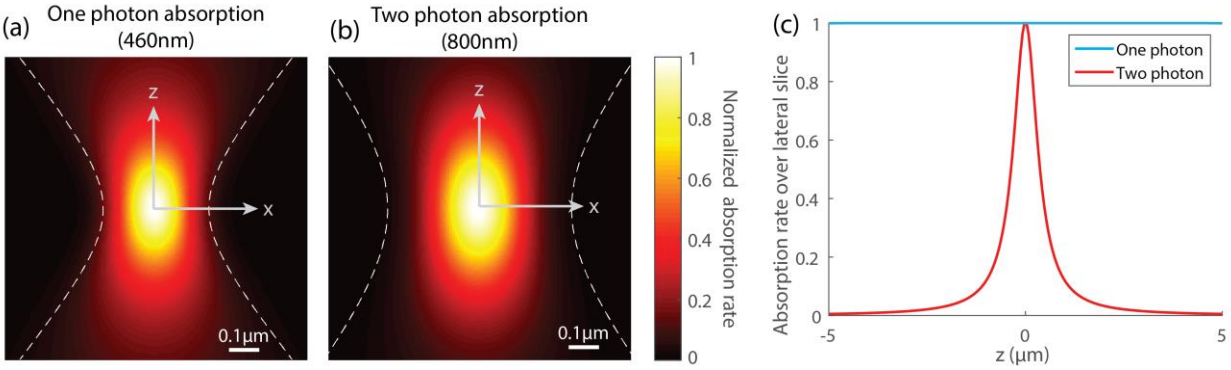

Fig. A.1. Axial confinement of two-photon excitation. (a) Spatial dependence of one-photon absorption. Dashed white lines are the beam waist of the excitation source. (b) Spatial dependence of two-photon absorption. Dashed white lines are the beam waist of the excitation source. (c) Absorption rate over entire axial cross sections as a function of axial position.

rate alone, so the rate of photon absorption was plotted as a function of axial position by summing the photon absorption rate over each xy cross section (Fig. A.1(c)) [152]. These results show that the number of photons absorbed over each xy cross section due to two-photon excitation depends on the axial position, whereas photons absorbed over each xy cross section due to one-photon excitation is independent of axial position. For a two-photon microscope, the emission is therefore localized to the focal point and does not need to be descanned. Another important feature of two-photon absorption that is apparent from Table A.1 is that a pulsed laser increases the rate of two-photon absorption by a factor of around 10^5 in comparison to a CW laser. Therefore, most two-photon microscopes use a TiSapphire laser, which is a pulsed laser with broad tuning range in the infrared.

The one-photon and two-photon absorption rates calculated here are not equal to the number of fluorescence photons collected per unit time, which depends on the fluorophore concentration, quantum efficiency, and collection efficiency [80]. For most two-photon microscopes, epifluorescence detection of the emitted photons is relayed onto a PMT (Section 2.2.3). Usually,

theoretical calculations of the absorption rate and fluorescence rate are expressed in terms of the NA of the objective lens. In the paraxial limit, the rate of two-photon absorption is independent of the NA of the objective lens [43]. However, Singh et al. recently showed that excitation rate for real diffraction-limited objectives decreases as a function of NA. The collection efficiency term that the fluorescence rate depends on is proportional to the collection NA squared. However, when accounting for the dependence of NA on the two-photon absorption rate, the actually fluorescence rate in an epi-collection two-photon microscope does not increase as rapidly as expected for the paraxial case [45].

The point spread function for a two-photon microscope is usually derived in a similar way to the absorption rate: the illumination point spread function is squared [42]. Therefore, the PSF has a similar profile shown in Fig. A.1. The resolution can be defined in several ways (e.g. 1/e, $1/e^2$, FWHM). In this report, we used the FWHM definition (Eq. 2.5).

Appendix B: Definition of Optical Invariant

The optical invariant can be defined in several ways. For this report, we were interested in analyzing telecentric, diffraction-limited microscopy systems. If the optical system or component is modeled with first-order principal planes, then the invariant at aperture and image planes is defined as

$$I = nr \tan\theta = n'F \tan\alpha \tag{B.1}$$

where I is the optical invariant, n and n' are the indices of refraction of the media before and after the optical component, r and θ are the beam radius and incident angle of collimated light at the aperture plane, and F and α are the field radius and angle of the cone of light at the image plane (Fig. B.1(a)) [78].

For paraxial rays [77], Eq. B.1 simplifies to:

$$I = nr\theta = n'F\alpha \tag{B.2}$$

Although Eq. B.1 is valid for systems modeled with thin lenses and Eq. B.2 is valid for paraxial systems, in many cases it is more accurate to model microscopy systems with spherical refracting surfaces centered at the front and back focal point of the optical system (Fig. B.1(b)). The vertices of these spherical surfaces are located at the principal points of the optical system. In this case, the optical invariant is defined as

$$I = nr \sin\theta = n'F \sin\alpha \tag{B.3}$$

Eq. B.3 is also known as the Abbe sine condition, which is valid for aplanatic optical systems that perfectly image points from one lateral plane to another lateral plane [79]. We opted to use Eq. B.3 because we typically calculated the optical invariant for well-designed optical systems under conditions in which the optical resolution was limited by diffraction. Note that this condition is

valid only for diffraction limited conjugate image and aperture planes, but is invalid for points along the optical axis that do not coincide with image and aperture planes. For imaging systems with perfect axial imaging, the Herschel condition must be satisfied [105]. The definition of the optical invariant in Eq. B.3 served as a useful guide for assessing the optical throughput of components even in cases for optics that were not aplanatic or for f-theta telecentric scan lenses for which $F = f\theta$, where f is the focal length of the scan lens.

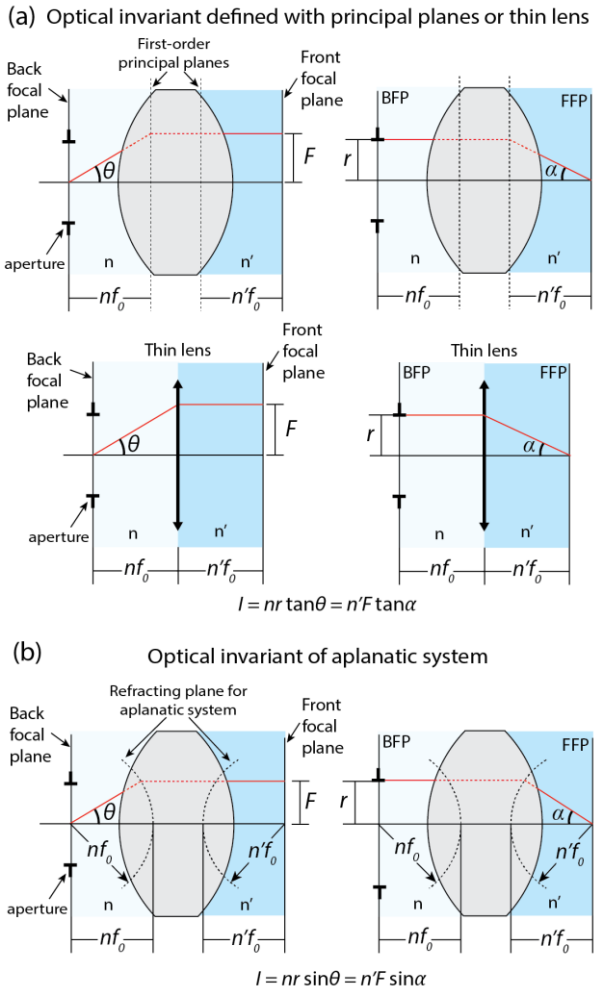

Fig. B.1. Definition of optical invariant. (a) Optical system modeled with first-order principal planes. Back focal plane and aperture stop coincide. Marginal and chief rays are shown to visualize field-of-view, numerical aperture, and optical invariant. Also shown is model of same system with a thin lens. (b) Same as (a), but for aplanatic model. Refracting surfaces are spherical.

Appendix C: Optical Components Analyzed for LF-TPM

C.1. Objective Lenses

We analyzed 45 commercially available Olympus objective lenses in this report (Table C.1). The invariant and SBP product were calculated using Eq. 2.5 and 2.9, respectively.

Table C.1 Specifications of 45 commercially available Olympus objective lenses analyzed.

Objective	M	FN	NA	n	Back aperture dia. (mm)	Invariant (mm)	SBP (MP)
UPLSAPO 4X	4	26.5	0.16	1	14.4	0.530	24.7
UPLFLN 4X	4	26.5	0.13	1	11.7	0.431	16.3
UPLFLN 4XP	4	26.5	0.13	1	11.7	0.431	16.3
PLN 4X	4	22	0.1	1	9	0.275	6.7
MVPLAPO 2 XC	4	22	0.5	1	45	1.375	166.5
XLFluor4x/340	4	26.5	0.28	1	25.2	0.928	75.7
UPLSAPO 10X2	10	26.5	0.4	1	14.4	0.530	24.7
UPLFLN 10X2	10	26.5	0.3	1	10.8	0.398	13.9
UMPLFN 10XW	10	26.5	0.3	1.33	10.8	0.398	13.9
UPLFLN 10XP	10	26.5	0.3	1	10.8	0.398	13.9
PLN 10X	10	22	0.25	1	9	0.275	6.7
XLPLN10XSVMP	10	18	0.6	1.33	21.6	0.540	25.7
UPLSAPO 20X	20	26.5	0.75	1	13.5	0.497	22.2
UPLFLN 20X	20	26.5	0.5	1	9	0.331	9.7
XLUMPLFLN-W	20	22	1	1.33	18	0.550	25.8
UMPLFN 20XW	20	26.5	0.5	1.33	9	0.331	9.7
UPLFLN 20XP	20	26.5	0.5	1	9	0.331	9.7
UCPLFLN 20X	20	22	0.7	1	12.6	0.385	13.1
LUCPLFLN 20X	20	22	0.45	1	8.1	0.248	5.4
LUCPLFLN 40X	20	22	0.6	1	10.8	0.330	9.6
PLN 20X	20	22	0.4	1	7.2	0.220	4.3

UAPON 20XW340	20	22	0.7	1.33	12.6	0.385	13.1
XLPLN25XWMP2	25	18	1.05	1.33	15.12	0.378	12.1
XLPLN25XSVMP2	25	18	1	1.33	14.4	0.360	11.1
XLSLPLN25XSVMP2	25	18	0.95	1.33	13.68	0.342	10.1
XLSLPLN25XGMP	25	18	1	1.41	14.4	0.360	11.1
UPLSAPO 30XS	30	22	1.05	1.41	12.6	0.385	12.5
UPLSAPO 60XO	40	26.5	0.95	1	8.55	0.315	8.5
UPLFLN 40X	40	26.5	0.75	1	6.75	0.248	5.5
UPLFLN 40XO	40	26.5	1.3	1.51	11.7	0.431	15.1
LUMPLFLN 40XW	40	26.5	0.8	1.33	7.2	0.265	6.2
UPLFLN 40XP	40	26.5	0.75	1	6.75	0.248	5.5
PLN 40X	40	22	0.65	1	5.85	0.179	2.8
UAPON 40XWO340-2	40	22	1.35	1.51	12.15	0.371	11.1
UAPON 40XW340	40	22	1.15	1.33	10.35	0.316	8.3
UPLSAPO 40X3	60	26.5	1.35	1.51	8.1	0.298	7.2
PLAPON 60XO	60	26.5	1.42	1.51	8.52	0.314	7.9
UPLFLN 60X	60	26.5	0.9	1	5.4	0.199	3.4
LUMPLFLN 60XW	60	26.5	1	1.33	6	0.221	4.2
LUMFLN 60XW	60	26.5	1.1	1.33	6.6	0.243	5.0
LUCPLFLN 60X	60	22	0.7	1	4.2	0.128	1.5
UPLSAPO 100XO	100	26.5	1.4	1.51	5.04	0.186	2.8
UPLFLN 100XO2	100	26.5	1.3	1.51	4.68	0.172	2.4
UPLFLN 100XOP	100	26.5	1.3	1.51	4.68	0.172	2.4
PLN 100XO	100	22	1.25	1.51	4.5	0.138	1.6

C.2. Scan Lenses

The 27 scan optics we analyzed in this report are included Table C.2. We included scan optics that were used in other LF-TPM systems [49, 65]. However, due to compensation optics that may be used in these systems, the performance of the scan optics in isolation may not be representative of the throughput of the integrated microscope.

Table C.2. Specifications of scan optics analyzed.

Lens ID#	Type	Focal length (mm)	Wavelength (nm)	Vendor	Part number
1	Plano-convex	50	600 – 1050 (coating only)	Edmund Optics	48-795
2	Plano-convex	60	725 – 1050 (coating only)	Qioptiq	G312340000
3	Plano-convex	60	650 – 1050 (coating only)	Thorlabs	LA1401-B
4	Plano-convex	100	600 – 1050 (coating only)	Edmund Optics	48-797
5	Plano-convex	100	725 – 1050 (coating only)	Qioptiq	G312334000
6	Plano-convex	100	650 – 1050 (coating only)	Thorlabs	LA1050-B
7	Plano-convex	200	600 – 1050 (coating only)	Edmund Optics	48-801
8	Plano-convex	200	650-1050 (coating only)	Thorlabs	LA1979-B
9	Plano-convex	300	725 – 1050 (coating only)	Qioptiq	G312363000
10	NIR achromatic doublet	100	750-1100	Edmund Optics	47-317
11	NIR Achromatic doublet	100	650 - 1050	Thorlabs	AC508-100-B
12	NIR Achromatic doublet	200	650 - 1050	Thorlabs	AC508-200-B
13	Compound achromatic doublet	100	650 - 1050	Thorlabs	AC508-200-B and AC508-200-B
14	Compound achromatic doublet	150	488 - 514	Qioptiq	322278000 and 322278000
15	Compound achromatic doublet	222	650 - 1050	Thorlabs	AC508-400-B and AC508-500-B
16	Compound achromatic doublet	222	650 - 1050	Thorlabs	AC508-400-B and AC508-500-B
17	Compound achromatic doublet	245	488 - 514	Qioptiq	322278000 and 322242000

18	Compound achromatic doublet	500	650 - 1050	Thorlabs	AC508-1000-B and AC508-1000-B
19	Telecentric f-theta scan lens	18	810 - 890 and 1000 - 1100	Thorlabs	LSM02-BB
20	Telecentric f-theta scan lens	36	810 - 890 and 1000 - 1100	Thorlabs	LSM03-BB
21	Telecentric f-theta scan lens	54	810 - 890 and 1000 - 1100	Thorlabs	LSM04-BB
22	Telecentric f-theta scan lens	54	750 - 950	Thorlabs	LSM54-850
23	Telecentric f-theta scan lens	58	920	Various	N/A
24	Telecentric f-theta scan lens	100	633	Edmund Optics	64-426
25	Telecentric f-theta scan lens	100	633	Various	64-426
26	Telecentric f-theta scan lens	110	810 - 890 and 1000 - 1100	Thorlabs	LSM05-BB
27	Telecentric f-theta scan lens	115	1064	Edmund Optics	64-422
28	Telecentric f-theta scan lens	235	920	Various	N/A
29	Plano-convex	50	600 – 1050 (coating only)	Edmund Optics	48-795